

BRANCHING AND CHAIN END EFFECTS ON SURFACE FLUCTUATIONS OF
POLYSTYRENE MELT FILMS

A Dissertation
Presented to
The Graduate Faculty of The University of Akron

In Partial Fulfillment
of the Requirements for the Degree
Doctor of Philosophy

Fan Zhang

December, 2018

BRANCHING AND CHAIN ENDS EFFECTS ON SURFACE FLUCTUATIONS OF
POLYSTYRENE MELT FILMS

Fan Zhang

Dissertation

Approved:

Advisor

Dr. Mark D. Foster

Advisor

Dr. Roderic P. Quirk

Committee Chair

Dr. Mesfin Tsige

Committee Member

Dr. Chrys Wesdemiotis

Committee Member

Dr. David S. Simmons

Accepted:

Department Chair

Dr. Tianbo Liu

Dean of the College

Dr. Ali Dhinojwala

Dean of the Graduate School

Dr. Chand Midha

Date

ABSTRACT

The first efficient method for synthesis of well-defined, tadpole-shaped polystyrene has been developed using anionic polymerization, silicon chloride linking chemistry and metathesis ring closure. The difunctional macromolecular linking agent, ω -methyldichlorosilylpolystyrene, was formed by reacting *sec*-butyllithium-initiated poly(styryl)lithium with excess (30 \times molar) methyltrichlorosilane to eliminate formation of linear dimer and three-arm star polystyrene. The asymmetric, three-arm, star precursor was formed by linking excess α -4-pentenylpoly(styryl)lithium (α -PSLi) with the macromolecular linking agent, and the excess α -PSLi was functionalized with ethylene oxide before termination with methanol to facilitate column chromatographic separation of unlinked arm. Cyclization of the asymmetric, three-arm, star precursor to form the tadpole-shaped polystyrene was effected in methylene chloride at high dilution using the Grubbs first generation catalyst, *bis*(tricyclohexylphosphine)benzylidene ruthenium(IV) chloride. The tadpole product was uniquely characterized by MALDI-ToF MS in terms of peaks that appeared characteristically 28 m/z units lower than those of the corresponding asymmetric, three-arm, star precursor and corresponding to the loss of an ethylene unit. The MALDI-ToF MS results showed that the tadpole-shaped polystyrene was of high purity. MD simulations find a smaller hydrodynamic volume for the tadpole-shaped PS as compared to the three-arm star precursor, in quantitative agreement with GPC results. Incorporating one cycle in the molecule, while leaving one chain end, leads to an increase in T_g of only $2.7 \pm 0.8^\circ\text{C}$, much smaller than the increase of $13.6 \pm 0.8^\circ\text{C}$ seen when going from the

linear chain to cyclic analog with no ends at all. These changes in T_g with architecture results are consistent with self-plasticization by free chain ends.

Thermally stimulated surface fluctuations in polymer films are important from a fundamental perspective. The surface fluctuations of melt films of linear polystyrene (LPS) and cyclic polystyrene chains (CPS) can be described by a hydrodynamic continuum theory (HCT) when the thickness, h , is sufficiently large. However, surface fluctuations can be slower than expected from the HCT when the viscosity enhancement manifests itself. To reveal branching and chain end effects on the surface fluctuations of melt films, the surface fluctuations of films of 15k, four-arm star polystyrene (SPS) and 6k TPS chains have been measured using X-ray Photon Correlation Spectroscopy (XPCS). For the star chains, the viscosity enhancement becomes evident at a film thickness between 112 nm ($40R_g$) and 72 nm ($26R_g$), which is remarkably larger than the critical thicknesses for LPS ($< 7R_g$) and CPS ($10\text{-}14R_g$) of the same molecular weight. This is true both for absolute thickness and thickness relative to chain size, R_g . XPCS data for the 15k star films can be rationalized using a two-layer model with a 17 nm ($6R_g$) thick, highly viscous layer at the silicon substrate, which is significantly thicker than the $1R_g$ thick “irreversibly adsorbed” layer. Here, the interpenetration of the chains accounts for this propagation of slow dynamics of the chains near substrate into the film. For a 29 nm ($10R_g$) thick film more striking viscosity enhancement occurs due to the overlapped viscosity enhancements from both interfaces.

For TPS, all the surface fluctuation relaxation times are well above those anticipated by the HCT adopting the bulk viscosity experimentally measured in this work. This observation is very surprising and most readily explained as resulting from an

inaccurate rheology measurement. Collapse of the data to a universal curve at a given temperature requires an increase in the highly viscous layer thickness with increasing temperature. This result suggests that these films were not fully equilibrated. The highly viscous layer was still growing during the measurement because the samples were effectively being annealed at the elevated temperature of the measurement. Rinsing films of TPS with good solvent yields an irreversibly adsorbed layer with thickness of $1R_g$ and scattering length density 20% larger than the bulk PS SLD value. The smaller relative thickness of the irreversibly adsorbed layer as compared to the irreversibly adsorbed layer of the CPS analog seems consistent with our anticipation that the linear tail should disrupt the compact packing. Again, the postulated highly viscous layer has been found to be much thicker than the irreversibly adsorbed layer after rinsing. We conjecture that threading of the cycles in some way provides a means for propagation of slow dynamics of the chains near the substrate.

ACKNOWLEDGEMENT

I would like to sincerely thank my advisor, Dr. Mark D. Foster, and my co-advisor, Dr. Roderic P. Quirk, for their guidance, support and helpful discussion all along the way during my PhD career. I wouldn't have been able to finish my research work without the help and encouragements from both of them. They have always been great role models in academia with their enthusiasm and dedication to science, their strict and precise attitude towards research as well as their high standards on experiment. Being exposed to such atmosphere, these qualities have been incorporated inside of me and are going to help me continuously grow and succeed in my future career. I would also like to thank all my committee members, Dr. Mesfin Tsige, Dr. Chrys Wesdemiotis and Dr. David S. Simmons for their helpful and insightful suggestions and discussions.

I would like to thank Dr. Chrys Wesdemiotis and Dr. Selim Gerislioglu for MALDI-ToF MS measurements and discussing the results. I would like to thank Dr. Bojie Wang for his help and advice in GPC measurements.

I would like to thank Dr. Suresh Narayanan and Dr. Zhang Jiang for assistance of XPCS measurement at APS national lab as well as guidance in data analysis and code debug.

I would like to thank Dr. Qiming He, who joined the group one year before me, helped me getting familiar with everything when I was a freshman in a foreign country and intrigued me joining Dr. Mark D. Foster's research group. I truly feel grateful for his help and advice all these years.

I would like to thank all the group members in Dr. Mark D. Foster's research group for building and keeping such a positive academic atmosphere in the group. I would also like to thank Dr. Chongwen Huang and Dr. Chao Wang for their help in rheology measurements.

I would like to thank my best friend, Dr. Wenpeng Shan, who's also been a roommate with me for more than four years, for his help both in life and work. Also, I would like to thank the other my best friend, Huan Zhang, who always imparts life wisdom to me.

Last but not the least, I would like to thank my girlfriend, Yixiao Feng, for continuous support and encouragement especially at my lowest. I would also like to thank my parents for their love, care and financial support.

Funding for this work was provided by the University of Akron Research Foundation. The use of the Advanced Photon Source at Argonne National Laboratory was supported by the DOE's Office of Science under Contract No. DE-AC02-06CH11357.

TABLE OF CONTENTS

LIST OF FIGURES	xi
LIST OF TABLES	xv
CHAPTERS	
I. INTRODUCTION	1
II. BACKGROUND	4
2.1 Synthesis of Tadpole-Shaped Polystyrene.....	4
2.2 Branching and Chain End Effects on Polymer Physical Properties	18
2.3 Kinetics of the Irreversibly Adsorbed Layer	22
2.4 Mobility Gradient in Polymer Thin Films	25
2.5 X-ray Photon Correlation Spectroscopy	29
III. EXPERIMENTAL.....	34
3.1 Requirements for Air Sensitive Materials	34
3.1.1 High Vacuum Techniques	34
3.1.2 Dry Box Manipulation.....	35
3.2 Purification of Materials	37
3.2.1 Solvents	37
3.2.2 Monomer	39
3.2.3 Terminating Agents	40

3.2.4 Initiator Materials	43
3.2.5 Ring-closure Catalyst	44
3.3 Synthesis of Tadpole-shaped Polystyrene	44
3.3.1 Synthesis of 5-Lithio-1-pentene ²²	44
3.3.2 Synthesis of ω -Methyldichlorosilylpolystyrene	46
3.3.3 Synthesis of Asymmetric, Three-arm, Star Polystyrene.....	48
3.3.4 Synthesis of Tadpole-Shaped Polystyrene	50
3.3.5 Synthesis of <i>tris</i> (α -4-Pentenylpolystyryl)methylsilane	51
3.3.6 Synthesis of Tadpole-shaped Polystyrene from <i>tris</i> (α -4- Pentenylpolystyryl)methylsilane	53
3.4 Synthesis of Four-arm, Star Polystyrene	54
3.5 Synthesis of Four-arm, Star Polyisoprene	55
3.6 Molecular Characterization.....	56
3.6.1 NMR Spectroscopy.....	56
3.6.2 Size Exclusion Chromatography (SEC)	57
3.6.3 MALDI-ToF Mass Spectrometry	57
3.6.4 Differential Scanning Calorimetry	58
3.6.5 Rheometry	58
3.7 Molecular Dynamics Simulations.....	59

3.8 Preparation of Polymer Films	60
3.8.1 Preparation of Polymer Films for XPCS	60
3.9 Instrument for the Study of Surface Fluctuations	61
3.9.1 X-ray Photon Correlation Spectroscopy	61
IV. SYNTHESSES AND CHARACTERIZATION OF TADPOLE-SHAPED POLYSTYRENES	66
4.1 <i>tris</i> (α -4-Pentenylpolystyryl)methylsilane	67
4.2 Tadpole-Shaped Polystyrene	71
4.3 Asymmetric, Three-arm, Star Polystyrene Precursor	75
4.4 Tadpole-Shaped Polystyrene	83
4.5 Physical Properties of 6k Tadpole-Shaped Polystyrene	87
V. VISCOSITY ENHANCEMENT IN SUPPORTED MOLTEN STAR POLYSTYRENE FILMS	94
VI. VISCOSITY ENHANCEMENT IN SUPPORTED MELT FILMS OF TADPOLE- SHAPED POLYSTYRENE	104
VII. CONCLUSIONS	118
REFERENCES	121
APPENDIX A	130
SURFACE FLUCTUATIONS OF TADPOLE-SHAPED POLYSTYRENE WITH 0.5% HIGH MOLECULAR WEIGHT DIMER IMPURITY	130

LIST OF FIGURES

Figure	Page
2.1 The reaction scheme for synthesis of tadpole-shaped poly(CEVE)-b-PS via a cationic coupling reaction of a heterodifunctional linear precursor.5	6
2.2 The reaction scheme for synthesis of tadpole-shaped polystyrenes via “electrostatic self-assembly and covalent fixation” process.6	7
2.3 The reaction scheme for synthesis of tadpole-shaped polycaprolactone with two tails via photochemical cyclization of acrylate groups.7	9
2.4 The reaction scheme for synthesis of tadpole-shaped copolymers via click cyclization chemistry.8	11
2.5 The reaction scheme for synthesis of tadpole-shaped polystyrenes via a coupling reaction between a ring polystyrene with two pendant diphenylethylene groups and poly(styryl)lithium.9	13
2.6 (a) Schematic illustration of the geometry for XPCS. (b) Speckle pattern of time averaged diffuse scattering measured using XPCS. (c) Speckle pattern from the fit to capillary wave model for a molten LPS sample. Reproduced with permission. ⁴⁶ Copyright 2003, American Physical Society.	31
3.1 Illustration of a glass high vacuum line for purification and anionic polymerization.35	
3.2 General view of vacuum glove box and air lock.	36
3.3 Illustration of reactor to synthesize 5-lithio-1-pentene.	46
3.4 Illustration of the reactors used to synthesize the ω -methyldichlorosilylpolystyrene.47	
3.5 Illustration of the reactor used to synthesize the asymmetric, three-arm, star polystyrene.	49

3.6 Illustration of the reactor used to synthesize the tadpole-shaped polystyrene.....	51
3.7 Illustration of the reactor used to synthesize the tris(α -4-pentenylpolystyryl)methylsilane.....	52
3.8 Illustration of the reactor used to synthesize the four-arm, star polystyrene.....	54
3.9 Illustration of the reactor used to synthesize the four-arm, star polyisoprene.....	56
3.10 Illustration of the XPCS setup at beam line 8-IDI at the Advanced Photon Source. Reproduced with permission. ⁴⁴ Copyright 2012, American Chemical Society.	62
3.11 CCD images of diffuse scattering collected using (a) full frame and (b) kinetic modes.	64
4.1 SEC chromatograms of purified tris(α -4-pentenylpolystyryl)methylsilane (red) and the corresponding tadpole-shaped polystyrene (black).....	68
4.2 ¹ H NMR spectrum of tris(α -4-pentenylpolystyryl)methylsilane.	69
4.3 MALDI-TOF MS of tris(α -4-pentenylpolystyryl)methylsilane.	70
4.4 Full MALDI-ToF MS of the tadpole-shaped polystyrene and the corresponding dimer formed by cyclization of tris(α -4-pentenylpolystyryl)methylsilane using grubbs 1st generation catalyst.	73
4.5 Blow up of the lower m/z region for the MALDI-ToF MS of the tadpole-shaped polystyrene and its dimer.	74
4.6 SEC chromatogram of the base polymer from sec-butyllithium-initiated polystyrene.	76
4.7 SEC chromatogram of α -4-pentenylpolystyrene.	77
4.8 SEC chromatograms of (a) purified asymmetric, three-arm, star precursor (blue, dashed curve) and (b) corresponding macrocyclic polystyrene (red, solid curve).	79

4.9 Probability distribution functions for hydrodynamic radii of the star and tadpole PS simulated using molecular dynamics of the pure melts at 510K after 1000 steps.....	80
4.10 ¹ H NMR spectra for (a) asymmetric, three-arm, star precursor and (b) the tadpole-shaped polystyrene.....	81
4.11 MALDI-MS spectrum of asymmetric, three-arm, star precursor.	83
4.12 MALDI-ToF MS spectrum for the tadpole-shaped polystyrene.....	85
4.13 Overlaid mass spectra for asymmetric, three-arm, star precursor and tadpole-shaped polystyrene.....	86
4.14 a) Top panel: DSC scans for the three-arm star precursor, tadpole, and linear analogue, performed on heating at 10 K/min after cooling at 10 K/min. b) Bottom panel: Absolute heat capacity for the three samples, along with results for a linear and cyclic polystyrene from Huang et al. ⁹⁶ and a compilation of results from the literature from Gaur and Wunderlich. ⁹⁷	90
4.15 Summary of the variation of T_g with density of chain ends for the molecules considered in this work, set in the context of variations seen in other studies. To understand the T_g behavior for the star precursor and tadpole studied here, it is sufficient to consider the density of chain ends, whereas for some molecules from Monteiro et al. ⁴⁰ with bulkier and stiffer junction points it is necessary to consider the junction point types as well.....	92
5.1 τ/h vs $q h$ at three temperatures for SPS films of two thickness. The dashed curves correspond to least-square fits using the HCT expression with η XPCS as a fitting parameter.....	96
5.2 Comparison of viscosities from XPCS (black squares) and bulk rheology (red circles) as a function of temperature for SPS.	97
5.3 τ/h vs $q h$ for SPS films with various thicknesses at (a) 120 °C (b) 130 °C and (c) 140°C. The dashed curves correspond to least-square fits to the HCT using the data for h of 112 and 277 nm.....	98

5.4 Collapse of the τ/h vs $q_{ }h$ data at three temperatures achieved by assuming an effective thickness, h_{eff} , for the film equal to total thickness minus the highly viscous layer thickness ($h-h_{vis}$, as shown in legend).	100
6.1 g^2 Functions at nine values of $q_{ }$ from TPS film of 144 nm.	107
6.2. τ/h vs $q_{ }h$ for TPS films with various thicknesses at (a) 115 °C, (b) 125 °C and (c) 135 °C. The dashed curves correspond to the HCT allowing the viscosity to float as a fitting parameter. The viscosity required to fit the data that overlap is substantially above bulk viscosity at each temperature.	109
6.3 Comparison of viscosities obtained from fitting the XPCS data for thicker films (black square) and from bulk rheometry (red circle) as a function of temperature for the 6k TPS.	111
6.4 Collapse of the τ/h vs $q_{ }h$ data at three temperatures achieved by assuming an effective thickness, h_{eff} , for the film, shown in the legend, which is equal to total thickness minus the highly viscous layer thickness.	113
6.5 X-ray reflectivity of the irreversibly adsorbed layer remaining after rinsing a 40 nm thick, annealed TPS film and drying in a high vacuum oven. The solid line represents the best fit to the data with the SLD depth profile shown in the inset.	115

LIST OF TABLES

Table	Page
4.1 T_g s for 6k polystyrenes with various architectures.....	89
5.1 Surface Tension and Bulk Viscosity of 15k Four-arm Star Polystyrene.....	95
6.1. Surface Tensions of 6k Tadpole-shaped Polystyrene.....	105

CHAPTER I

INTRODUCTION

Polymers with branched architectures exhibiting unique bulk dynamics and have drawn a lot of interest from both industrial and academic perspectives. Branched polymers have smaller hydrodynamic volumes and lower mean square radii of gyration than do their linear analogs; thus, melts of unentangled branched polymers can have remarkably low viscosities and high compliances as compared to melts of linear chains with the same overall molecular weight. It also has been shown that properties such as chain conformation, chain dynamics and crystallization behavior are significantly different.

Understanding the surface fluctuation behavior of thin films provides insight for developing new techniques and devices in coatings¹, membranes² and microlithography³. For thin films of branched polymers can show much slower surface dynamics than shown by films of their linear analogs; however, the mechanism behind this difference is still not well understood.

Three topics will be addressed in this work investigating the effects of branching and chain ends on thin film surface dynamics and changes with film thickness. The first topic is the synthesis and characterization of well-defined, tadpole-shaped polystyrene (TPS). The second topic is the anomalous viscosity enhancement slowing down star polystyrene melt thin films. The third topic is the effect of branching and chain ends on surface fluctuations of tadpole-shaped polystyrene melt thin films. Polystyrene was selected as a model polymer because a rich database on polystyrene physical properties

exists in the literature, which can be compared with our results; in addition, polystyrene is robust when subjected to X-ray radiation. Therefore, a well-defined tadpole-shaped polystyrene was synthesized using a combination of anionic polymerization, silicon chloride linking chemistry and metathesis ring-closure. In the first part of the dissertation, a new synthetic route for making a 6k, well-defined, tadpole-shaped polystyrene (TPS) will be described. The synthesis involves a macromolecular linking agent made via anionic polymerization, followed by the addition of poly(styryl)lithium initiated by a vinyl-containing organolithium initiator to generate an asymmetric, three-arm, star precursor; the last step involves a ring-closing metathesis reaction. The cyclization reaction has been optimized to eliminate the formation of dimer.

Variation in surface fluctuations of star polystyrene melt films with thickness were studied using a well-defined, 15k, four-arm star polystyrene synthesized using alkylolithium initiated anionic polymerization. For various star-branched polystyrenes, Foster and coworkers⁴ had already found that the apparent film viscosity derived from X-ray Photon Correlation Spectroscopy data for films as thick as 100 nm ($20R_g$) using a hydrodynamic continuum theory (HCT) is greater than the bulk viscosity obtained from rheometry. There still remain several questions about the mechanism by which the surface fluctuations of such branched chain melts are slowed with decreasing thickness, especially as to the particular thickness at which this anomalous slowing becomes apparent. Therefore, in this work, thin films of this 15k, four-arm star polystyrene were prepared with a wide range of thicknesses from $10R_g$ to $107R_g$ to address the threshold thickness where the polymer chains start to behave differently from how they behave in the bulk state.

Finally, the effects of branching and chain ends on the surface fluctuations of tadpole-shaped polystyrene melt films were investigated using XPCS. The results were compared with the surface fluctuation behavior of polymers with various architectures with the intent to gain insight into the effect of molecular architecture on surface dynamics. The film viscosities derived from the XPCS data using an HCT of overdamped capillary waves were compared with viscosities obtained from bulk rheology to test the validity of the HCT in this case. The result of this comparison suggests that the samples may not have been annealed to an equilibrium state before being studied at still higher temperatures. The critical thickness at which the strong slowing manifests itself was determined by measuring thin films of thickness from $10R_g$ to $80R_g$. Finally, we studied the irreversibly adsorbed layer in place after XPCS measurements by rinsing the film with a good solvent and then using X-ray Reflectometry (XR) to understand how physisorption affects surface fluctuations.

CHAPTER II

BACKGROUND

In this chapter synthetic routes for the synthesis of various types of tadpole-shaped polymers are reviewed. Then the measurement of dynamic behavior of surface fluctuations using XPCS is discussed. After that, the role of architecture, especially branching and chain ends, on physical properties is reviewed. The final part of the background is focused on research that has been done to study the irreversibly adsorbed layer and viscosity enhancement in thin polymer films.

2.1 Synthesis of Tadpole-Shaped Polystyrene

The challenges of efficient synthesis of pure tadpole-shaped polymers with well-defined structures have been an obstacle for research progress and potential applications of tadpole-shaped polymers. Generally, synthetic strategies for tadpole-shaped polymers can be classified into two categories: intermolecular coupling methods and intramolecular cyclization methods. In the intermolecular coupling, tadpole-shaped polymers are prepared by the linking of a cyclic polymer with a linear polymer. For the intramolecular cyclization methods, the precursor, usually a difunctional copolymer or a star homopolymer, is cyclized using a unimolecular “end-to-end” coupling reaction.

Syntheses of tadpole-shaped polymers have been reported by several groups. Deffieux et al.⁵ have proposed a method to synthesize tadpole-shaped polymers based on

a unimolecular “end-to-end” coupling reaction of a heterodifunctional linear polymer precursor (Figure 2.1). The synthesis involves two main steps. They first prepared a linear α -acetal- γ -styrenylpoly(chloroethyl vinyl ether-*block*-styrene) [poly(CEVE)-*b*-PS] precursor. The cationic intramolecular coupling reaction was then performed to yield the poly(chloroethyl vinyl ether-*block*-styrene) macrocyclic part of the diblock tadpole. The SEC chromatogram of the product exhibited high molecular weight species formed by intermolecular coupling of a small fraction of the chains.

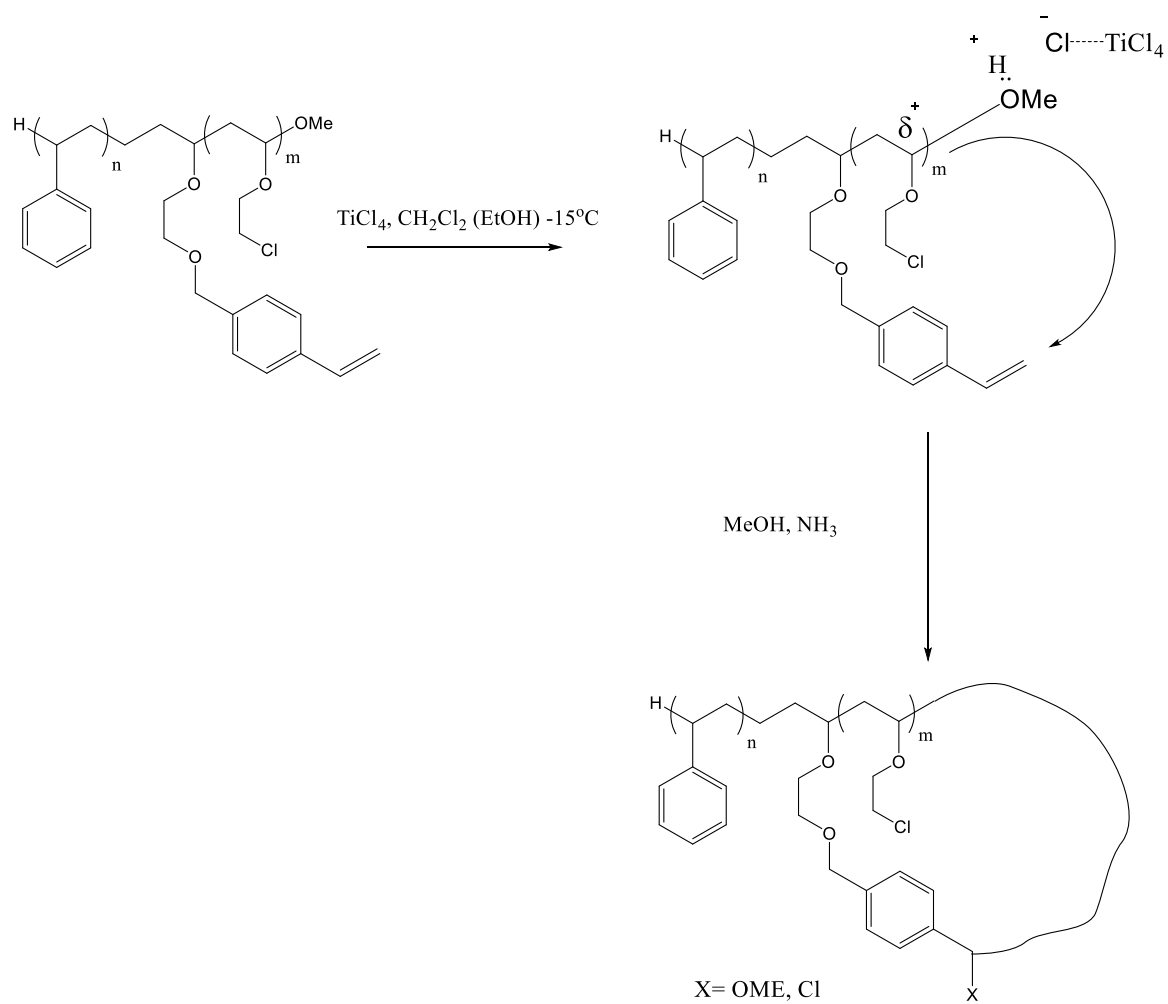


Figure 2.1. The reaction scheme for synthesis of tadpole-shaped poly(CEVE)-*b*-PS via a cationic coupling reaction of a heterodifunctional linear precursor.⁵

Tezuka et al.⁶ have reported an “electrostatic self-assembly and covalent fixation” process to synthesize tadpole-shaped polymers (Figure 2.2). A trifunctional, star-shaped polytetrahydrofuran (THF) having N-phenylpyrrolidinium ionic end groups with trifluoromethanesulfonates was synthesized first as a precursor. An ion-exchange reaction was then performed to generate star precursors carrying benzoate and terephthalate counterions at the chain ends, followed by a covalent fixation reaction to make the tadpole-

shaped poly(THF). The tadpole-shaped polymer was obtained in quantitative yield and determined to have molecular weights of 8k and 9k with polydispersity of 1.3 using GPC.

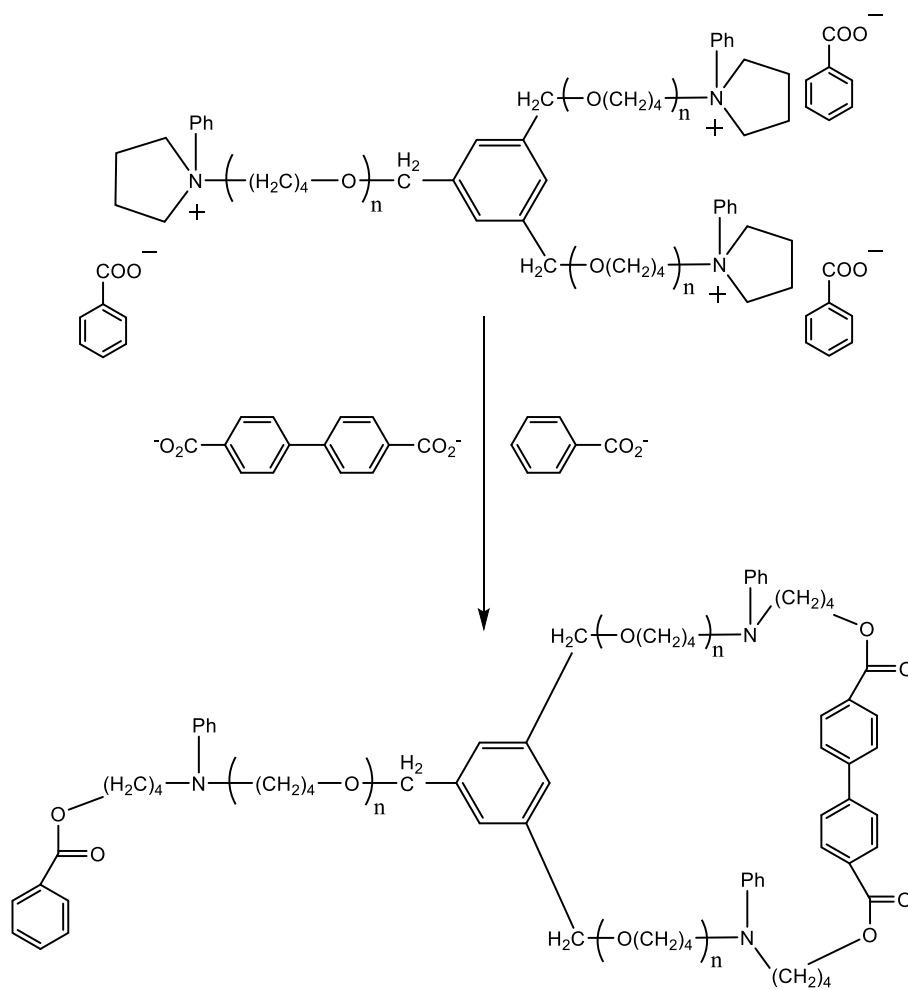


Figure 2.2. The reaction scheme for synthesis of tadpole-shaped polystyrenes via “electrostatic self-assembly and covalent fixation” process.⁶

Jerome and coworkers⁷ have tested a strategy for the synthesis of tadpole-shaped polyesters, which relied on the intramolecular photochemical cyclization of unsaturated acrylic units at both ends of precursor chains (Figure 2.3). Firstly, the precursor chain was synthesized using ring-opening polymerization of ϵ -caprolactone initiated by a cyclic tin alkoxide, followed by the addition and sequential polymerization of a few units of α -(1-

acryloxyethyl)- ϵ -caprolactone. The precursor chain then underwent photocyclization of the acrylate unit to generate a cyclic polyester with several intramolecular crosslinks. The average number of the acrylic units has decreased from 14.3 to 6.5 according to ^1H NMR analysis, which confirms the expected occurrence of the cross-linking reaction. Polymerization of ϵ -caprolactone was resumed after the cyclization to produce the tadpole-shaped polyesters with two tails. The active tin alkoxides were deactivated by a hydrolysis reaction. The molecular weight distribution of the two-tailed tadpole chains determined using GPC was broad (PDI: 1.45) and the breadth of the distribution was ascribed to the nature of ring-opening polymerization.

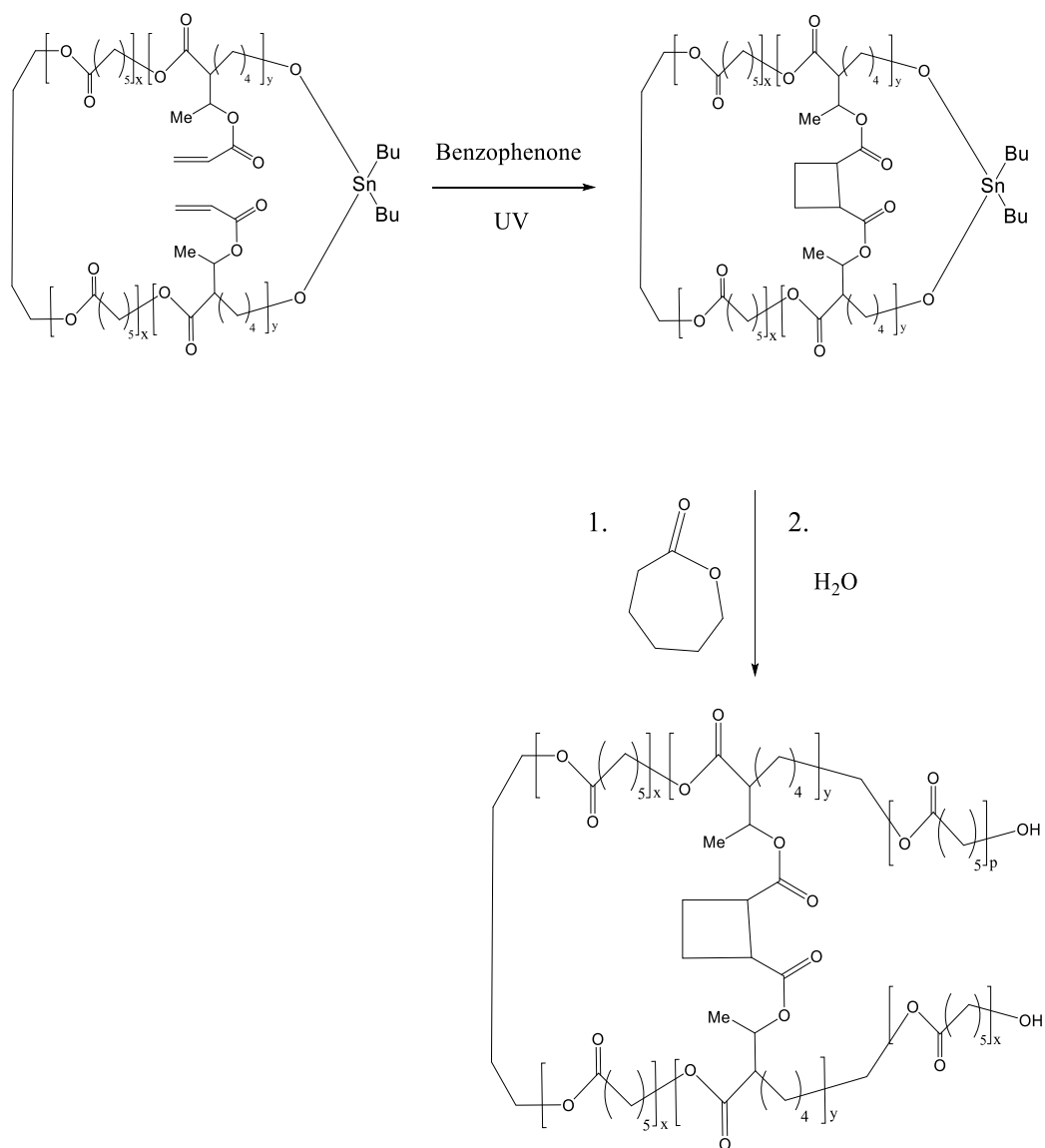


Figure 2.3. The reaction scheme for synthesis of tadpole-shaped polycaprolactone with two tails via photochemical cyclization of acrylate groups.⁷

Shi et al.⁸ have reported a “click” synthetic route to obtain a tadpole-shaped copolymer (Figure 2.4). They first used RAFT polymerization to synthesize a linear acetylene-terminated polystyrene using propargyl isobutyrate ditholbenzoate as RAFT agent. Insertion of reactive maleic anhydride into the middle of polymer chain was then

achieved by addition reaction of polystyrene living chain with maleic anhydride and following RAFT polymerization of *N*-isopropylacrylamide. Poly(*N*-isopropylacrylamide)-*b*-PS with α -acetylene at the end and ω -azido side group anchored at the junction between the two blocks was thus produced as a precursor. Intramolecular cyclization was then carried out to produce the tadpole-shaped block copolymer using “click” chemistry under high dilution. By this method they synthesized a tadpole-shaped block copolymer with a narrow molecular weight distribution (PDI: 1.03) in a yield of 60%. Similarly, Grayson’s group has synthesized a tadpole-shaped amphiphilic poly(ethylene glycol)-*b*-polycaprolactone copolymer using ring-opening polymerization and click chemistry.⁹

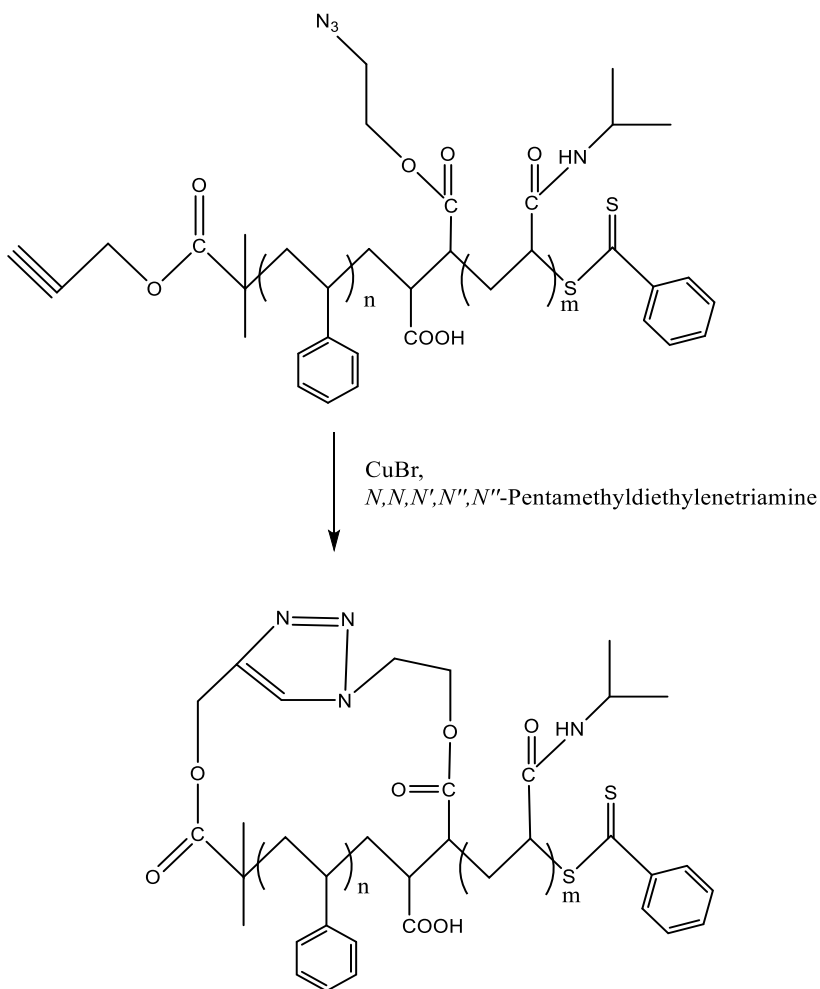
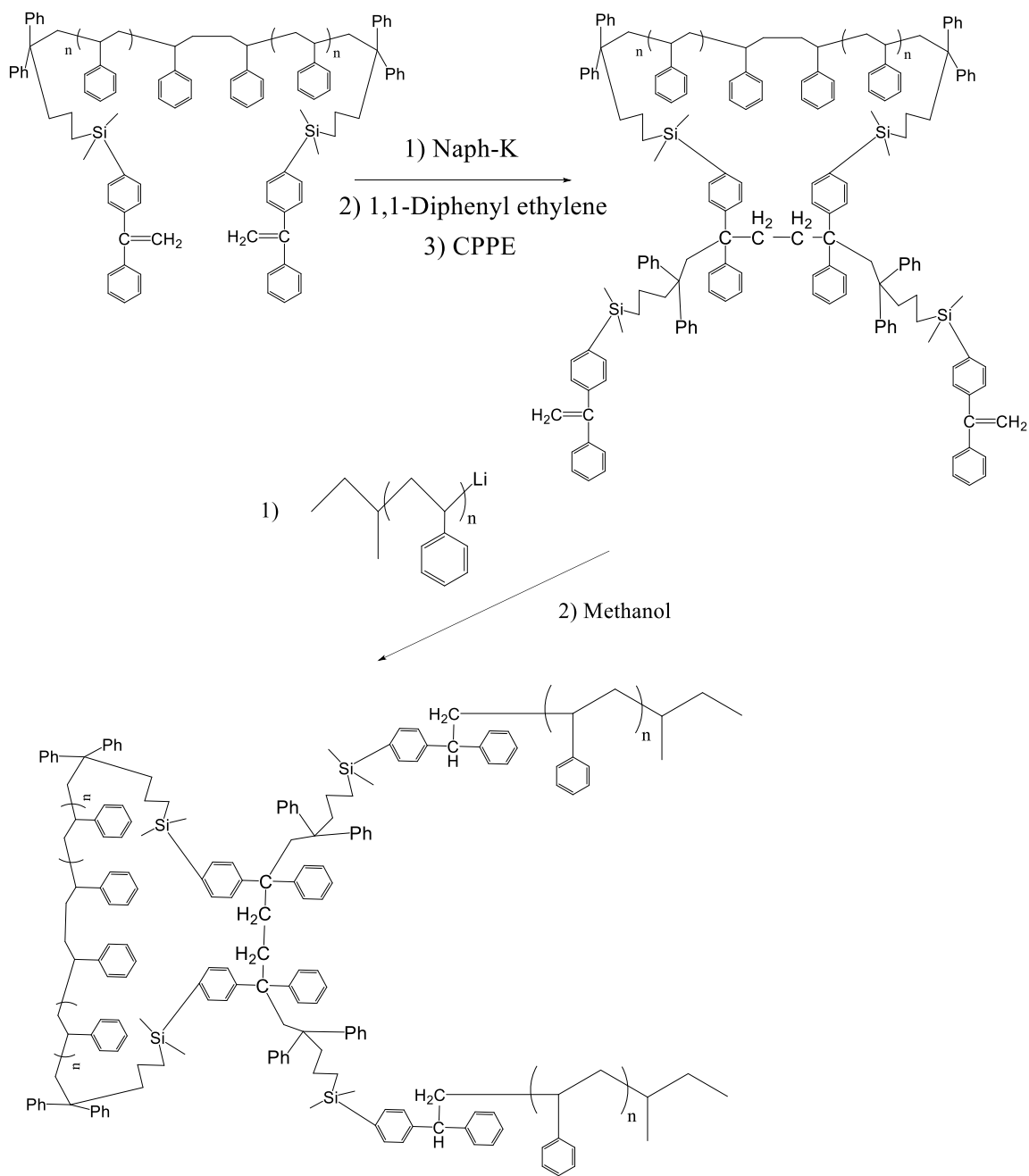


Figure 2.4. The reaction scheme for synthesis of tadpole-shaped copolymers via click cyclization chemistry.⁸

Takano et al.¹⁰ have synthesized tadpole-shaped polystyrene using a coupling reaction between ring polystyrene with two pendant 1,1-diphenylethylene groups and linear poly(styryl)lithium (Figure 2.5). The synthesis involves two steps. They first synthesized a linear polystyrene difunctional living chain initiated by potassium naphthalenide, followed by two-step end-capping reactions using 1,1-diphenylethylene and 1-[3-(3-chloropropyl)dimethylsilyl]phenyl]-1-phenylethylene (CPPE). The linear telechelic

polystyrene was cyclized using an excess amount of potassium naphthalenide as a promoter for the linking reaction. After cyclization, CPPE was added to attach two new 1,1-diphenylethylene-type double bonds to the ring polystyrene. Poly(styryl)lithium initiated by *sec*-butyllithium was synthesized and then reacted with the two pendant diphenylethylene groups to yield the tadpole-shaped polystyrene with two arms. The crude coupling product was a mixture of unreacted linear tail polymer, single-tail tadpole polymer and twin-tail tadpole polymer. Precipitational fractionation was used to obtain high-purity, single-tail, tadpole-shaped polymer in 11% yield.



CPPE = 1-[3-(3-Chloropropyldimethylsilyl)phenyl]-1-phenylethylene

Figure 2.5. The reaction scheme for synthesis of tadpole-shaped polystyrenes via a coupling reaction between a ring polystyrene with two pendant diphenylethylene groups and poly(styryl)lithium.¹⁰

These reported syntheses provided tadpole-shaped polymers with relatively large and polar junction points (not a single atom), which we conjecture could affect the molecular dynamics.¹¹ In addition, these procedures generally required extra purification steps such as multiple fractionations and HPLC. In general, the molecular characterization of these tadpole polymers was limited. Therefore, development of an efficient strategy for synthesizing well-defined, tadpole-shaped polymers with single atom junction point is still a significant challenge. The development of a multi-step method combining anionic polymerization, silicon chloride linking chemistry, and metathesis ring closure has provided efficient procedures for synthesizing well-defined macrocycles¹²⁻¹³ and eight-shaped polystyrene.¹⁴

Living anionic polymerization is useful to prepare well-defined, α - and ω -functionalized polymers.¹⁵⁻¹⁶ Anionic polymerization was first proposed by Karl Ziegler;¹⁷ he found that the addition of a monomer (styrene or butadiene) to an alkyllithium initiator occurred and the polymerization proceeded to form an active polymer chain end. Twenty years later, Szwarc and collaborators¹⁸⁻¹⁹ identified living anionic polymerization as a type of polymerization in which the chain-end remained active until terminated. Anionic polymerization is a very useful tool for predictably synthesizing polymers with well-defined structures.¹⁵ The absence of chain termination and chain transfer makes it possible to make polymers with predictable molecular weights and to prepare chain-end functional polymers. A rate of initiation comparable to the rate of polymerization allows one to prepare polymers with narrow molecular weight distribution.²⁰ Another advantage of living polymerization is that after complete consumption of monomer the active chain ends are

available to perform chain-end functionalization using electrophilic reagents.²¹ Another method for inclusion of functional groups at the ends of the polymer chains is the use of an unsaturated initiator for anionic polymerization. This was first reported by Waack and Doran²² in 1961, but the efficiency was very low for both allyllithium and vinylolithium compared to other alkylolithium initiators. The lower reactivity may be due to the resonance stability and hybridization of these initiators, as well as the aggregation effects. Later, Takano et al.²³ synthesized polystyrene using 4-pentenylolithium as initiator in the presence of a small amount of tetrahydrofuran, and they managed to get the desired molecular weight with narrow polydispersity index.

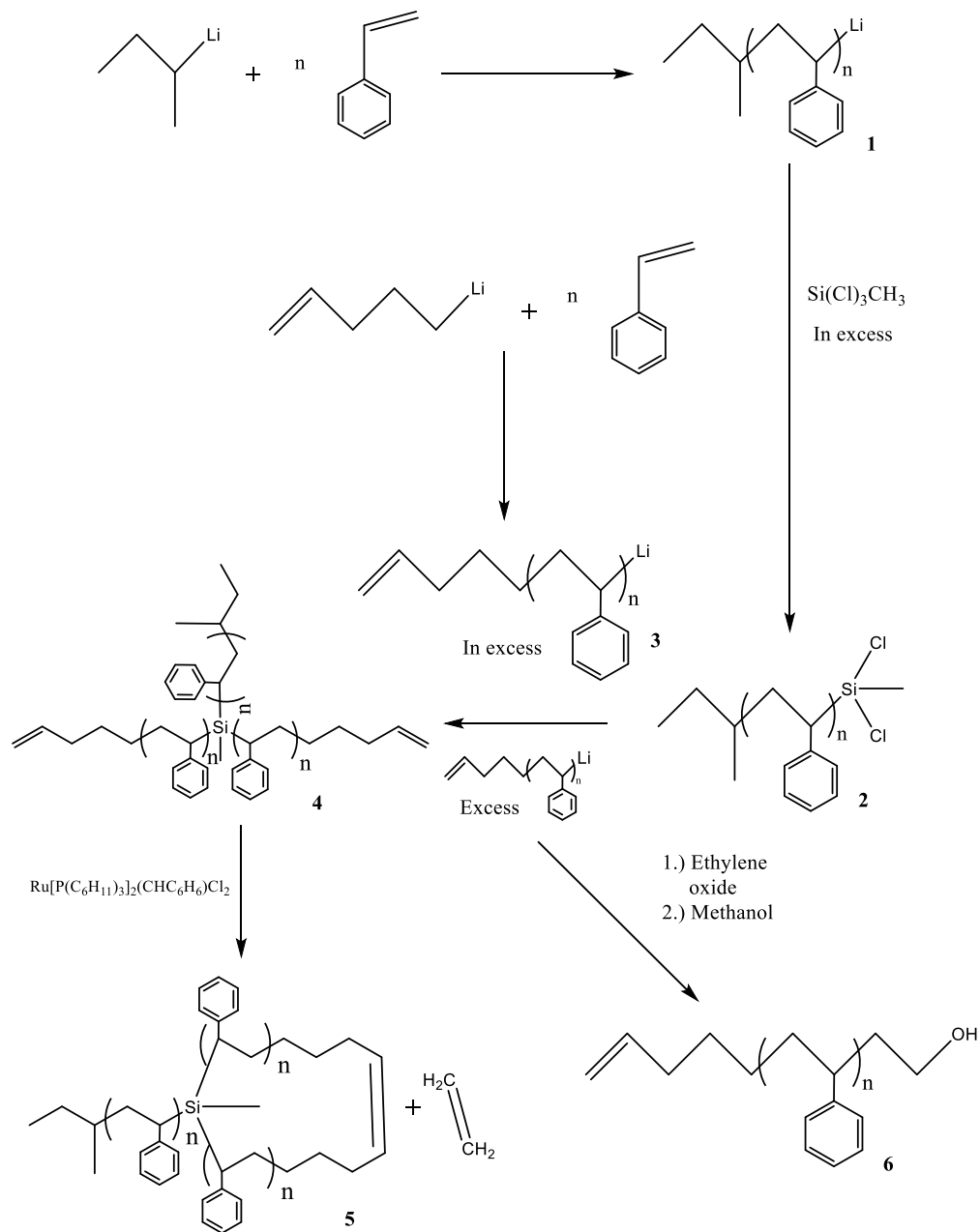
Reaction of the anionic living chain end with a multifunctional linking agent will produce star, branched, or comb polymers.²⁴ In this work, specifically, silyl chlorides were selected as multifunctional linking agents to produce polymers with branching architecture. Fetters and Bauer²⁵ and Hadjichristidis²⁶ have reported that silicon chloride linking chemistry is one of the best methods to synthesize a variety of star-branched polymers with control over molecular weight and with narrow molecular weight distributions. DeSimone and coworkers²⁷ synthesized perfluoroalkyl-terminated polymers based on high yielding reactions of polymeric organolithium compounds with silyl chlorides, and they successfully applied this synthetic methodology to various monomers (styrene and dienes). Fetters and Pennisi,²⁸ Mays,²⁹ and Mays and coworkers³⁰ have developed methods to synthesize asymmetric star copolymers using anionic polymerization and silicon chloride linking chemistry. Later work by Quirk and coworkers¹²⁻¹⁴ showed the versatility of silicon

chloride linking chemistry, which was applied to the synthesis of well-defined cyclic and 8-shaped polymers.

The metathesis ring-closure technique has been proven to be one of the most efficient ways to synthesize macrocyclic polymers. Grubbs and collaborators³¹ have developed an efficient metathesis catalyst that polymerizes cyclic dienes such as 1,5-cyclooctadiene to macrocyclic polybutadienes. The resulting polydispersity, however, is large (PDI = 2) due to intramolecular chain transfer. Using the Grubbs' 1st generation metathesis catalyst, *bis*(tricyclohexylphosphine)benzylidene ruthenium(IV) dichloride, Quirk et al.¹²⁻¹⁴ synthesized macrocyclic polymers with well-defined structure and narrow molecular weight distribution by using a multifunctional precursor with two or more double bonds.

In this work (Scheme 2.1), the synthesis method involves preparation of a macromolecular linking agent (2), which is synthesized by reacting a polymeric organolithium compound (1) with an excess of a trichloromethylsilane to generate linear polymer chains with multiple silicon chlorine bonds at the chain end (2). This macromolecular linking agent (2) can be reacted with polymeric organolithium with allyl-type end groups (3) to generate an asymmetric, three-arm, star polymer (4). Metathesis ring closure has been shown to be one of the best methods to make macrocycles from divinyl precursors.^{12-14, 32} Thus, it should be possible to prepare tadpole-shaped polymers using an asymmetric, three-arm, star polymer with two vinyl chain-end groups (4) as a precursor for metathesis ring-closure. Based on these precedents, herein we present an efficient approach to synthesize well-defined, tadpole-shaped polystyrene by a combination of living

alkyllithium-initiated anionic polymerization, silicon chloride linking chemistry, and metathesis ring closure.



Scheme 2.1. The reaction scheme for synthesis of tadpole-shaped polystyrenes using a combination of anionic polymerization, silicon chloride linking chemistry and metathesis ring closure technique.

2.2 Branching and Chain End Effects on Polymer Physical Properties

The properties of polymers of nonlinear architecture such as star and cyclic chains can be strikingly different than those of linear analogues,^{25-26, 33} both in bulk³⁴⁻³⁷ and in thin films^{4, 11, 38-39}. For example, the T_g 's of cyclic polystyrenes (PS) are substantially higher than those of linear analogues for degrees of polymerization < 400 .^{33, 40} Monteiro and coworkers⁴¹ measured T_g 's for two types of linear PS (LPS), tadpole-shaped PS (TPS), and bicyclic PS formed with a triazole junction. One of the linear chains had conventional architecture while the other was a two-arm star with a bifunctional triazole junction in the middle. They also reported that the T_g for their 10k TPS sits 1-2 °C below the T_g they expect for a cyclic analog based on comparison with T_g values for cyclics with various M reported by Hogenesch and coworkers⁴² and sits ca. 6 °C above the T_g of the linear analog based on the Kanig-Ueberreiter equation⁴³. The linking chemistry they use introduces considerable heterogeneity into the chain chemistry and the mobility around the junction point is limited. Floudas and coworkers⁴⁴ recently studied segmental dynamics for various multicyclic polystyrenes from Monteiro's group. They observed, generally, a linear increase in T_g with the number of segments adjacent to the junctions, suggesting that the bulk dynamics are strongly dependent on this number of segments constrained by being attached to the junctions. Chains with more branching points are more structurally hindered. Takano et al.³⁷ have reported that tadpole-shaped polystyrene shows a terminal relaxation that is slower than those of either the component macrocyclic ring or linear chain, and also slower than for blends in which those macrocyclic and linear components are mixed. In addition, tadpoles exhibited a drastic viscosity enhancement compared with the linear

chains, which suggests the relaxation motion of tadpole chains can be taken place with the intermolecular ring-linear penetrations. Strong effects of chain ends on surface fluctuations of melts has also been identified by Foster and coworkers.^{39, 45} Therefore, it is of interest to consider how these physical properties may differ when the architecture of the chain is changed, such as for a tadpole-shaped polymer, which may be thought of as a macrocyclic polymer with a linear tail attached.

Thermally stimulated surface fluctuations of polymer melts dictate their properties and performance, including wetting, adhesion⁴⁶ and tribology. These fluctuations are indicative of collaborative motions of chains in the whole film. For a sufficiently thick film of polymers at temperatures higher than $T_{g,bulk}$, the surface fluctuations are overdamped capillary waves.⁴⁷ X-ray Photon Correlation Spectroscopy (XPCS) has been proven to be one of the most powerful techniques to study surface fluctuations of thin films. Kim *et al.*⁴⁷ found that for entangled ($M=123k$) linear polystyrene melt films, the surface fluctuations of sufficiently thick films probed by XPCS can be well described by a hydrodynamic continuum theory (HCT).⁴⁸ They also showed that the intensity autocorrelation functions, g_2 , were reasonably well described by single exponential decays, and that the relaxation times varied with $q_{||}$, which agrees well with the overdamped capillary waves dynamics. Viscosities of the linear polystyrene films derived from the XPCS data are consistent with the literature values for bulk viscosities obtained from rheometry.

However, when a melt film is thin enough, viscosity enhancement manifest themselves and cause the deviation of the data from what is anticipated by the HCT. Gutt and coworkers⁴⁹ studied liquid films of small molecules (n-hexane and cyclohexane) and

found that the surface fluctuations were already completely suppressed for a thickness of 600 Å. The apparent viscosities of liquid films of 6-7 molecular layers thick obtained from Surface Forces Apparatus measurements can be orders of magnitude larger than the bulk viscosity due to soft solidity.⁵⁰ Later, more work was done to investigate the confinement effects on surface fluctuations of polymer melt films. Wang *et al.*⁵¹ observed confinement effects in the thin films of 90k linear polystyrene (LPS) based on X-ray scattering for the first time. They have shown the long wavelength fluctuations are strongly suppressed due to the interaction between the polymer and the substrate, which results in a lower cutoff value of scattering vector varying as function of the film thickness by studying off-specular scattering data. Later studies by Sinha and collaborators⁵² revealed a critical thickness below which the thin film behavior manifests the confinement effects. For films thicker than $4R_g$, the surface dynamics can be described as the behavior of a viscous liquid film. For films as thick as $2R_g$ the relaxation times were slower than anticipated by HCT for a purely viscous film. Thus, an elastic modulus must be introduced to describe the data. This modulus presumably originates from the pinning of the chain segments by physisorption to the substrate. For films of thickness around R_g , no surface fluctuations could be observed in the experimental window of time and wavevector.

Foster and coworkers have studied surface fluctuations for melt films of linear (LPS), cyclic (CPS) and branched polystyrenes of molecular weights below the entanglement molecular weight. Even without entanglements, for sufficiently thin films the fluctuations are slower than expected by the HCT. Compared to the work done by Sinha and collaborators for entangled linear chains, unentangled linear chains (6k) behave as

expected. The HCT captures the features of the surface fluctuations of LPS thin films as thin as 15 nm ($7R_g$). However, for a film of 14k CPS,⁴⁵ deviation from the universal behavior anticipated by HCT is observed at thickness of $10R_g$, and is even larger in the case for a film of 6k CPS ($14R_g$).³⁹ All these relative thicknesses are substantially larger than the relative thickness of LPS at which confinement effects appear. In contrast to the data of Sinha *et al.*⁵² for entangled linear chains, the shape of the τ vs. $q_{||}$ curves does not change as thickness decreases for the low molecular weight cyclic chains, suggesting that the phenomenon can be explained using an effective film viscosity higher than the bulk value. Melt films of three types of branched polystyrene chains, 6-arm pom-poms, 6 arm stars and 6-end, end-branched three arm stars, all show anomalous surface fluctuations at film thicknesses of order $20R_g$.⁴ The effective film viscosity derived from XPCS is higher than the bulk viscosity obtained from rheometry, and the discrepancy increases with increased degree of branching. It can be concluded from these results that branching and chain ends are key factors to determining the thickness at which confinement effects set in.

Based on previous results⁵¹⁻⁵² that confinement effects in the thin films are due to the physisorption of the chain segments onto the substrate, one may attempt to understand the surface fluctuations by considering the film as containing two layers: the upper layer with bulk viscosity and the bottom layer with an enhanced viscosity, with the simplest assumption being that this enhanced viscosity is taken as infinite. Taking the 6-end, end-branched polystyrene data in Foster and coworkers'⁴ work for example, if one assumes there is an extremely viscous layer next to the substrate, the thickness of this layer would have to be ca. 70 nm to rationalize the data. Therefore, many efforts have been made to

reveal the structure and physics of this layer or region of increased viscosity. Koga *et al.*⁵³ have developed a protocol where they repeatedly place the polymer film into a good solvent bath to reveal an “irreversibly adsorbed layer”. It should be noted here that this irreversibly adsorbed layer is an artificial layer with a collapsed structure, which is different from what is present in the film when it is in the melt state. However, it still allows us to gain insight for understanding polymer chain behavior near the substrate. To unveil the effect of this layer on the thin film dynamics, one must understand the kinetics of evolution of this layer. Studies of these phenomena are reviewed in the following section.

2.3 Kinetics of the Irreversibly Adsorbed Layer

The temperature and time dependent kinetics of formation of irreversibly adsorbed layers have emerged as a feature which affects thin film properties. Earlier work regarding this issue mostly focused on adsorption from dilute solutions. de Gennes⁵⁴ found that for polymers in solution contacting a solid surface, the adsorbed molecules fall into two groups where: 1. all monomers feel the same attraction towards the surface and 2. the molecules attach to the surface by one or both extremities. Later theoretical work by Shaughnessy⁵⁵ demonstrated the irreversibility of the polymer adsorption. There is a strong tendency for a dense polymer layer to form when an attractive surface contacts even a very dilute polymer solution. When the monomer sticking advantage, ϵ , exceeds $k_B T$, the relaxation times become so large that the physisorption is considered irreversible. They describe the adsorption process as consisting of two stages. In the first stage, chain adsorption happens initially by one monomer/segment contacting the surface, and the monomers/segments near the first attached one will attach next. Thus, the chain zips down from the initial graft

point. This zipping down is simultaneously accompanied by the occasional grafting of a distant monomer/segment, forming a loop, and each new graft point induces further zipping which accelerates the adsorption. Then comes the second stage, where the free surface sites become scarce and the late-coming chains can no longer zip down completely. Thus, the available sites are scattered and each group of adjacent open sites can only accommodate a certain number of monomers/segments. As the surface approaches saturation, the mean distance between available sites become so large that the late-coming chain cannot find any two adjacent sites to form a loop. Therefore, one can expect a loop size distribution in the adsorbed layer, which is the sum of a surface monolayer plus a diffuse outer part. In general, the adsorbed portions of chains show three types of conformations: trains (adsorbed segment sequences), loops (free segment sequences connecting successive trains), and tails (non-adsorbed chain ends). Although the formation of an adsorbed layer is well understood in the case of dilute solutions, the adsorption of polymer melts still remains a puzzle despite all the extensive theoretical and modeling efforts.⁵⁶⁻⁶¹ The experimental difficulties related to the characterization of buried interfaces and extremely thin polymer layers limit the understanding of the formation of the adsorbed layer.

Inspired by Guiselin's work⁶², several research groups utilized approaches combining prolonged thermal annealing with subsequent solvent leaching to uncover the adsorbed layer on the substrate surfaces.^{53, 63-67} Using X-ray reflectivity and neutron reflectivity, Koga et al.⁶⁸ reported the novel nanoscale morphology of adsorbed polymer chains at the polymer-substrate interface. They studied polystyrene adsorbed layers with different molecular weights on silicon substrates using a well-established leaching protocol

based on Guiselin's approach.⁶² The kinetics study suggests that the adsorption times (after which the thickness stops growing) for the adsorbed layers with different molecular weights (123k to 2000k) are all less than 24h. The X-ray reflectivity data can be well interpreted using a four-layer model containing two polystyrene layers of different density, and it was found that the thickness of the inner, higher density region is molecular weight independent, while the thickness of the outer, bulk-like density region increases as molecular weight increases. The results are well in line with the picture given by Shaughnessy's work.⁵⁵

Later experimental measurements by Napolitano and coworkers⁶⁷ show two regimes for the kinetics of irreversible adsorption of entangled LPS from the melt: a linear dependence of thickness on time at short times, and a logarithmic dependence at longer times. In their work, they studied the effects of annealing time and annealing temperature on the kinetics of development of the adsorbed layer. The first regime is attributed to the adsorption where chains in contact with the surface pin onto the substrate via kinetics limited by the characteristic time for the attachment of one monomer/segment. The linear growth process transitions to a logarithmic growth regime when crowding of the adsorbed chains inhibits the first order reaction mechanism. This is because the late-coming chains need to undergo severe entropy loss before diffusing through the layer already formed at the surface. The crossover time is of the order of 10 h and is molecular weight independent. They explored the time scale of annealing up to 70 h, and the thicknesses of the adsorbed layer tended to reach the plateau after this amount of time. Further work by Napolitano's group⁶⁹ reveals two mechanisms for adsorption: interfacial interactions and molecular

rearrangement. They found that the adsorption kinetics sped up upon increase of the temperature, while the adsorbed amount showed no dependence on temperature. This observation suggests different mechanisms for adsorption. They reconcile this result with the previous result showing two regimes for the kinetics of irreversible adsorption, where the first regime is related to the pinning rate only, and the later stage of adsorption depends on the velocity of incorporation of new chains limited by a repulsive interaction potential.

2.4 Mobility Gradient in Polymer Thin Films

Although thin films are considered to have a viscosity equal to that of bulk viscosity throughout the entire height of the film according to the HCT, this is not always the case. Due to the irreversibly adsorbed layer next to the substrate, the slow dynamics of this layer can propagate into the film under some circumstances, inducing slowing down of the whole film. The slow dynamics of this layer do not end abruptly at some distance away from the substrate; therefore, there is a gradient in mobility of the chains through the film. Since viscosity is an important factor dictating surface fluctuations of polymer films as describe by the HCT, a viscosity gradient study would provide more direct insight for understanding viscosity enhancement effects. Koga and collaborators⁷⁰ studied the diffusion of gold nanoparticles as markers embedded in supported PS thin films to indirectly deduce the viscosity of the films at certain depths. They prepared thin films of thicknesses ranging from 32 nm to 235 nm, and with adjustment of the incident angle (below or just above the critical angle for polystyrene), they were able to study the diffusion of the nanoparticles at the surface of the films (D_{sur}) or at the center of the films (D_{cen}) depending on from which depth of the sample the scattering signal primarily came. For thicker films, the D_{sur} and

D_{cen} values are similar, but the slightly higher D_{sur} is attributed to the reduced viscosity layer at the air interface. For the center mode for the 32 nm film, for which the region about 20 nm from the substrate is studied, almost no diffusion of the markers were observed. It should be noted that the irreversibly adsorbed layer resisting rinsing in this study was only 7 nm thick. Based on this, they claimed that the reduced mobility is due to the propagation of the slow dynamics of the irreversibly adsorbed layer. Even for a 57 nm film, the marker dynamics in the surface region are to some extent perturbed by the irreversibly adsorbed layer effect, which underscores the substrate effect on local viscosities in the thin films.

So far, results on enhancement of viscosity in thin films upon annealing and adsorption to substrates has often been discussed in the context of experimental work on confinement effects in segmental dynamics. Thus, we review here briefly some of those studies, but we point out that the viscosity may not necessarily be coupled to the segmental confinement effect. Earlier work done by Torkelson et al.⁷¹ demonstrates a novel way to determine the T_g distributions in thin films. The T_g is identified by a shift in the temperature dependence of the fluorescence of pyrene that is doped into or covalently attached to the polymer at trace levels. First, they prepared a pyrene labelled layer to place on the top of the films and examined how T_g varies as a function of the thickness of this layer placed on top. The results show that T_g approaches the bulk value as this layer placed on the film surface becomes thicker, suggesting that the segmental mobility is much faster near the surface than in the bulk of the original layer. They then exploited the fluorescence of labelled polystyrene confined in the middle of the film to measure T_g at specific depths in the multilayer films. They found that the transition from highly enhanced segmental

dynamics on the surface to bulk dynamics could extend over 36 nm for 440k PS with pyrenyl butyl methacrylate. Recently, using the same technique, Torkelson and coworkers⁷² investigated the confinement effects from both the free surface and the substrate on the stiffness changes in thin polystyrene films. The effects of confinement on interfacial perturbations were investigated using ultrathin bilayer films of 440k PS with a pyrenyl-dyed layer either at the free surface or next to the substrate. First, they confirmed the reduction in stiffness at the free surface and then verified that the molecular caging effect is significantly enhanced near the substrate. Moreover, the perturbation to caging and stiffness were found to be substantially greater in the substrate layer than in the free surface layer. However, this perturbation caused by interfaces depends strongly on confinement effects. The difference in stiffness between a 20 nm thick substrate layer and a 20 nm thick free-surface layer drastically decreases as the total film thickness decreases from 1520 nm to 40 nm, suggesting that substrate and free-surface layers impose similar effects on the molecular caging and stiffness. In other words, these two interfacial effects counteract each other over the range of depths where the perturbations or gradients from the two interfaces overlap. Further results show that the length scale associated with stiffness perturbation from the free surface is estimated to be less than 20 nm at 140 °C, while the perturbation from the substrate seems to extend over 85 nm at the same temperature. From these results, it is evident that for nanoscale thin films there is always a mobility gradient over the entire film thickness. This complicated, continuous gradient can be approximated as a step function, and even a two-step function for convenience. This is

a simplification we have employed in our work in using a two-layer model for variation of viscosity through a film.

The simplest approach to rationalizing surface fluctuations slower than expected from the HCT is to model the film of branched chains to contain a layer near the substrate with a large viscosity, conveniently approximated as infinite, with the remainder of the film exhibiting bulk viscosity. Measurements of surface fluctuations, which are dictated by hydrodynamic flow through the entire film, are not sensitive to enhanced mobility in a very thin layer at the surface.⁴⁷ Recent studies by others^{39, 53, 68, 73-77} on films of linear chains have found evidence of strong interaction between the polymer and substrate by rinsing away the vitrified film with a good solvent to yield the “strongly adsorbed” layer. This layer, which is only a fraction of the highly viscous layer that was present in the melt film, is typically of order R_g in thickness. For films of 6k cyclic chains, Foster *et al.*³⁹ have reported a strongly adsorbed layer of thickness, $h_{ads} \approx 2R_g$. XPCS data at 140 °C for various thicknesses of films of these cyclic chains collapse to a single curve using an effective film thickness, h_{eff} , defined as the actual thickness minus the thickness of a highly viscous layer, h_{vis} . At 140 °C $h_{vis} \approx h_{ads}$. However, at higher temperatures, the data collapse assuming $h_{vis} > h_{ads}$.

The “strongly adsorbed” layer thicknesses for the various branched chain films considered by Foster *et al.*⁴ have not been reported, but would not be expected to be > 10 nm, suggesting that for these architectures h_{vis} (ca. 70 nm) is substantially larger than h_{ads} . Koga *et al.*⁷⁰ have found in a ~60 nm thick film of 123k LPS with $h_{ads} = 10$ nm, the increased viscosity 30 nm from the substrate can be attributed to entanglements that propagate the

enhanced viscosity into the film. Later work by Foster and coworkers⁷⁷ showed that h_{vis} is much larger than h_{ads} in a 130k LPS film for two different substrate chemistries, with the exact thickness dependent on substrate chemistry. The propagation of the slow dynamics due to the “strongly adsorbed” layer thus depends on substrate chemistry and chain architecture and perhaps molecular weight as well. Molecular dynamics simulations by Green *et al.*⁷⁸ also suggest that for stars, a molecular layering of the melt next to the free surface may help dictate surface fluctuations, with the layering being weaker for the smaller numbers of arms (4) used in the research we report here.

Surface fluctuations of linear polymers have been studied quite a bit, and cyclic polymers have been studied as well to demonstrate the importance of chain ends. Therefore, in order to systematically investigate how molecular architecture, specifically chain ends and branching points, affects surface fluctuations, polymers with various architectures need to be made and measured to unravel the mechanism of viscosity enhancement for films containing branched chains, especially to determine the thickness at which viscosity enhancement becomes evident.

2.5 X-ray Photon Correlation Spectroscopy

For the surface of a viscoelastic fluid film, the thermally stimulated surface fluctuations are overdamped capillary waves with a relaxation time depending on the film viscosity, surface tension, film thickness and wave vector.^{48, 79} To study this phenomena, one needs to gather the information on the lateral variations in height of a surface, which requires measuring scattering from the surface for values of the scattering vector away from the specular direction, specifically, scattered intensity for a range of q_{\parallel} , the in-plane

wave vector. Additionally, one needs to measure how this scattering changes in time. In this way one can obtain information on how the surface moves spatially and temporally.

The X-ray scattering pattern as a function of q_{\parallel} resulting from the interaction between the film and a coherent X-ray beam is referred to as a “speckle pattern”. An example is shown in Figure 2.6. The speckle pattern changing over time is related to the dynamics of the surface fluctuations at certain length scales dependent on the range of q_{\parallel} probed, which is typically from 10^{-4} \AA^{-1} to 10^{-3} \AA^{-1} in this XPCS measurement. The accessible time window for this experiment ranges from 10^{-1} to 10^3 seconds, the lower limit being due to the detector readout time while the upper limit is dictated by the beamline stability. The resolution of this technique depends on the details of the instrument and the strength of the scattering. Time averaging of the speckle pattern resulting from using an acquisition time that is too long compared to the fast dynamics can smear out the pattern, making it difficult to resolve the relaxation time. Thus, the details regarding how the data are collected must be adjusted accordingly based on an estimation of the relaxation rate of the surface fluctuations. Typically, total exposure time has to be minimized to avoid beam damage, while greater total acquisition time improves statistics. The mechanics of running the XPCS measurement are similar to those of running dynamic light scattering (DLS) measurements except for the source. The coherence is much more easily obtained in photon correlation spectroscopy using visible light than that in XPCS. Therefore, with the partially coherent beam typical for XPCS measurements, high fluxes one must be used. On these premises, XPCS measurements can only be carried out at a synchrotron with high flux and

brightness (3rd generation synchrotrons). With the smaller wavelength, $\lambda \sim 1 \text{ \AA}$, used in XPCS, the length scales probed are smaller than those probed in DLS.

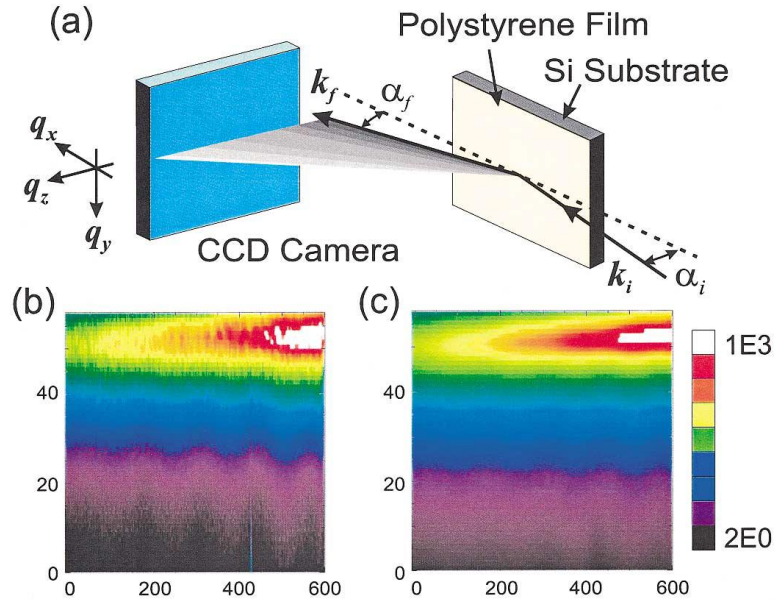


Figure 2.6. (a) Schematic illustration of the geometry for XPCS. (b) Speckle pattern of time averaged diffuse scattering measured using XPCS. (c) Speckle pattern from the fit to capillary wave model for a molten LPS sample. Reproduced with permission.⁴⁷ Copyright 2003, American Physical Society.

The thermally stimulated surface fluctuations are isotropic for a liquid surface. The scattering intensity at one specific point in the speckle pattern resulting from such surface fluctuations, which evolves with time, can be recorded using a 2-D position sensitive detector. Specifically, a charge-coupled device is used in this study (Figure 2.6). The speckle pattern is recorded as a “frame” after a certain amount of time of exposure to X-rays, which is similar to a frame in a movie. Thus, the time correlation of the frames can be obtained by comparing the intensities at a particular position on the detector separated by specific intervals in time, which are referred as the “delay times”. The time evolution

of the scattering intensity at a certain value of q_{\parallel} that quantifies the dynamics of the surface at the corresponding length scales is described using a normalized intensity-intensity time autocorrelation function, $g_2(q_{\parallel}, t')$, defined as

$$g_2(q_{\parallel}, t) = \frac{\langle I(q_{\parallel}, t')I(q_{\parallel}, t+t') \rangle}{\langle I(q_{\parallel}, t+t') \rangle^2}, \quad (2.1)$$

where $I(q_{\parallel}, t')$ is the scattering intensity at q_{\parallel} at time t' , and the angular brackets refer to ensemble averages for a fixed delay time, t . A single exponential decay, $g_2 = 1 + \beta \exp(-2t/\tau)$ with relaxation time τ ,⁸² provided a good fit to the g_2 function decay for the overdamped capillary waves. In an ideal case, in which a totally coherent incident beam is achieved, the speckle contrast factor, β , equals 1. In fact, however, β , is much less than 1 in the real case. In principle, β is a sample-independent parameter only related to the coherence of the incident beam and infinite detector acceptance.⁸⁰

As mentioned before, the relaxation time depends on film viscosity, surface tension, film thickness and in-plane wave vector based on the HCT.^{47, 79} When a nonslip boundary condition is applicable at the film-substrate interface and thickness is sufficiently large, the normalized relaxation time, τ/h is given as a function of normalized scattering vector, $q_{\parallel}h$:

$$\frac{\tau}{h} = \frac{2\eta[\cosh^2(q_{\parallel}h) + (q_{\parallel}h)^2]}{\gamma q_{\parallel}h[\cosh(q_{\parallel}h)\sinh(q_{\parallel}h) - q_{\parallel}h]}. \quad (2.2)$$

As the film becomes thicker, the nonslip boundary condition becomes less important and the surface fluctuations approach an asymptotic behavior for large thickness. However,

equation 2.2 describes a universal behavior where the data for τ/h as a function of dimensionless scattering vector $q_{\parallel}h$ should overlap onto a single curve for different thicknesses. When the normalized data deviate from the universal curve, one may say that confinement effects are present.

CHAPTER III

EXPERIMENTAL

3.1 Requirements for Air Sensitive Materials

Impurities in the anionic polymerization systems can deactivate the initiator and living chain, leading to a broad molecular weight distribution and lack of molecular weight control. To prevent impurities including oxygen, carbon dioxide and moisture from being in the reaction, standard high vacuum techniques, dry box manipulation and purification of chemical agents are required for anionic polymerization.^{20, 81-82}

3.1.1 High Vacuum Techniques

Specially designed apparatus and an appropriate high vacuum line are needed to exclude from the reaction all contaminants that react with anionic centers. In order to get a polymer with a narrow molecular weight distribution and controlled molecular weight, all anionic polymerizations were carried out in an all-glass, sealed apparatus on a high vacuum line.

High vacuum was produced by the combination of a mechanical pump (Edwards RV-8) and an oil diffusion pump (ChemGlass). The volatile material was condensed in the liquid nitrogen trap to protect the pumps from contamination. In addition to these two parts, there were the upper and lower glass manifolds connected by two glass tubes with stopcocks, which constitute the complete high vacuum line, as shown in Figure 3.1.

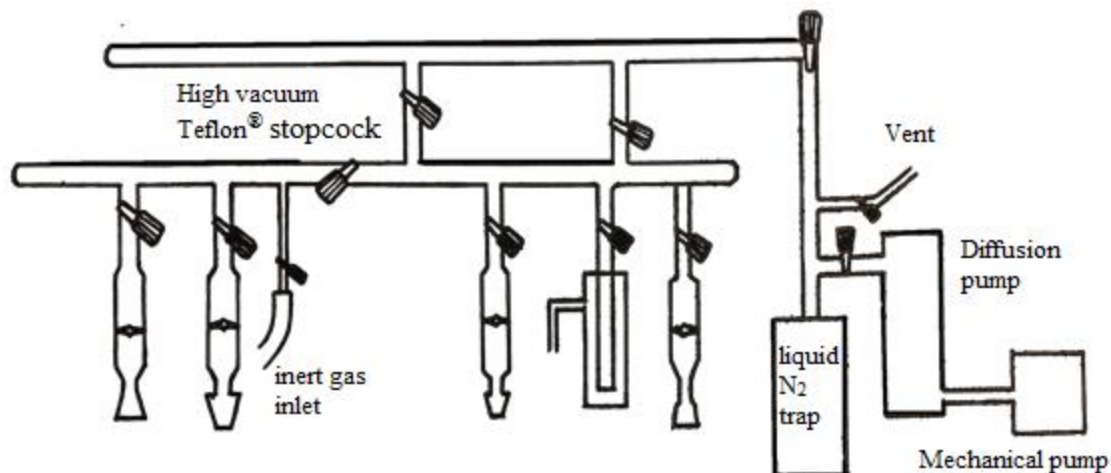


Figure 3.1. Illustration of a glass high vacuum line for purification and anionic polymerization.

The high vacuum was tested using a Tesla coil by putting the side of the tip close to the high vacuum line. The absence of an arc and noise from the interaction of the Tesla coil with the vacuum system are indications that the pressure inside the system is lower than 10^{-3} mm Hg.²⁰ Proper maintenance is essential for the pump efficiency and longevity, so one needs to make sure the oil stays at the proper level in each pump and that the oil for the mechanical pump is changed regularly.

3.1.2 Dry Box Manipulation

An inert atmosphere is required for the handling of those chemical agents that are sensitive to air.⁸³⁻⁸⁴ A Vacuum Atmospheres Model HE-43-2 glove box provides such an argon gas atmosphere for transfers and weighing. Figure 3.2 shows a general view of the glove box used in the experiments. The purification system for the glove box was a column

packed with molecular sieves (4\AA) and a copper catalyst [13 wt% of Cu(II) oxide on alumina]. Regeneration was accomplished by purging with 5% hydrogen in nitrogen to reduce the catalyst and to remove the resident water vapor and oxygen. Equipment and chemicals were brought into the glove box through an antechamber, which was pumped and refilled with argon gas at least three times before moving items into the dry box. The condition of the atmosphere in the dry box was checked using the Sekutowshi and Stucky method.⁸⁵ The solution of $(\text{Cp}_2\text{TiCl})_2\text{ZnCl}_2$ exposed to the dry box atmosphere remains green if the oxygen level is less than 5 ppm in the dry box, while turning red or orange indicates that the oxygen level is above 5 ppm, and that the regeneration protocol was needed.

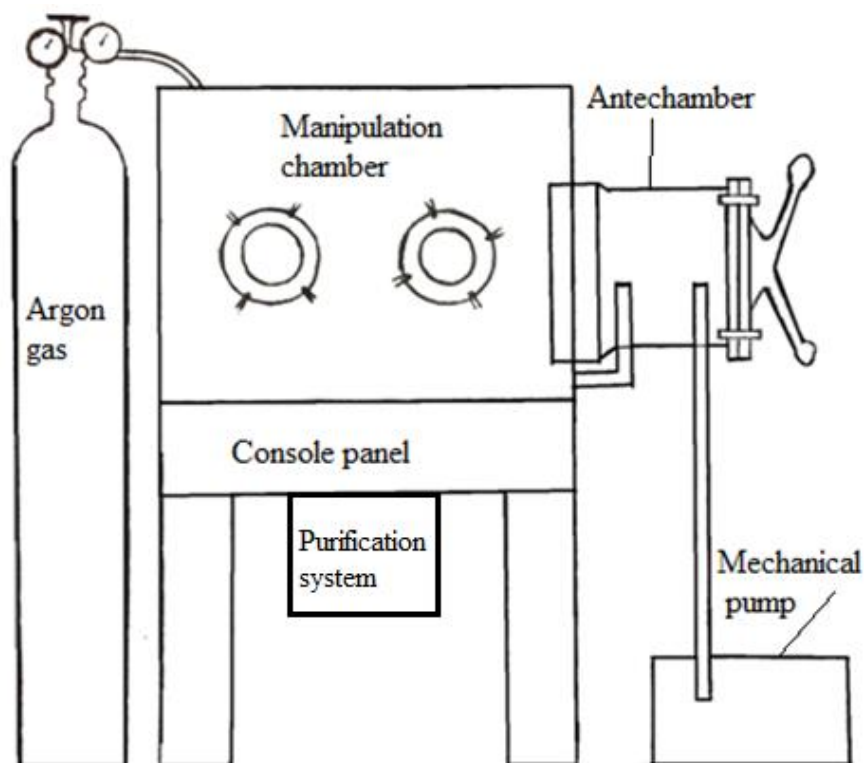


Figure 3.2. General view of vacuum glove box and air lock.

3.2 Purification of Materials

All chemical reagents used in anionic polymerization were purified to protect the initiator and living anionic chain ends. The purification of solvents, monomers and terminating agents used for anionic polymerization as well as the handling of the initiator and ring-closure agents are discussed in this section.

3.2.1 Solvents

Solvents were purified using stringent procedures and stored in the proper way described below to ensure the absence of reactive impurities.

3.2.1.1 Benzene and Heptane

Benzene (ACS grade, EMD; 99%) or heptane (EMD; 99%) was stirred in a flask with freshly crushed calcium hydride (Sigma-Aldrich, 95%) overnight under vacuum. The mixture was degassed in the vacuum line using three freeze-pump-thaw cycles in a dry ice/isopropyl alcohol bath (-78 °C). After degassing, the solvent was transferred into a flask with a sodium metal dispersion using vacuum distillation. The solvent was stirred overnight. Finally, the purified solvent was distilled into a storage flask with a Rotoflo® stopcock containing oligomeric poly(styryl)lithium, which remained red if no reactive impurities were present. Purified solvent was freshly distilled from this flask into ampoules or a reactor when needed.

3.2.1.2 Tetrahydrofuran and Diethyl Ether

Tetrahydrofuran (THF) (ACS grade, Fisher Scientific, >95%) or diethyl ether (EMD, 99%) was stirred in a flask with freshly crushed calcium hydride (Sigma-Aldrich, 95%) overnight under vacuum. The mixture was degassed three times on the vacuum line using freeze-pump-thaw cycles. It was frozen using an isopropyl alcohol/dry ice bath (-78 °C). After degassing the solvent was transferred into a flask containing a sodium metal dispersion using vacuum distillation. The solvent was stirred overnight. Finally, the solvent was transferred into a storage flask with a Rotoflo[®] stopcock containing a sodium mirror. Persistence of the sodium mirror indicated that the solvent was free of reactive compounds. Purified THF was stored in a dark place and was freshly distilled from this flask into ampoules when needed.

3.2.1.3 Dichloromethane

Dichloromethane (ACS grade, Fisher Scientific, >95%) was stirred in a flask with freshly crushed calcium hydride (Sigma-Aldrich, 95%) overnight under vacuum. The mixture was degassed three times on the vacuum line using freeze-pump-thaw cycles. It was frozen using an isopropyl alcohol/dry ice bath (-78 °C). After degassing the solvent was transferred into a flask containing calcium hydride dispersion using vacuum distillation and stirred overnight. The purified solvent was distilled into a storage flask with a Rotoflo[®] stopcock. Purified solvent was distilled from the flask into the ampoules or reactors when needed.

3.2.2 Monomer

In this work, the only monomer used were styrene and isoprene. At room temperature, styrene can easily polymerize, so inhibitor is added before shipment to prevent it from reacting. Therefore, purification is required before reaction to remove inhibitors and impurities.

3.2.2.1 Styrene

Styrene (Aldrich, 99%) was stirred in a flask with freshly crushed calcium hydride (Sigma-Aldrich, 95%) overnight under vacuum. The mixture was degassed three times on the vacuum line using freeze-pump-thaw cycles. It was frozen using a liquid nitrogen bath (-196 °C). After degassing, the purified monomer was transferred into a storage round-bottom flask equipped with a Rotoflo® stopcock and containing neat dibutylmagnesium (FMC Lithium Division, 17% in heptanes). Purified styrene was freshly distilled from the flask into reactors or ampoules that were stored in the refrigerator.

3.2.2.2 Isoprene

Isoprene (Goodyear, >99%) was stirred in a flask with freshly crushed calcium hydride (Sigma-Aldrich, 95%) overnight under vacuum. The mixture was degassed three times on the vacuum line using freeze-pump-thaw cycles. It was frozen using a liquid nitrogen bath (-196 °C). After degassing, the purified monomer was transferred into a storage round-bottom flask equipped with a Rotoflo® stopcock and containing neat

dibutylmagnesium (FMC Lithium Division, 17% in heptanes). Purified isoprene was freshly distilled from the flask into reactors or ampoules which were stored in the refrigerator.

3.2.3 Terminating Agents

The terminating agents were used to react with the living chains to terminate carbanion chain end or to achieve functionalization. The detailed purification procedures of these terminating agents will be discussed in this section.

3.2.3.1 Methanol

Methanol (Fisher Scientific, reagent ACS, 99.8%) was degassed three times on the vacuum line using freeze-pump-thaw cycles. It was frozen using a liquid nitrogen bath (-196 °C). After degassing the methanol was transferred into ampoules with break-seals. The ampoules were removed from the vacuum line using flame-sealing.

3.2.3.2 Methyltrichlorosilane

Methyltrichlorosilane (Sigma-Aldrich, >99.5%) was distributed in a flask with freshly crushed calcium hydride (Sigma-Aldrich, 95%) in the dry box and stirred under the vacuum line overnight. The mixture was degassed three times on the vacuum line using freeze-pump-thaw cycles. It was frozen using a liquid nitrogen bath (-196 °C). After degassing the reagent was transferred into a flask containing calcium hydride and stirred overnight. The middle fraction of the purified methyltrichlorosilane was distilled into

ampoules with break-seals and then diluted by benzene and degassed.⁸⁶ The ampoules were then removed from the vacuum line using flame-sealing and were stored in the refrigerator.

3.2.3.3 Tetrachlorosilane

Tetrachlorosilane (Sigma-Aldrich, 99%) was distributed in a flask with freshly crushed calcium hydride (Sigma-Aldrich, 95%) in the dry box and stirred under the vacuum line overnight. The mixture was degassed three times on the vacuum line using freeze-pump-thaw cycles. It was frozen using a liquid nitrogen bath (-196 °C). After degassing the reagent was transferred into a flask containing calcium hydride and stirred overnight. The middle fraction of the purified tetrachlorosilane was distilled into ampoules with break-seals and then diluted by benzene and degassed. The ampoules were then removed from the vacuum line using flame-sealing and were stored in the refrigerator.

3.2.3.4 1,2-*bis*(Methyldichlorosilyl)ethane

1,2-*bis*(Methyldichlorosilyl)ethane (Gelest) was distributed into a round-bottom flask with a Rotoflo[®] stopcock containing calcium hydride in the dry box and stirred over calcium hydride (95%, Sigma-Aldrich) on the vacuum line at 40 °C, distilled into an ampoule through short-path, and transferred into the dry box. After the linking agent was diluted with benzene, the solution was transferred into an ampoule with a Rotoflo[®] stopcock. The ampoules were then connected to the high vacuum line. After three freeze-pump-thaw cycles in an isopropyl alcohol/dry ice bath, the ampoules were removed from the line by flame-sealing.

3.2.3.5 Trichloromethylsilane

Trichloromethylsilane (Sigma-Aldrich, >97%) was stirred in a flask with freshly crushed calcium hydride overnight under vacuum. The mixture was degassed three times on the vacuum line using freeze-pump-thaw cycles. It was frozen using a liquid nitrogen bath (-196 °C). After degassing the reagent was transferred into a flask containing calcium hydride and stirred overnight. The middle fraction of the purified trichloromethylsilane was distilled into ampoules with break-seals, which were then removed from the vacuum line using flame-sealing. The ampoules of trichloromethylsilane were stored in the refrigerator.

3.2.3.6 Ethylene oxide

Ethylene oxide (Aldrich, >99.5%) was transferred through the high vacuum line into a round bottom flask with ground calcium hydride in an isopropyl alcohol/dry ice bath. The isopropyl alcohol/dry ice bath was then replaced by water/ice bath and the mixture was stirred for 2h at 0 °C. The purified ethylene oxide was transferred into a flask equipped with a Rotoflo[®] stopcock and containing neat dibutylmagnesium, and stirred for another 2h at 0 °C. Then it was vacuum distilled into ampoules with break-seals and diluted with benzene.⁸⁷ The ampoules were degassed three times on the vacuum line using freeze-pump-thaw cycles, using a liquid nitrogen bath (-196 °C). The ampoules were sealed off using flame-sealing and stored in the refrigerator.

3.2.4 Initiator Materials

5-Lithio-1-pentene was the initiator used to synthesize polystyrenes with α -vinyl functionalization. The materials used to synthesize the initiator were lithium metal and 5-bromo-1-pentene. The procedures to purify these chemicals will be discussed in this section.

3.2.4.1 5-Bromo-1-pentene

5-Bromo-1-pentene (Aldrich, 95%) was distilled into a flask with freshly crushed calcium hydride, and then stirred overnight. The mixture was degassed three times on the vacuum line using freeze-pump-thaw cycles. It was frozen using liquid nitrogen (-196 °C). After degassing the reagent was fractionally distilled into a flask with a Rotoflo® stopcock. The middle fraction was collected in a calibrated ampoule, flame sealed from the vacuum line and stored in the refrigerator.

3.2.4.2 Lithium

Lithium metal (Sigma-Aldrich, stabilized, 1% Na) was stored in the dry box. The lithium particles were transferred in the dry box to a reactor and then degassed on the vacuum line before reaction.

3.2.4.3 Allyl bromide

Allyl bromide (Sigma-Aldrich, 99%) was distilled into a flask with freshly crushed calcium hydride, and then stirred overnight. The mixture was degassed three times on the vacuum line using freeze-pump-thaw cycles. It was frozen using liquid nitrogen (-196 °C).

After degassing the reagent was distilled into a flask with a Rotoflo® stopcock before transferred into the glove box.

3.2.5 Ring-closure Catalyst

In the step of end-to-end cyclization of the linear telechelic precursor, the Grubbs first generation catalyst $(\text{Ru}[\text{P}(\text{C}_6\text{H}_{11})_3]_2(\text{CHC}_6\text{H}_6)\text{Cl}_2)^{30}$ was used to catalyze the cyclization reaction.

3.2.5.1 Grubbs Catalyst

The 1st generation Grubbs catalyst, *bis*(tricyclohexylphosphine)benzylidene ruthenium (Aldrich, 97%), was dissolved in purified dichloromethane and then the solution was poured into an ampoule in the dry box. The ampoule was connected to the vacuum line and degassed three times using freeze-pump-thaw cycles and a liquid nitrogen bath. Finally, the ampoule was removed from the vacuum line by flame-sealing.

3.3 Synthesis of Tadpole-shaped Polystyrene

3.3.1 Synthesis of 5-Lithio-1-pentene²³

The reactor used is shown in Figure 3.3. A 150-mL, Morton-creased, glass reactor equipped with a break-seal (C), a septum-sealed side arm (E) and ampoules of diethyl ether (20 mL, A), 5-bromo-1-pentene (6.5 mL, 0.055 mol, B), and a medium porosity fritted glass filter (F) connected to an empty ampoule was transferred into the dry box. Lithium

(3.6 g, 0.52 mol) was added to the reactor through the side arm which was then plugged using a rubber septum. The reactor was removed from the dry box and connected to the vacuum line through a break-seal (D). After flame-sealing the side arm, heptane (50 mL) was distilled into the reactor and then the break-seal of the 5-bromo-1-pentene ampoule was smashed. The mixture was stirred for three days at room temperature, and then the reactor was cooled to 0 °C with an ice-water bath. The break-seal of the diethyl ether ampoule was smashed and the mixture was stirred for another 24 h at 0 °C. The reactor was reconnected to the vacuum line through a break-seal. The break-seal was smashed and the solvent was stripped off through the vacuum line. Another batch of heptane (~50 mL) was distilled into the reactor and the mixture was filtered into the empty ampoule (G) through the fritted glass filter. The reactor was rinsed by back-distilling heptane using an isopropyl alcohol/dry ice cooling bath and transferring back through the filter. The ampoule containing this functionalized initiator solution was then flame-sealed from the reactor and transferred into the dry box. The initiator solution was diluted with heptane (~50 mL) and distributed into two crimp-cap bottles and sealed. The concentration of the 5-lithio-1-pentene initiator was determined using double titration.⁸⁸ The aliquots (1 mL each) of the initiator solution were injected into six crimp-cap bottles. Three of them were quenched using 1 mL of distilled water in each. The other three were quenched using 1 mL of allyl bromide in each followed by addition of 1 mL of distilled water in each. The solutions were titrated with 0.1 M standard hydrochloric acid solution (Sigma-Aldrich) using phenolphthalein (Sigma-Aldrich) as the indicator. The difference between the two

titrations indicated the amount of the initiator. The initiator concentration was determined to be 0.24M.

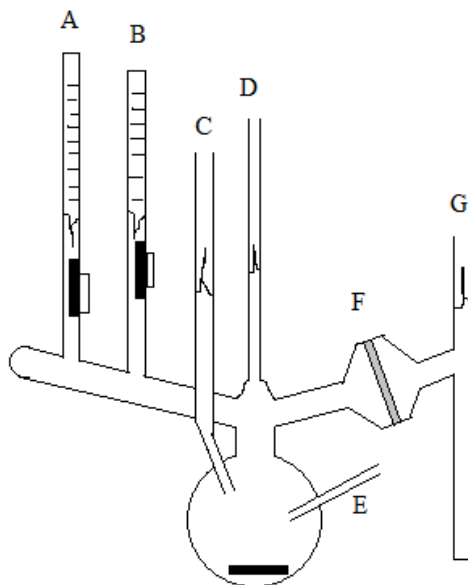


Figure 3.3. Illustration of reactor to synthesize 5-lithio-1-pentene.

3.3.2 Synthesis of ω -Methyldichlorosilylpolystyrene

The two reactors used are shown in Figure 3.4. All polymerizations were conducted in all-glass apparatus using standard high vacuum techniques. A 150-mL, glass reactor equipped with a septum-sealed side arm, ampoules of styrene (5 mL, 4.55 g, 43.7 mmol, A), methanol (~2 mL, C), and an empty storage ampoule (D) with a stopcock was connected to the high vacuum line (B). *sec*-Butyllithium (1.9 mL, 2.27 mmol) was added into the reactor through the side arm using a gas-tight syringe under a flowing nitrogen atmosphere. After flame-sealing the side arm, benzene (100 mL) was vacuum distilled into the reactor. The reactor was then flame-sealed from the vacuum line and the break-seal of the styrene ampoule was smashed. The reactor was placed in a water bath at 25 °C for 2 h

and then 35 mL of the poly(styryl)lithium solution was transferred into the stopcock-sealed storage ampoule (D) which was then flame-sealed from the reactor. The remaining poly(styryl)lithium was quenched with methanol for characterization.

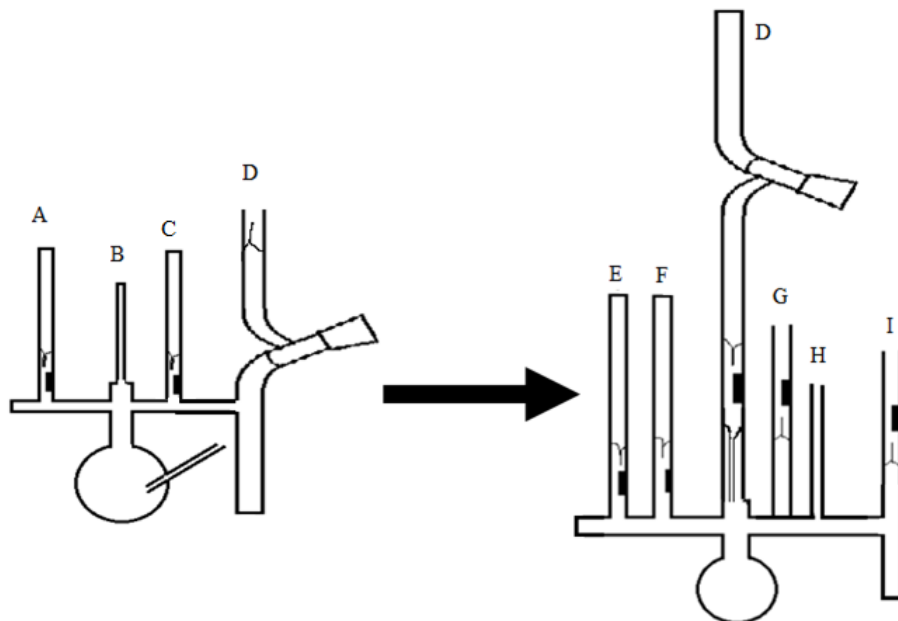


Figure 3.4. Illustration of the reactors used to synthesize the ω -methyldichlorosilylpolystyrene.

A 250-mL, Morton-creased, glass reactor equipped with ampoules of poly(styryl)lithium solution (35 mL, 0.8 mmol, D), methyltrichlorosilane (2.9 mL, 24 mmol, E), benzene (20 mL, F), an empty storage ampoule (I) and a teflon stir bar was connected to the high vacuum line (H). Benzene (15 mL) was distilled into the reactor and the reactor was separated from the vacuum line by flame-sealing. The break-seal of the methyltrichlorosilane ampoule was broken and the solution was stirred at 0 °C for 10 min. The break-seal of the poly(styryl)lithium (I) solution was then broken and the solution was slowly added to the methyltrichlorosilane solution by adjusting the stopcock. The reactor

was reconnected to the vacuum line through a break-seal (G) after decolorization of the solution. The solvent was removed by three freeze-dry processes using benzene as solvent and then the reactor was flame-sealed from the vacuum line. The break-seal of the benzene ampoule was broken and the resulting solution was transferred into the storage ampoule (I) and flame-sealed. The product was 0.8 mmol in benzene.

3.3.3 Synthesis of Asymmetric, Three-arm, Star Polystyrene

The reactor used is shown in Figure 3.5. A 150-mL, Morton-creased, glass reactor equipped with a septum-sealed side arm, ampoules of styrene (5.5 mL, 5 g, 48 mmol, A), THF (1 mL, 12.3 mmol, B), ω -methyldichlorosilylpolystyrene solution (0.8 mmol in benzene, C), ethylene oxide (1 mL in 5 mL of benzene, 20 mmol, F), and methanol (~2 mL, G) was connected to the vacuum line (D). The 5-lithio-1-pentene initiator (10.5 mL, 2.52 mmol) was injected into the reactor via the side arm (E) using a gas-tight syringe under a flowing nitrogen atmosphere followed by flame-sealing of the side arm under high vacuum. Then benzene (100 mL) was distilled into the reactor cooled with a dry ice/isopropyl alcohol bath before it was removed from the line by flame-sealing. The break-seals of the THF and styrene ampoules were smashed sequentially after the reactor was warmed to room temperature. The reactor was cooled to 0 °C and stirred for 3 h. An aliquot of the α -4-pentenylpoly(styryl)lithium (α -PSLi) solution was transferred into an empty ampoule equipped with a methanol ampoule, flame-sealed from the vacuum line, and later quenched using methanol for characterization. The break-seal of the ω -methyldichlorosilylpolystyrene ampoule was smashed and the mixture was stirred at 0 °C for 24 h. The break-seal of the ethylene oxide ampoule was smashed and the mixture was

stirred for 10 min. The methanol ampoule break-seal was then smashed and all of the solvent was removed using a rotary evaporator. The crude product was dissolved in toluene (~2 mL) and precipitated into methanol (~40 mL). The asymmetric, three-arm, star polystyrene was purified by silica gel chromatography using toluene as eluent. The powder was dried in a high vacuum oven overnight before characterization using ^1H NMR, SEC, and MALDI-ToF mass spectrometry (MALDI-MS).

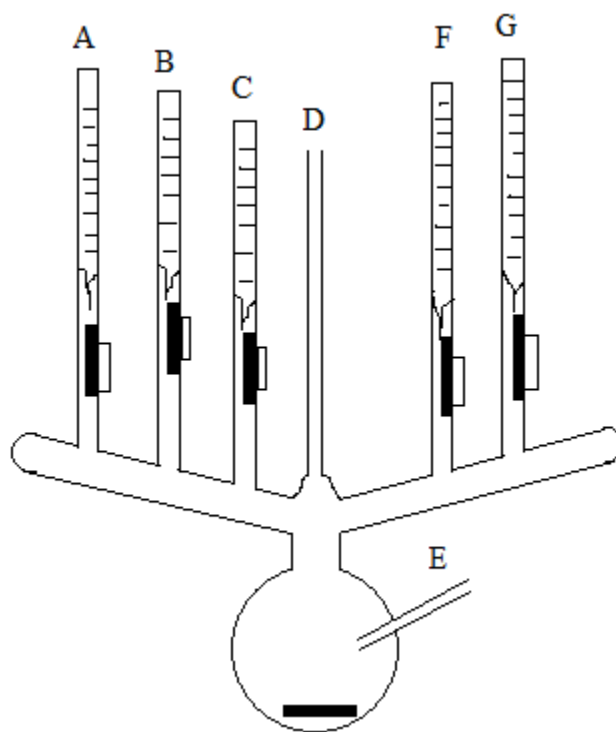


Figure 3.5. Illustration of the reactor used to synthesize the asymmetric, three-arm, star polystyrene.

3.3.4 Synthesis of Tadpole-Shaped Polystyrene

The reactor used is shown in Figure 3.5. The asymmetric, three-arm, star polystyrene (**4**, 400 mg, 0.067 mmol; $M_n = 6000$ g/mol, A) and *bis*(tricyclohexylphosphine)benzylidineruthenium(IV) chloride (123 mg, 0.15 mmol, C) were each dissolved in dichloromethane (20 mL) and distributed into separate ampoules with stopcocks in the dry box. The ampoules were then taken out of the dry box and connected to the vacuum line (B). Both solutions were degassed using three freeze-pump-thaw cycles in a liquid nitrogen bath and were then removed from the vacuum line by flame-sealing. A 2-L glass reactor equipped with the two ampoules was connected to the vacuum line and dichloromethane (1 L) was vacuum distilled into the reactor. The reactor was then removed from the vacuum line by flame-sealing and warmed to room temperature. The break-seals of the asymmetric, three-arm, star polystyrene (**4**) and the ruthenium catalyst ampoules were smashed sequentially. The mixture was stirred at 40 °C for 24 h before the solution was exposed to air to deactivate the catalyst.¹²⁻¹⁴ After removing the solvent using a rotary evaporator, the residual catalyst was removed by alumina (neutral, Sigma-Aldrich) column chromatography using toluene as eluent. The product was dissolved in 10 mL of toluene, precipitated into methanol and dried in a high vacuum oven overnight before characterization using ¹H NMR, SEC, and MALDI-ToF MS.

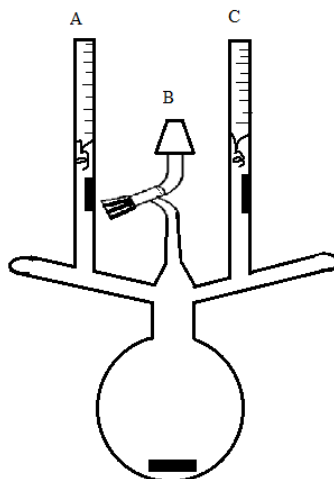


Figure 3.6. Illustration of the reactor used to synthesize the tadpole-shaped polystyrene

3.3.5 Synthesis of *tris*(α -4-Pentenylpolystyryl)methylsilane

The reactor used is shown in Figure 3.6. A 150-mL, Morton-creased, glass reactor equipped with a septum-sealed side arm, ampoules of styrene (2.9 mL, 2.639 g, 25.5 mmol, A), 4-pentenyllithium (9.2 mL, 0.45M, 4.2 mmol, B), THF (3.3 mL, 2.937 g, 40.7 mmol, C), trichloromethylsilane (0.8 mL, 1 mmol, E), ethylene oxide (1 mL in 5 mL of benzene, 20 mmol, F), and methanol (~2 mL, G) was connected to the vacuum line (D). Benzene (100 mL) was distilled into the reactor cooled with a dry ice/isopropyl alcohol bath before it was removed from the line by flame-sealing. The break-seals of the initiator (4-pentenyllithium), THF and styrene ampoules were sequentially smashed after the reactor was warmed to 0 °C. The reactor was stirred for 1 h. The break-seal of the trichloromethylsilane ampoule was smashed and the mixture was stirred at 0 °C for 1h. Then the break-seal of the ethylene oxide ampoule was smashed and the mixture was stirred for 10 min. The methanol ampoule break-seal was then smashed and all of the

solvent was removed using a rotary evaporator. The crude product was dissolved in toluene (~5 mL) and precipitated into methanol (~100 mL). The three-arm, star polystyrene was purified by silica gel chromatography using toluene as eluent. The powder was dried in a high vacuum oven overnight before characterization using ^1H NMR, SEC, and MALDI-ToF MS.

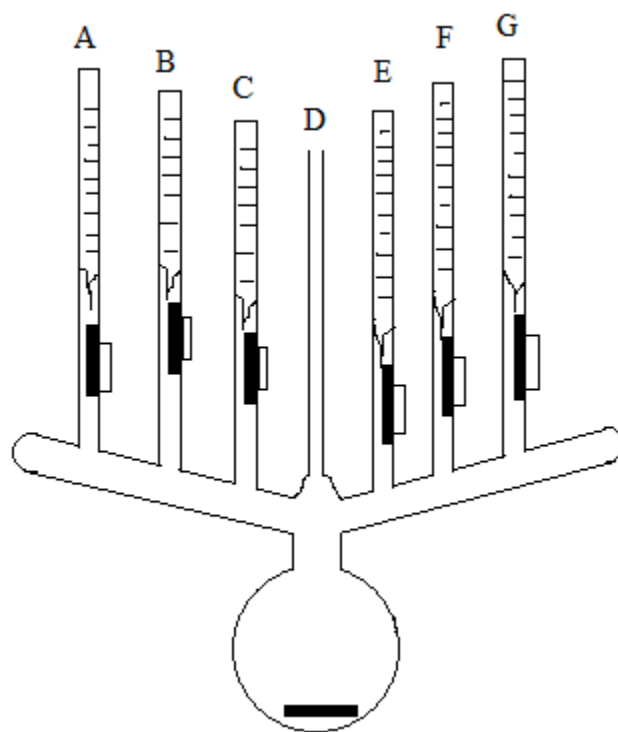


Figure 3.7. Illustration of the reactor used to synthesize the *tris*(α -4-pentenylpolystyryl)methylsilane.

3.3.6 Synthesis of Tadpole-shaped Polystyrene from *tris*(α -4-Pentenylpolystyryl)methylsilane

The reactor used is shown in Figure 3.5. The *tris*(α -4-pentenylpolystyryl)methylsilane (200 mg, 0.1 mmol; $M_n = 2000$ g/mol, A) and *bis*(tricyclohexylphosphine)benzylidineruthenium(IV) chloride (120 mg, 0.14 mmol, C) were each dissolved in dichloromethane (20 mL) and distributed into separate ampoules with stopcocks in the dry box. The ampoules were then taken out of the dry box and connected to the vacuum line (B). Both solutions were degassed using three freeze-pump-thaw cycles in a liquid nitrogen bath and were then removed from the vacuum line by flame-sealing. A 2-L glass reactor equipped with the two ampoules was connected to the vacuum line and dichloromethane (750 mL) was distilled into the reactor by vacuum distillation. The reactor was then removed from the vacuum line by flame-sealing and warmed to room temperature. The break-seals of the *tris*(α -4-pentenylpolystyryl)methylsilane) (three-arm, functionalized star polystyrene), and the Grubbs' 1st generation catalyst, *bis*(tricyclohexylphosphine)benzylidineruthenium(IV) chloride, ampoules were smashed sequentially. The mixture was stirred at 40 °C for 24 h before the reactor was reattached on the vacuum line to transfer most of the solvent back to the storage flask. Then the solution was exposed to air for 10 min. After removing the solvent using a rotary evaporator, the residual catalyst was removed by alumina (neutral, Sigma-Aldrich) column chromatography using toluene as eluent. The product was dissolved in toluene (5 mL), precipitated into methanol (100 mL) and dried in a high

vacuum oven overnight before characterization using ^1H NMR, SEC, and MALDI-ToF MS.

3.4 Synthesis of Four-arm, Star Polystyrene

The reactor used is shown in Figure 3.6. A 150-mL, Morton-creased, glass reactor equipped with a septum-sealed side arm, ampoules of styrene (5 mL, 4.545 g, 44 mmol, A), 1,2-*bis*(dichloromethylsilyl)ethane (41 mg, 0.16 mmol, B), ethylene oxide (1 mL in 5 mL of benzene, 20 mmol, D), and methanol (~2 mL, E) was connected to the vacuum line (C). *sec*-Butyllithium (0.85 mL, 1.25M, 1.069 mmol) was injected into the reactor via the side arm (F) using a gas-tight syringe under a flowing nitrogen atmosphere followed by flame-sealing of the side arm under high vacuum.

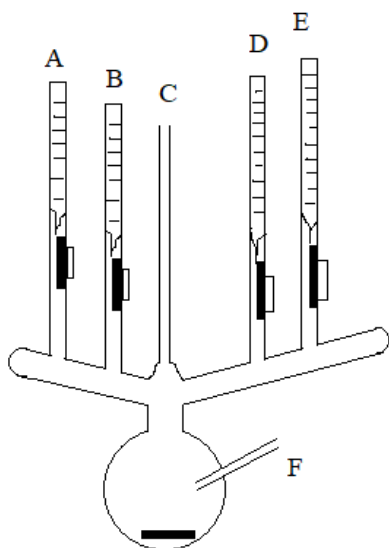


Figure 3.8. Illustration of the reactor used to synthesize the four-arm, star polystyrene.

Benzene (100 mL) was distilled into the reactor cooled with a dry ice/isopropyl alcohol bath before it was removed from the line by flame-sealing. The break-seal of the styrene ampoule was smashed after the reactor was warmed to room temperature. The reactor was stirred for 3 h. An aliquot of the α -*sec*-butylpoly(styryl)lithium (α -PSLi) solution was transferred into an empty ampoule equipped with a methanol ampoule, flame-sealed from the vacuum line, and later quenched using methanol for characterization. The break-seal of the 1,2-*bis*(dichloromethylsilyl)ethane ampoule was smashed and the mixture was stirred at 25 °C for 120 h. Then the break-seal of the ethylene oxide ampoule was smashed and the mixture was stirred for 10 min. The methanol ampoule break-seal was then smashed and all of the solvent was removed using a rotary evaporator. The crude product was dissolved in toluene (~10 mL) and precipitated into methanol (~200 mL). The four-arm star polystyrene was purified by silica gel chromatography using toluene as eluent. The powder was dried in a high vacuum oven overnight before characterization using ¹H NMR, SEC, and MALDI-ToF mass spectrometry.

3.5 Synthesis of Four-arm, Star Polyisoprene

The reactor used is shown in Figure 3.7. A 1-L glass reactor equipped with a septum-sealed side arm, ampoules of isoprene (105 mL, 71.4 g, 1 mol, A), tetrachlorosilane (0.02 mL, 0.16 mmol, B) and methanol (~2 mL, D) was connected to the vacuum line (C). *sec*-Butyllithium (0.6 mL, 1.2M, 0.72 mmol) was injected into the reactor via the side arm (E) using a gas-tight syringe under a flowing nitrogen atmosphere followed by flame-sealing of the side arm under high vacuum. Then cyclohexane (500 mL) was distilled into the reactor cooled with a dry ice/isopropyl alcohol bath before it was removed from the

line by flame-sealing. The break-seal of the isoprene ampoule was smashed after the reactor was warmed to room temperature. The reactor was stirred at 50 °C for 12 h. Then the break-seal of the tetrachlorosilane ampoule was smashed and the mixture was stirred at 50 °C for 72 h. After that, the methanol ampoule break-seal was smashed and all of the solvent was removed using a rotary evaporator. The crude product was dissolved in cyclohexane (~1 L) and precipitated into methanol (~20 L). The four-arm star polyisoprene was dried in a high vacuum oven overnight before characterization using SEC.

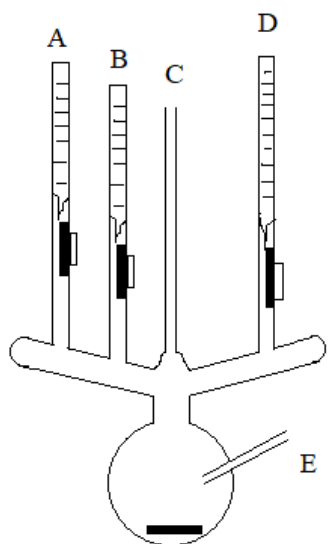


Figure 3.9. Illustration of the reactor used to synthesize the four-arm, star polyisoprene.

3.6 Molecular Characterization

3.6.1 NMR Spectroscopy

^1H NMR characterization was performed using a Varian Mercury 500 instrument (500 MHz) with CDCl_3 (99.8% Cambridge Isotopes) as solvent. Material (5 mg) was

dissolved in 1.5 mL of CDCl₃ and transferred into an NMR tube which was then capped. The relaxation time was set as 30 sec and the spectrum scanned 512 times for each sample.

3.6.2 Size Exclusion Chromatography (SEC)

SEC characterization was carried out on a Tosoh EcoSEC HLC-8320GPC instrument equipped with eight TSK gel columns (30 Å to 10000 Å) and a quad detector system (viscometer, refractive index, light scattering and UV detectors). THF was used as the eluent with a flow rate of 1.0 mL/min at 30 °C. Samples were prepared in THF (5 mg/mL) and filtered through a 0.45 µm Teflon filter before injection. The intrinsic viscosities were obtained using a Viscotek viscometer and the analyses were performed using Wyatt ASTRA software (Version 5.63)

3.6.3 MALDI-ToF Mass Spectrometry

MALDI-ToF MS data were obtained on a Bruker Ultraflex-III MALDI tandem time-of-flight (ToF/ToF) mass spectrometer (Bruker Daltonics, Billerica, MA) equipped with a Nd: YAG laser (355 nm). Samples of 2-[(2E)-3-(4-*tert*-butylphenyl)-2-methylprop-2-enylidene]malononitrile (20 mg/mL) ($\geq 99\%$, Sigma-Aldrich, St. Louis, MO, USA) and silver trifluoroacetate (10 mg/mL) (98%, Sigma-Aldrich, St. Louis, MO, USA) served as matrix and cationizing salt, respectively. Solutions of the matrix (20 mg/mL), cationizing salt (10 mg/mL), and the sample (10 mg/mL) were prepared in THF (Fisher, Fair Lawn, NJ, USA). The matrix/sample/cationizing agent solutions were mixed in the ratio 10:2:1 (vol/vol/vol), and 0.5–1.0 µL of the final mixture were applied to the MALDI sample target and allowed to dry at ambient conditions before spectral acquisition. This sample

preparation protocol led to the formation of $[M + Ag]^+$ ions. Spectral acquisition was carried out in reflectron mode and ion source 1 (IS 1), ion source 2 (IS 2), lens, reflectron 1, and reflectron 2 potentials were set at 25.03 kV, 21.72 kV, 9.65 kV, 26.32, and 13.73 kV, respectively.

3.6.4 Differential Scanning Calorimetry

The glass transition temperatures of the four-arm, star-branched polystyrene and tadpole-shaped polystyrene (obtained by cyclization of the asymmetric, three-arm, star polystyrene) were determined using a TA Instruments Q10 DSC. The scans were performed from 20 °C to 120 °C at the rate of 10 °C /min. The samples were then cooled at the rate of -10 °C/min to 20 °C using liquid nitrogen to eliminate the thermal history, and a second scan was carried out using the same conditions as for the first scan. The data from the second heating scan were collected and analyzed using the Universal Analysis software developed by TA Instruments-Waters LLC.

3.6.5 Rheometry

The bulk viscosities of the four arm star-branched polystyrene and tadpole-shaped polystyrene (obtained by cyclization of the asymmetric, three-arm, star polystyrene) were measured using an Anton Paar MCR rheometer from strain-sweep experiments within the linear viscoelastic region with cone and plate geometry. Shear step strain mode was used with a 25 mm dia., 0.04 rad cone with a 1 mm gap over the temperature range 110 °C to 140 °C and shear rates from 0.0001 to 1000 s⁻¹.

3.7 Molecular Dynamics Simulations

Molecular dynamics simulations were carried out for the star precursor PS and tadpole-shaped PS (TPS). Both simulated chains have molecular weights exactly matching those of their experimental counterparts and were generated initially through the Discover module of Materials Studio 6.0 from Accelrys Inc. Each system consisted of 30 chains of the same molecular weight corresponding to 60 PS monomers. The systems were initially run in the NPT ensemble for 8 ns to determine the equilibrium average volume consistent with the target temperature density. Accordingly, the simulation box size for each system was set to a cubic box of around $71 \text{ \AA} \times 71 \text{ \AA} \times 71 \text{ \AA}$ (with the dimensions changing less than 1 \AA in each direction when the temperature was lowered from 550 K to 510 K) for subsequent runs in the NVT ensemble for at least 10 ns. The systems were modeled with the OPLS-AA force field⁸⁹, which has been shown to capture structural and dynamical properties of PS that are consistent with experimental results⁹⁰. The cutoff radius for the Lennard–Jones term was set to 12 \AA . The particle–particle/particle-mesh Ewald (PPPM) algorithm was used for the calculation of the Coulombic interactions. Both systems were further equilibrated for an additional 2 ns for the chains to diffuse through distances several times their end-to-end distance and data were recorded every 2 ps during this 2ns run for data analysis. Data from the last 1 ns of simulation were used for analysis. All simulations were carried out using the LAMMPS MD package⁹¹ with an integration time step of 1 fs.

3.8 Preparation of Polymer Films

Polymer films of pure material melt for the surface fluctuation studies were prepared by spin-coating the polymer solution onto an etched silicon wafer. The procedures for preparing these samples will be described in the following section.

3.8.1 Preparation of Polymer Films for XPCS

Pure polystyrene (star-branched polystyrene or tadpole shaped polystyrene) was dissolved in toluene (EMD, 99.5%) at a concentration appropriate to achieve a target thickness and the vial containing the solution was rotated for overnight in advance of spin-coating. The silicon substrates were cut out from one-side polished silicon wafers (EL-CAT Inc.) to be 2.0 cm × 1.5 cm size, which had been checked for substrate roughness and polarity using X-ray reflectometer to pick out the qualified wafers. The organic impurities on the surface of the wafers were removed by piranha solution,⁹² and the native oxide layer was removed by immersing the wafer into a 1% aqueous solution of hydrofluoric acid for about 40 seconds, and then rinsing with ultra-purified water and drying with nitrogen gas. The polymer solutions were filtered five times using 0.45 μm filter (Whatman, PTFE) before spin-coating. After this, the wafers were rinsed with 5 mL toluene and then 0.5 mL of the polymer solution was spun-cast onto each wafer at the rotation speed of 2000 rpm for 2 min. The concentrations of the solutions were varied from 1 to 6 wt% based on the target thicknesses of the films. The prepared films were annealed in a high vacuum oven ($\sim 1 \times 10^{-7}$ Pa) at 150 °C for five days for star-branched polystyrene and 95 °C for 12h for tadpole-shaped polystyrene to remove the residual stress and solvent in the films and ensure

that the films were in a state close to the equilibrium at corresponding temperatures before the XPCS measurements.

3.9 Instrument for the Study of Surface Fluctuations

The surface fluctuations of polystyrene melt films were measured using XPCS at the Advanced Photon Source at Argonne National Laboratory. The instrument setup and condition are described in the following section.

3.9.1 X-ray Photon Correlation Spectroscopy

The XPCS measurements were carried out at beam line 8-IDI with partially coherent monochromatic X-ray beam (7.35 keV, $20 \times 20 \mu\text{m}$) with coherence lengths of 7 and 140 μm in the horizontal and vertical directions, respectively. The geometry of the instrument is illustrated schematically in Figure 3.8. The incident angle of X-ray is below 0.14° , which is below the critical angle of polystyrene films (0.16°), and the depth probed in the polystyrene films was restricted to 9 nm. The scattering from the vacuum/surface dominates the scattering pattern. The setup of the instrument enables the collection of intensities at values of the in-plane wave vector, q_{\parallel} , up to 10^{-3} \AA^{-1} . The intensity of the beam was typically 1×10^{10} photons/sec. The XPCS experiments were performed at temperatures 10-60 $^\circ\text{C}$ above the values of $T_{g,bulk}$ of the polystyrenes. The off-specular scattering from the film surface was recorded every certain time intervals using a CCD camera located 3345 mm downstream of the samples.

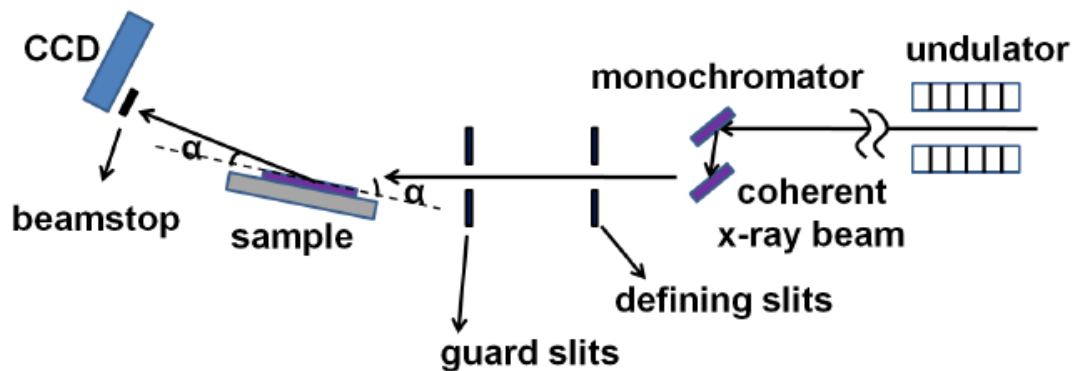


Figure 3.10. Illustration of the XPCS setup at beam line 8-IDI at the Advanced Photon Source. Reproduced with permission.⁴⁵ Copyright 2012, American Chemical Society.

Two dynamic modes were adopted to conduct the XPCS experiment: full frame and kinetic modes. For the full frame mode, the whole area of the CCD camera was used to collect the scattering data as a function of time; while for the kinetic mode, only 1/13 area of the CCD camera is active to capture each frame for the measurement. Examples of scattering patterns recorded on the CCD camera using full frame and kinetic modes are shown in Figure 3.7 (a) and (b), respectively. In either mode, sequences of speckle patterns were collected over time. Generally, the full frame mode is used to measure slow surface fluctuations ($100 \text{ sec} < \tau < 2000 \text{ sec}$) and kinetic mode is used to measure fast surface fluctuations ($0.1 \text{ sec} < \tau < 500 \text{ sec}$). A so called “sleep time”, or the time between adjacent frames with a shutter active, is increased to measure long relaxation time. During the sleep time, there will be no data collection with a fast beam shutter being kept closed to reduce the rate of radiation damage on the spot being measured. The use of sleep time provides

the chance to extend the measurement time to capture long relaxations without further exposure of that sample spot with X-rays. In order to improve statistics while with limited exposure time on each spot, the measurements were done on multiple spots on a sample at the same condition and the correlation functions from these multiple spots were averaged to obtain a correlation function with good statistics. As for kinetic mode, the active area of the detector is divided into 13 regions. The advantage of this mode is that it allows us to measure for shorter times otherwise not accessible due to the readout time of the detector, which is 1.8 sec. As the active area of the detector is divided into several slices and several patterns captured before reading out the detector, the time interval between frames can be reduced to as short as 0.050 sec. By reducing both time per frame and the time between each frame, the extended time window of the XPCS measurement can reach down to relaxation times of order 0.1-1 sec, while with trade-off of narrowing down the $q_{||}$ range probed since a small portion of the CCD camera is used to collect the speckle pattern.

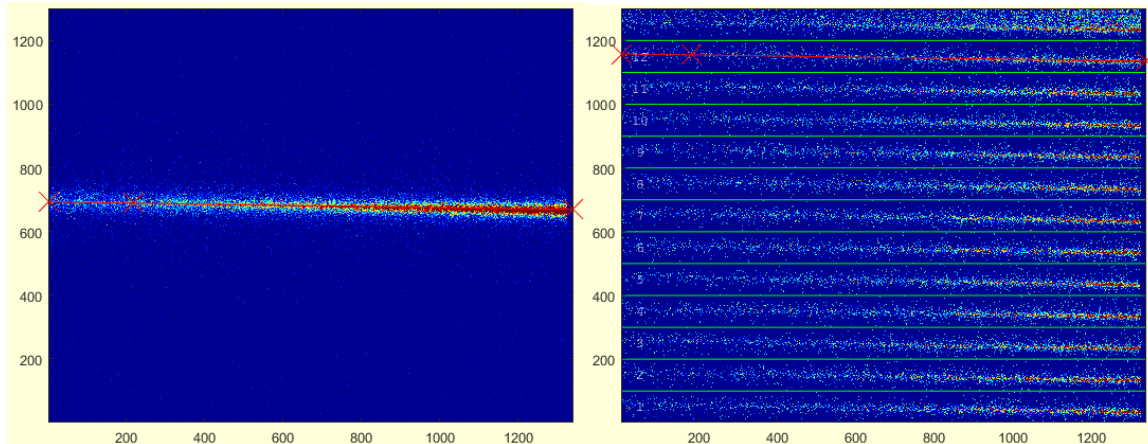


Figure 3.11. CCD images of diffuse scattering collected using (a) full frame and (b) kinetic modes.

Reflectivity measurements were performed before and after the XPCS measurements to obtain the thicknesses of the film and provide a way to check on possible beam damage on the sample. The correlation results using the full number of frames with those using half the number of frames were compared to check the beam damage caused by X-ray exposure at the temperature far above $T_{g, \text{bulk}}$.

Values of autocorrelation function were calculated using a Matlab based analysis program (xpcsgui, version 1060) coded by Zhang Jiang and Michael Sprung of the University of California San Diego and made available to users at 8-IDI by the beamline scientist. The scattering speckles have to be partitioned to define which pixels are associated with certain q_{\parallel} values. Since the number of the static and dynamic partitions are constant for the analysis, use of different mask size leads to the incorporation of different length scales of motion. Therefore, for a given sample under a certain condition, the

relaxation times obtained using different masks can be different, relying on how closely the mask regions match with each other. To keep the consistence of the results entails making just one mask for one mode during the analysis.

CHAPTER IV

SYNTHESES AND CHARACTERIZATION OF TADPOLE-SHAPED POLYSTYRENES

In this chapter, two synthetic routes will be compared and the structures and architectures of the star polystyrene precursors and resulting tadpole-shaped polystyrenes will be verified by characterization data from GPC, NMR and MALDI-ToF MS. The 28.0 Da peak shift in mass spectra after metathesis ring-closure reaction was used to confirm the macrocycle formation.

4-Pentenylithium was used as initiator in styrene polymerization in our previous work.¹²⁻¹³ One can easily prepare star branched polystyrene with multiple α -4-pentenyl functionality at each initiating chain by terminating the α -4-pentenylpoly(styryl)lithium using various silyl halides as linking agent. The use of this initiator ensures that every chain would have this functional group at the initiating, α , chain end.⁹³ Living alkylolithium-initiated polymerization of styrene is one of the most reliable methods for making polystyrenes with controlled, predictable molecular weights and narrow molecular weight distributions.¹⁵

Linking reactions with silyl halides were chosen because of the high efficiency of this reaction of polymeric organolithium compounds, which is not complicated by competing side reactions that are generally observed in linking reactions with organic halides.²⁵⁻²⁶ In order to synthesize a tadpole-shaped polystyrene, a three-arm, star polystyrene precursor was conceived. With the advantage of a metathesis ring-closure

reaction, the easiest way to prepare a tadpole-shaped polystyrene is to first synthesize a *tris*(α -4-pentenylpolystyryl)methylsilane as a precursor, followed by cyclization of two of the three arms to produce a tadpole-shaped polystyrene.

4.1 *tris*(α -4-Pentenylpolystyryl)methylsilane

For polymerization of styrene using 4-pentenyllithium as initiator in benzene, ten equivalents of THF was added to facilitate the dissociation of the primary organolithium aggregates of the initiator. This accelerates the initiation rate to be comparable to the propagation rate to provide polymers with narrow molecular weight distributions.^{15, 94-95} The linking reaction was conducted using trichloromethylsilane to link the resulting α -(4-pentenyl)poly(styryl)lithium chains in benzene. The living chains were prepared in 25% excess to consume all of the trichloromethylsilane.²⁶ The excess living chains were terminated by ethylene oxide and methanol sequentially to form ω -hydroxyethylpolystyrene.⁸⁷ The desired *tris*(α -4-pentenylpolystyryl)methylsilane was separated from the hydroxyl-functionalized polystyrene using silica gel column chromatography with toluene as eluent, based on their polarity difference. This is an alternative to the usual procedure of fractionation to remove unlinked, excess polymer chains after alcohol termination. Quirk and coworkers⁹⁶ have shown that the chromatographic separation for purification of the functionalized precursor is effective for carboxyl-terminated chains of molecular weight up to 56k. For chains with hydroxyl functionality with relatively lower polarity in this work, the chromatographic separation should be applicable to single arm molecular weights up to 20k, or precursor molecular

weights up to 60k. If carboxyl-terminated arms were used here, the reachable molecular weight of the precursor could be potentially higher, perhaps 100k.

The SEC chromatogram of the purified *tris*(α -4-pentenylpolystyryl)methylsilane is shown in Figure 4.1, which shows a symmetric, monomodal distribution. The number average molecular weight, M_n , determined by SEC coupled with a refractometer detector is 2,100 g/mol [$M_n(\text{calc'd}) = 2,000$ g/mol] and the polydispersity index is $M_w/M_n = 1.17$. The larger polydispersity index compared to the that generally obtained by anionic polymerization is probably due to the high concentration of THF, which could have deactivated some of the living chains.

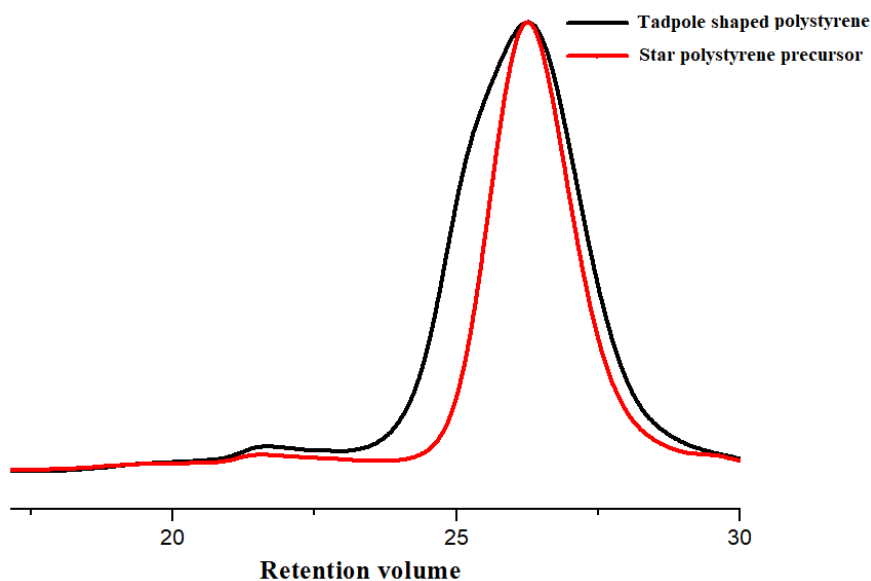


Figure 4.1. SEC chromatograms of purified *tris*(α -4-pentenylpolystyryl)methylsilane (red) and the corresponding tadpole-shaped polystyrene (black).

The ^1H NMR spectrum (Figure 4.2) of *tris*(α -4-pentenylpolystyryl)methylsilane exhibits characteristic vinyl resonances ($-\text{CH}=\$, green) and ($=\text{CH}_2$, red) at δ 6.2 ppm and 5.4 ppm, respectively.¹³ The integration ratio of the two peaks (2.15:1.00), which agrees well with the expected number of protons in the vinyl groups (2:1). The broad peak between δ -0.4 ppm and -0.4 ppm corresponds to the protons of methyl groups which are bonded to silicon [$-\text{SiCH}_3$, blue]. The integration area for this peak relative (0.94) to the two types of vinyl protons (1.00 and 2.15) is consistent with the expected number of protons in the methyl group (1:1:2). These results are consistent with the formation of the star polymer formed with a methyl silyl junction point and three arms with α -4-pentenyl end groups.

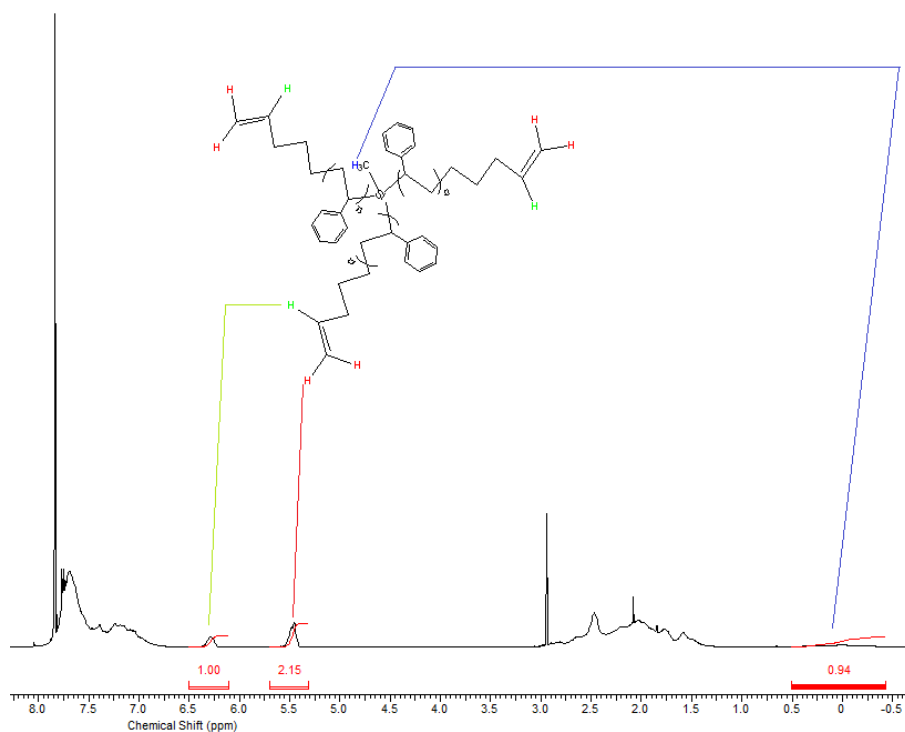


Figure 4.2. ^1H NMR spectrum of *tris*(α -4-pentenylpolystyryl)methylsilane.

The MALDI-ToF mass spectrum of tris(α -4-pentenylpolystyryl)methylsilane is shown in Figure 4.3. A monomodal distribution is present, which demonstrates that the excess linear chains with hydroxyl end groups were completely removed from the product using column chromatography. The calculated monoisotopic mass according to the structure of the 16-mer of tris(α -4-pentenylpolystyryl)methylsilane is 2022.08 Da [3×69.07 (C_5H_9) + 16×104.06 (C_8H_8) + 43 ($SiCH_3$) + 106.91 (Ag^+)], and the observed peak is at m/z 2022.27, which is in excellent agreement with the calculated mass. The MALDI-ToF mass spectrum complemented by the SEC chromatogram confirms the efficient synthesis of tris(α -4-pentenylpolystyryl)methylsilane with controlled molecular weight and quantitative vinyl chain-end functionality for each arm.

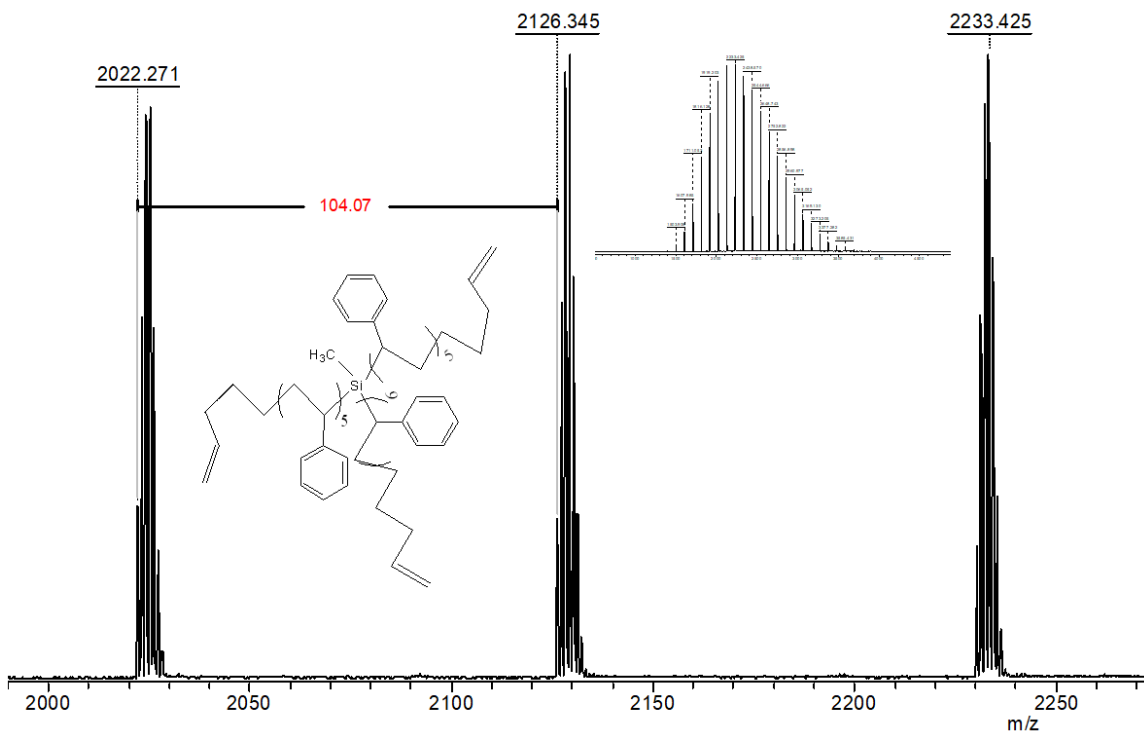


Figure 4.3. MALDI-TOF MS of tris(α -4-pentenylpolystyryl)methylsilane.

4.2 Tadpole-Shaped Polystyrene

Previous work has established that metathesis ring closure using *bis*(tricyclohexylphosphine)benzylidene ruthenium(IV) chloride (Grubb's first generation catalyst at low concentration, 2.6×10^{-4} M) in dichloromethane is an efficient method for cyclization of α , ω -divinyl polymer precursors.¹²⁻¹⁴ Herein we applied this reaction to a trifunctional precursor [*tris*(α -4-pentenylpolystyryl)methylsilane]. The SEC chromatogram of the product after cyclization is shown in Figure 4.1 (black curve), which shows a broadened distribution [M_w (Refractometer) = 3,100 g/mol; $M_w/M_n = 1.38$] and higher molecular weight than that of precursor ($M_n = 2000$ g/mol; $M_w/M_n = 1.17$). This can be ascribed to the higher concentration of the reactive vinyl end groups of the precursor, which could favor the formation of dimer. Also, the product has the residual vinyl group that could participate in dimer formation. Additionally, the solution was not exposed to the air (especially oxygen) for a sufficiently long time (20 mins to air v.s. oxygen bubbling for 20 min) to complete the deactivation of the catalyst, which also could increase the amount of dimer formation.

The formation of the dimer was clearly observed using MALDI-ToF MS. Figure 4.4 shows the full mass spectrum; the numbers for two of the peaks refer to the average values of m/z . The distribution on the left corresponds to the tadpole-shaped polystyrene, while the other distribution on the right represents the dimer generated from intermolecular reactions. The calculated average mass for the 26-mer of the dimer is 3230.87 Da [3×110.20 (C_8H_{14}) + 26×104.15 (C_8H_8) + 2×43.12 ($SiCH_3$) + 107.87 (Ag^+)], which is consistent with the observed peak at 3231.0 m/z . Figure 4.5 shows the monoisotopic peak

for the tadpole-shaped polystyrene in the distribution on the left. The calculated exact mass of the 16-mer of the tadpole-shaped polystyrene is 1994.05 Da [$69.07 (\text{C}_5\text{H}_9)^+$ $110.11 (\text{C}_8\text{H}_{14}) + 16 \times 104.06 (\text{C}_8\text{H}_8) + 43 (\text{SiCH}_3) + 106.91 (\text{Ag}^+)$], which agrees well with the observed m/z at 1994.17. It is interesting to know that the dimer formed from the trivinyl precursor actually contains two macrocyclic rings with an octenyl bridging group. It should be possible to maximize the formation of this interesting dimer by increasing the reaction time and or adding more metathesis ring closure catalyst. Conversely, it may be possible to maximize the formation of the tadpole by diluting the concentration of the trivinyl precursor.

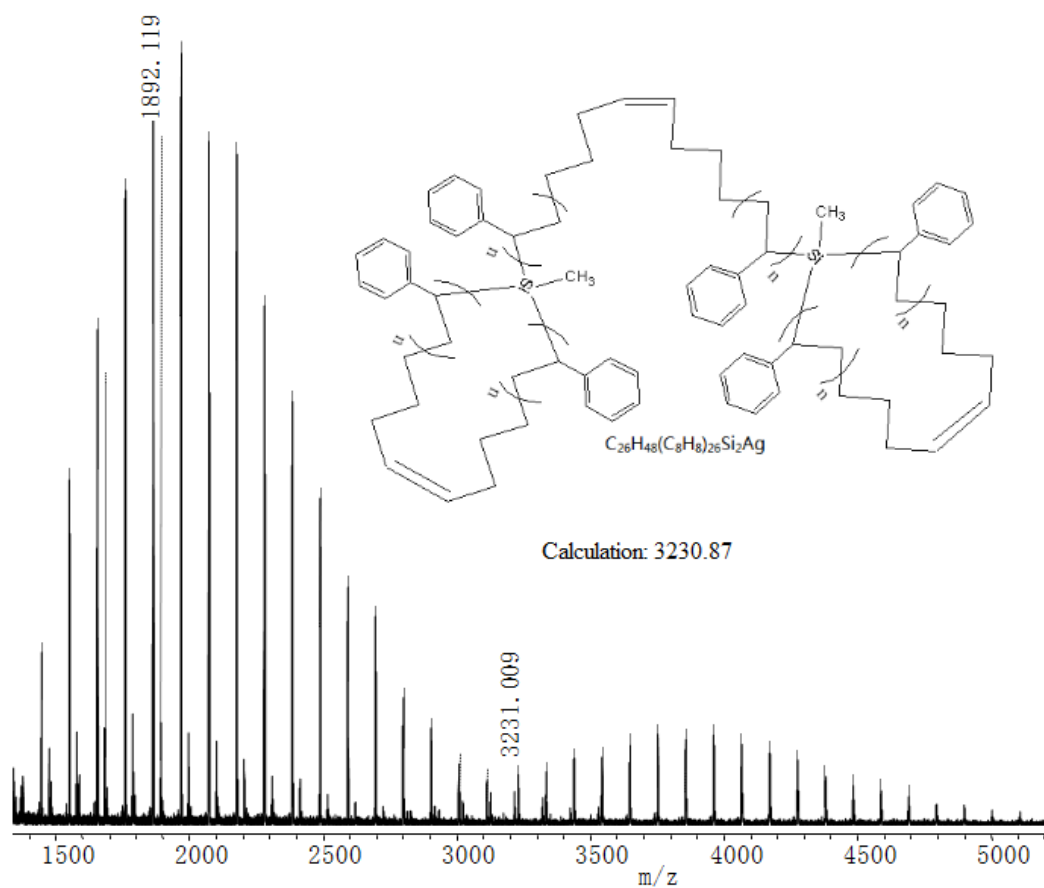


Figure 4.4. Full MALDI-ToF MS of the tadpole-shaped polystyrene and the corresponding dimer formed by cyclization of *tris*(α -4-pentenylpolystyryl)methylsilane using grubbs 1st generation catalyst.

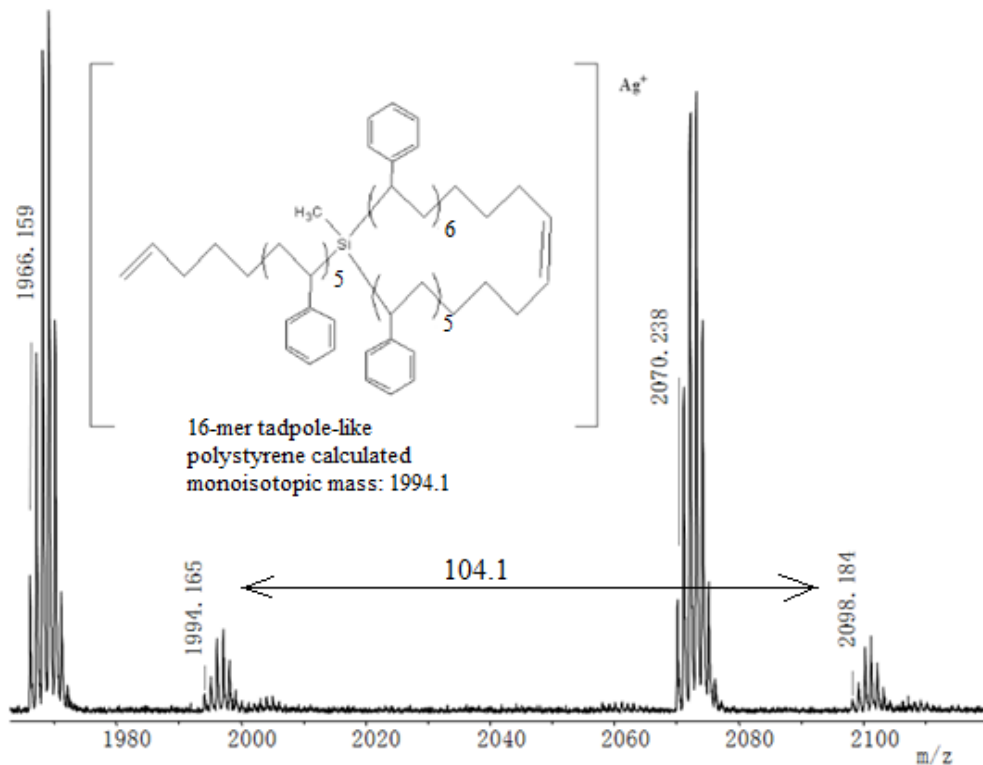
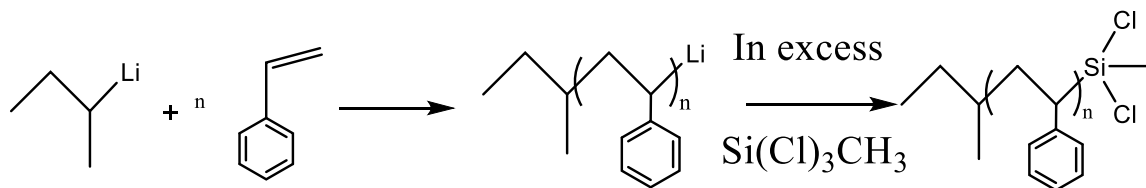


Figure 4.5. Blow up of the lower m/z region for the MALDI-ToF MS of the tadpole-shaped polystyrene and its dimer.

There is another set of peaks at m/z (1966.159 ± 104.06), which is 28 m/z less than the mass of the tadpole-shaped polystyrene. This might be due to the residual catalyst inducing the loss of the ethylene molecule in the tadpole-shaped polystyrene. Apparently, for a physics study purpose, the product is not pure enough to serve as a model to study physics of this molecule. To prevent the intermolecular reaction, an asymmetric three-arm, star polystyrene precursor with only two arms having vinyl groups at the initiating chain end was then synthesized.

4.3 Asymmetric, Three-arm, Star Polystyrene Precursor

To eliminate the reactive third vinyl group in the macrocyclic precursor, an asymmetric, three-arm, star precursor was synthesized. The first step was the preparation of the macromolecular linking agent, ω -methyldichlorosilylpolystyrene, as shown in Scheme 4.1. *sec*-Butyllithium was used as the initiator in benzene to polymerize styrene to generate a saturated, α -*sec*-butylpolystyrene linking agent. An aliquot of this PSLi was quenched with methanol before reaction with methyltrichlorosilane for SEC characterization. The SEC chromatogram of the *sec*-butyllithium-initiated polystyrene is shown in Figure 4.6, which presents a symmetric, monomodal distribution with $M_n = 1800$ g/mol [$M_n(\text{calc}) = 2000$ g/mol], and $M_w/M_n = 1.08$. The concentration of poly(styryl)lithium was 3 wt% to reduce the probability of dimer formation for reaction with methyltrichlorosilane.^{29, 35, 97} Furthermore, an inverse addition of the poly(styryl)lithium solution into a solution of a large excess of methyltrichlorosilane ([Si] : [Li] = 30 : 1) was applied to minimize dimer formation. Three freeze-dry cycles with benzene were performed after the reaction to strip off all excess methyltrichlorosilane.²⁸ The resulting macromolecular linking agent, ω -methyldichlorosilylpolystyrene, was dissolved in benzene, flame-sealed in an ampoule, and then the ampoule was attached to another reactor to prepare the asymmetric, three-arm, star precursor.



Scheme 4.1. Synthesis of ω -methyldichlorosilylpolystyrene using anionic polymerization.

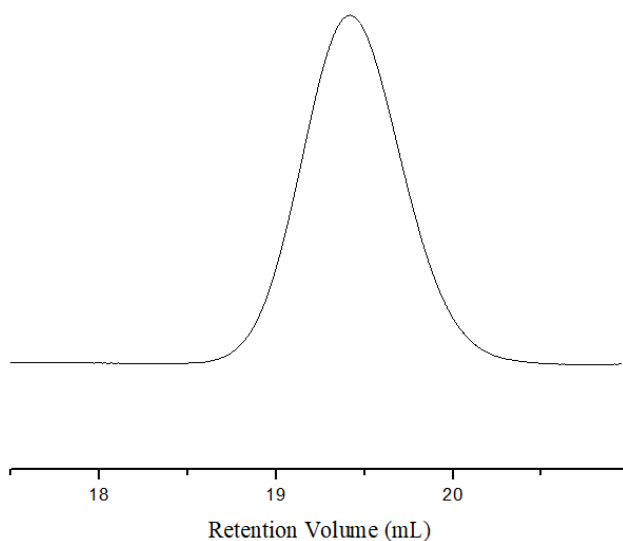


Figure 4.6. SEC chromatogram of the base polymer from *sec*-butyllithium-initiated polystyrene.

In next step, 4-pentenylithium was used as initiator for polymerization of styrene in benzene (Scheme 4.2). Since too much THF might lead to chain termination,¹⁵ only five equivalents of THF were added to the reaction to favor the dissociation of the aggregates of this primary organolithium initiator. Addition of THF increases the rate of initiation relative to propagation to generate a narrower molecular weight distribution. The presence of a Lewis base, such as THF, also facilitates the rate of chlorosilane linking reaction.¹²⁻¹⁴

The concentration of THF used here was decreased by 50% compared to previous work.¹²⁻
¹⁴ The base polymer was obtained by quenching an aliquot of the α -4-pentenylpoly(styryl)lithium by methanol for SEC characterization, while the rest of the PSLi was reacted with the macromolecular linking agent, ω -methyldichlorosilylpolystyrene, synthesized in the first step. The SEC chromatogram of the α -4-pentenylpolystyrene (Figure 4.7) shows a symmetric, monomodal distribution with $M_n = 1800$ g/mol [$M_n(\text{calc}) = 2000$ g/mol] and $M_w/M_n = 1.09$.

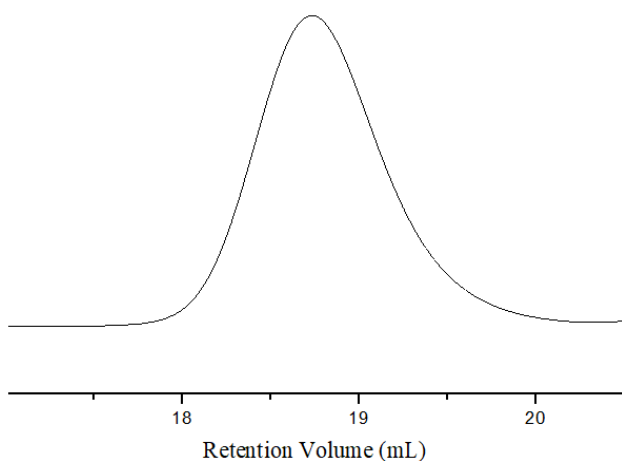
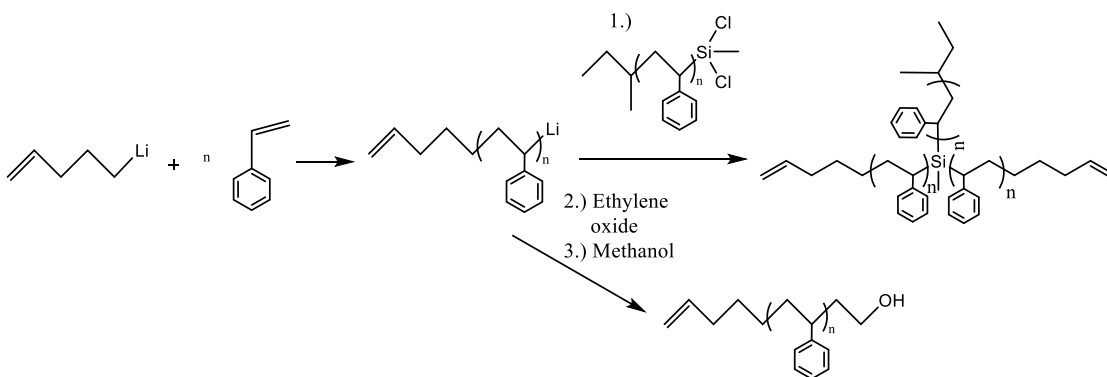


Figure 4.7. SEC chromatogram of α -4-pentenylpolystyrene.



Scheme 4.2. Synthesis of asymmetric, three-arm, star precursor.

The PSLi living chains were in 57% excess relative to silyl chloride groups in the macromolecular linking agent to drive the reaction to completion. The linking process was allowed to proceed for 24 h, followed by addition of ethylene oxide to functionalize the excess PSLi chains with hydroxyl groups, (Scheme 4.2) which could be readily removed from the desired product by silica gel column chromatography.

The SEC chromatogram of the asymmetric, three-arm, star precursor exhibited a symmetric, monomodal distribution, with $M_n = 5500$ g/mol [$M_n(\text{calc}) = 5600$ g/mol] and $M_w/M_n = 1.09$, as shown in Figure 4.8. The slightly larger elution volume for the tadpole compared to that of the star precursor indicates that the tadpole is slightly more compact than the star, as seen also by Tezuka et al.⁶. Since the apparent difference in hydrodynamic volumes between the tadpole polymer and its star precursor is smaller than the difference in hydrodynamic volumes between cyclic polymers and their linear analogs,^{12-13, 98-99} it was of interest to investigate the intrinsic viscosity change after the cyclization. The ratio of the intrinsic viscosity of purified, tadpole-shaped polymer to that of the star precursor ($[\eta]_v/[\eta]_s$) was 0.88, which is larger than that of macrocyclic polymer to linear precursor (0.58-0.68) reported in the literature.^{98, 100} This is expected based on the larger difference in compactness between cyclic and linear than between tadpole and cyclic, in fact, 30% of the tadpole is linear polymer segment.

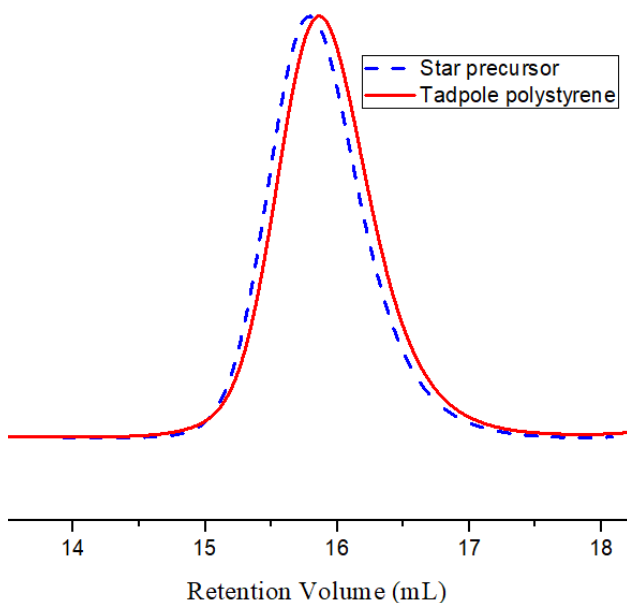


Figure 4.8. SEC chromatograms of (a) purified asymmetric, three-arm, star precursor (blue, dashed curve) and (b) corresponding macrocyclic polystyrene (red, solid curve).

Since no MD simulations of the difference in hydrodynamic size of star and tadpole analogs have been previously published, such simulations have been done here for comparison with the experimental results. Shown in Figure 4.9 are the probability distribution functions for the hydrodynamic radii (R_H) for the star and tadpole PS as simulated for the pure melt at 510K. (Additional plots for R_g and for the temperature of 550K are shown in Figures S5-S7). The calculated ensemble average value $\langle R_H \rangle$ for the tadpole is seen to be about 4% smaller than that of the star, so the hydrodynamic volume would be expected to be about 12% smaller. The hydrodynamic volumes (V_H) corresponding to the peak positions in Figure 4.8 were calculated in the following way. The molecular weights of the linear chains corresponding to the two peak positions were found from the calibration curve created with linear PS standards. Then the infinite dilution diffusion coefficient corresponding to those molecular weights interpolated from

experimental light scattering data for PS in THF at 25 °C from Kok and Rudin¹⁰¹. From these the hydrodynamic radii and thus the values of V_H corresponding to these peak positions were calculated. From the GPC data V_H of the star chain is 11% larger than that for the tadpole. The results from the MD simulations thus agree very well with the experimental results showing the small reduction in hydrodynamic volume that comes with the cyclization of the three-arm star to make the tadpole-shaped chain.

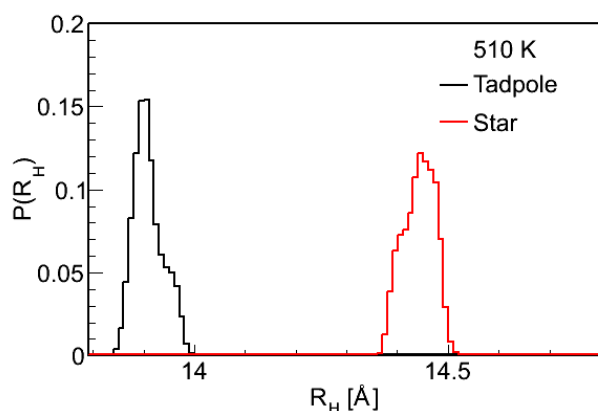


Figure 4.9. Probability distribution functions for hydrodynamic radii of the star and tadpole PS simulated using molecular dynamics of the pure melts at 510K after 1000 steps.

The ^1H NMR spectrum (Figure 4.9) of the asymmetric, three-arm, star precursor exhibits characteristic vinyl resonances at δ 5.7 ppm ($-\text{CH}=\text{}$, H_a) and 4.9 ppm ($=\text{CH}_2$, H_b), respectively.¹²⁻¹⁴ The integration ratio of 1.00: 2.09 is consistent with the incorporation of vinyl groups in the three-arm star precursor. The multiplet between δ 0.5 ppm and 0.8 ppm corresponds to the protons of the *sec*-butyl methyl groups from the initiator ($-\text{CH}_3$, H_c). The integration ratio of this peak (6 H) relative to that of the vinyl protons (6 H) is 3.24: 3.09, which confirms the proposed structure of the asymmetric, three-arm, star precursor.

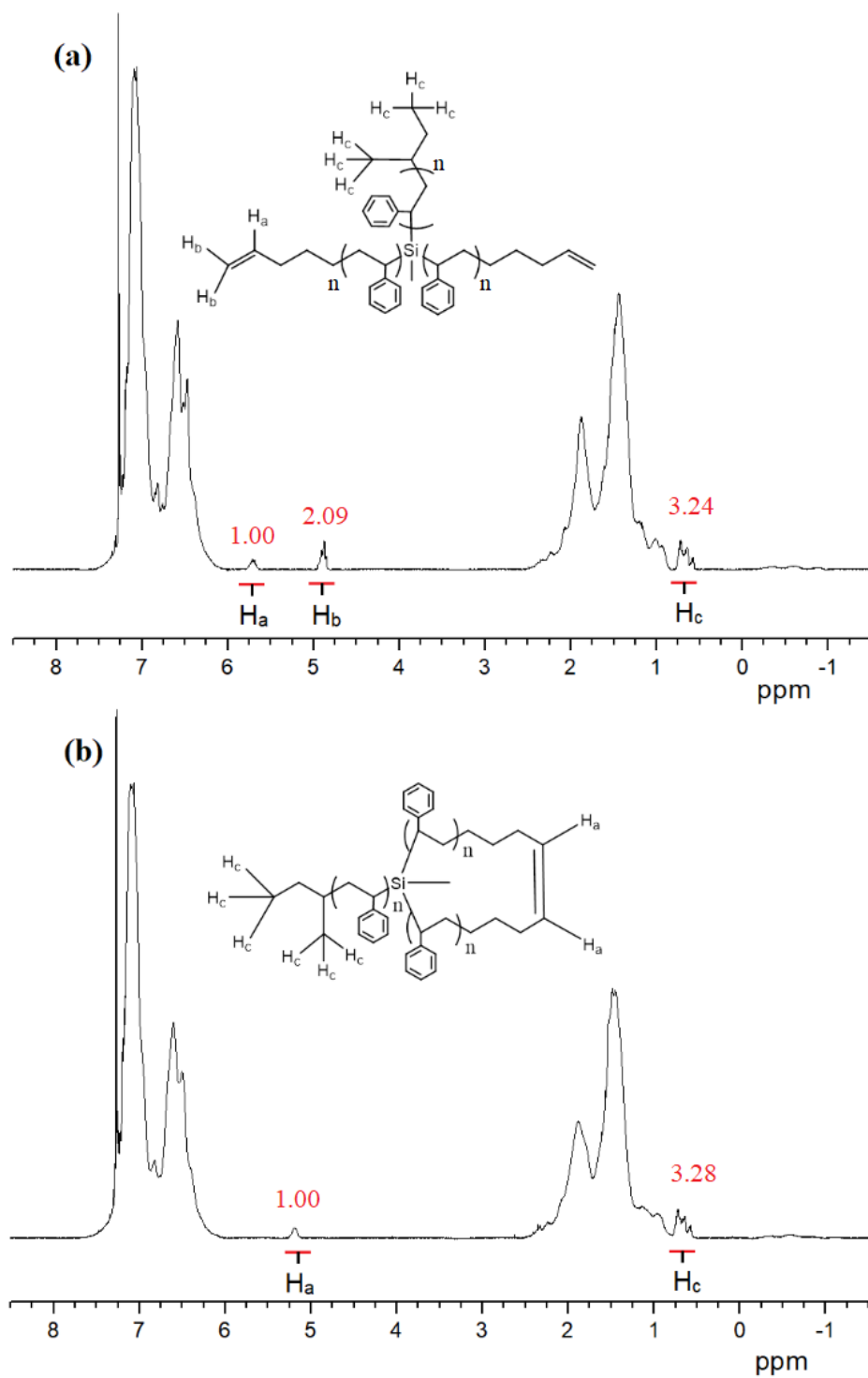


Figure 4.10. ^1H NMR spectra for (a) asymmetric, three-arm, star precursor and (b) the tadpole-shaped polystyrene.

The MALDI ToF MS spectrum of the purified asymmetric, three-arm, star polystyrene, as shown in Figure 4.10, shows a clean, monomodal distribution, which proves that the excess linear chains with hydroxyl groups were completely removed by silica gel column chromatography. This simple purification procedure is a vast improvement compared to the fractionation method of generally used to remove excess arm polymers for star polymer syntheses. The calculated monoisotopic mass based on the structure of the silver adducted 54-mer of the asymmetric, three-arm, star polystyrene is 5964.58 Da $[(C_{447}H_{462}Si + Ag)^+ : 57.07 (C_4H_9) + 2 \times 69.07 (C_5H_9) + 43 (Si-CH_3) + 54 \times 104.064 (C_8H_8) + 106.91 (Ag^+)]$, which agrees well with the experimentally observed m/z value at 5964.64. The mass difference between neighboring oligomers is measured to be 104.07 Da, corresponding to the mass of a styrene unit. Therefore, it can be concluded that SEC, 1H NMR and MALDI-ToF MS characterizations consistently verify the structure of the asymmetric, three-arm, star polystyrene with controlled molecular weight and narrow molecular weight distribution.

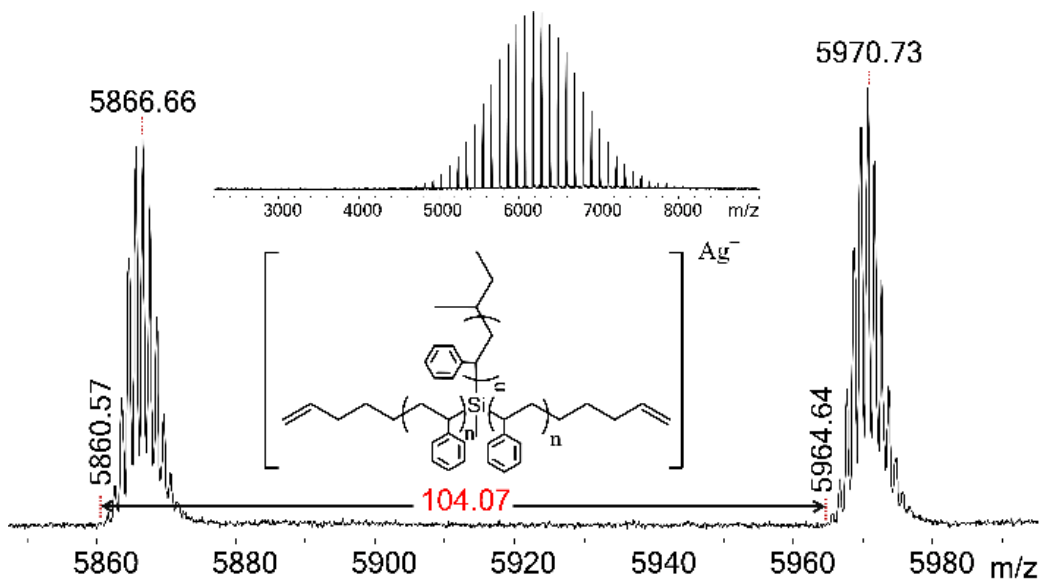


Figure 4.11. MALDI-MS spectrum of asymmetric, three-arm, star precursor.

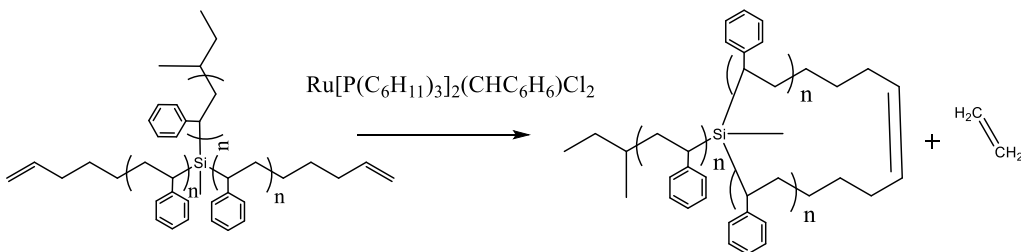
4.4 Tadpole-Shaped Polystyrene

The macrocyclization of telechelic, α , ω -divinyl polystyrenes using a metathesis catalyst has been shown to be very efficient; therefore, it was anticipated that this reaction would be useful to synthesize a tadpole-shaped polymer using the asymmetric three arm star precursor.^{12-14, 31, 102} High dilution conditions were utilized to eliminate dimer formation from intermolecular chain extension based on previous work.¹²⁻¹⁴ The asymmetric, three-arm, star precursor was dissolved in methylene chloride with *bis*(tricyclohexylphosphine)benzylidene ruthenium(IV) chloride (Grubb's 1st generation catalyst), and heated at 40 °C for 40h (Scheme 4.3). The solution was bubbled with oxygen for 20 min after the reaction to deactivate the catalyst, which then was readily removed by alumina column chromatography using toluene as eluent. The SEC chromatogram of the cyclization product, as shown in Figure 4.9(b), showed a symmetric, monomodal peak with

$M_n = 5500$ g/mol and $M_w/M_n = 1.09$ ($M_p = 5100$ g/mol). The peak was shifted to the right after cyclization (M_p of tadpole being smaller than M_p of the precursor); this is consistent with the smaller hydrodynamic volumes of macrocycles compared with their linear precursors.^{12-14, 98-99} The ^1H NMR spectrum of the cyclization product (Figure 4.9b) shows that the vinyl resonances at δ 4.9 ppm ($-\text{CH}=\text{}$, H_a) and δ 5.7 ppm ($=\text{CH}_2$, H_c) of the precursor have disappeared, while a new, internal, vinyl proton resonance at δ 5.1 ppm ($-\text{CH}=\text{CH}-$, H_a) is observed.¹²⁻¹⁴ This is consistent with the proposed structure of the tadpole-shaped polystyrene. The integration ratio of the multiplet between δ 0.5 ppm to 0.8 ppm corresponding to the *sec*-butyl methyl group protons (6 H) to the peak at δ 5.1 ppm representing vinyl protons (2 H) is 3.28:1, which is in good agreement with the expected structure (Figure 4.9b). These H NMR results have been reported previously for metathesis cyclization of α , ω -divinylpolystyrenes to form the corresponding macrocycles.¹²⁻¹⁴

MALDI-ToF MS has proven to be the most definitive and quantitative tool to characterize and confirm the macrocyclic structure for the metathesis ring closure method.¹²⁻¹⁴ The loss of an ethylene molecule after cyclization provides a definitive method to distinguish the precursor and cyclization product in the mass spectrum and to determine the efficiency of the conversion to the macrocycle (as shown in Scheme 4.3). In contrast, many other methods for forming macrocycles yield products with the same molar mass as that of the precursor. The mass spectrum of the tadpole-shaped polystyrene, as shown in Figure 4.11, exhibits a clean monomodal distribution. The absence of both higher and lower molecular weight impurities attests to the efficiency of this synthetic method. The calculated monoisotopic mass based on the structure of the silver adducted 54-mer,

tadpole-shaped polystyrene is 5936.55 Da $[(C_{445}H_{458}Si + Ag)^+ : 57.07 (C_4H_9) + 110.11 (C_8H_{14}) + 43 (Si-CH_3) + 54 \times 104.064 (C_8H_8) + 106.91 (Ag^+)]$, which is in excellent agreement with the experimentally observed value at m/z of 5936.42.



Scheme 4.3. Synthesis of tadpole-shaped polystyrene.

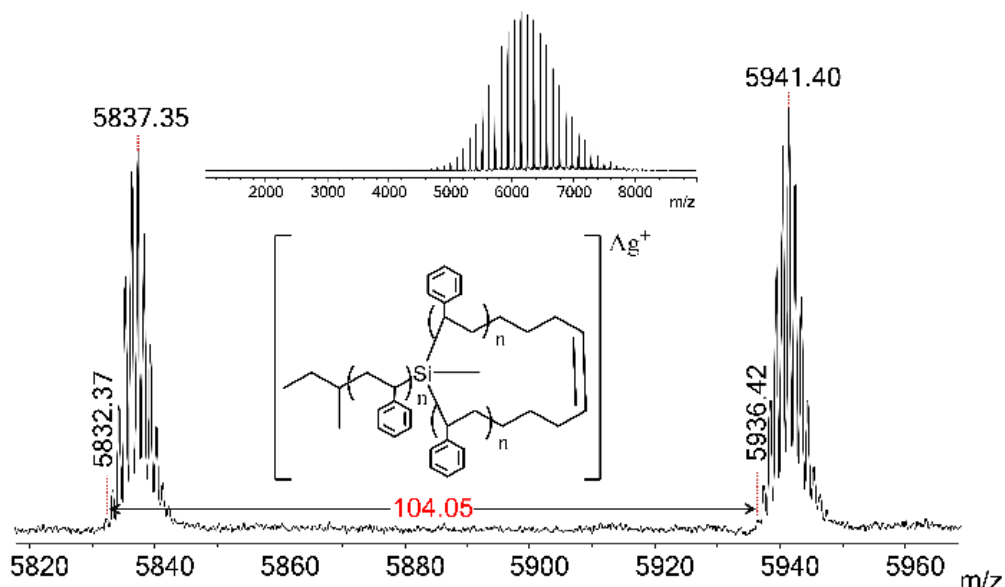


Figure 4.12. MALDI-ToF MS spectrum for the tadpole-shaped polystyrene.

The mass difference between a given monoisotopic peak for the tadpole-shaped polystyrene and the corresponding peak for the three-arm precursor with the same number of styrene units should be m/z 28.0 due to the loss of an ethylene molecule (C_2H_4) after cyclization. This allows us to distinguish the two products in the mass spectra as shown in Figure 4.13. Indeed, the monoisotopic peak for the 48-mer, tadpole-shaped polystyrene is

observed at m/z 5311.94, while the corresponding monoisotopic peak for the 48-mer star precursor is observed at m/z 5340.72, giving a mass difference of m/z 28.78, which is consistent with the anticipated value for loss of an ethylene molecule after cyclization. Thus, the MALDI-ToF MS results agree well with SEC and ^1H NMR results, all of which demonstrate the efficiency of this ring closure reaction to produce a well-defined, tadpole-shaped polystyrene with single atom junction point (Si), predictable molecular weight and narrow molecular weight distribution.

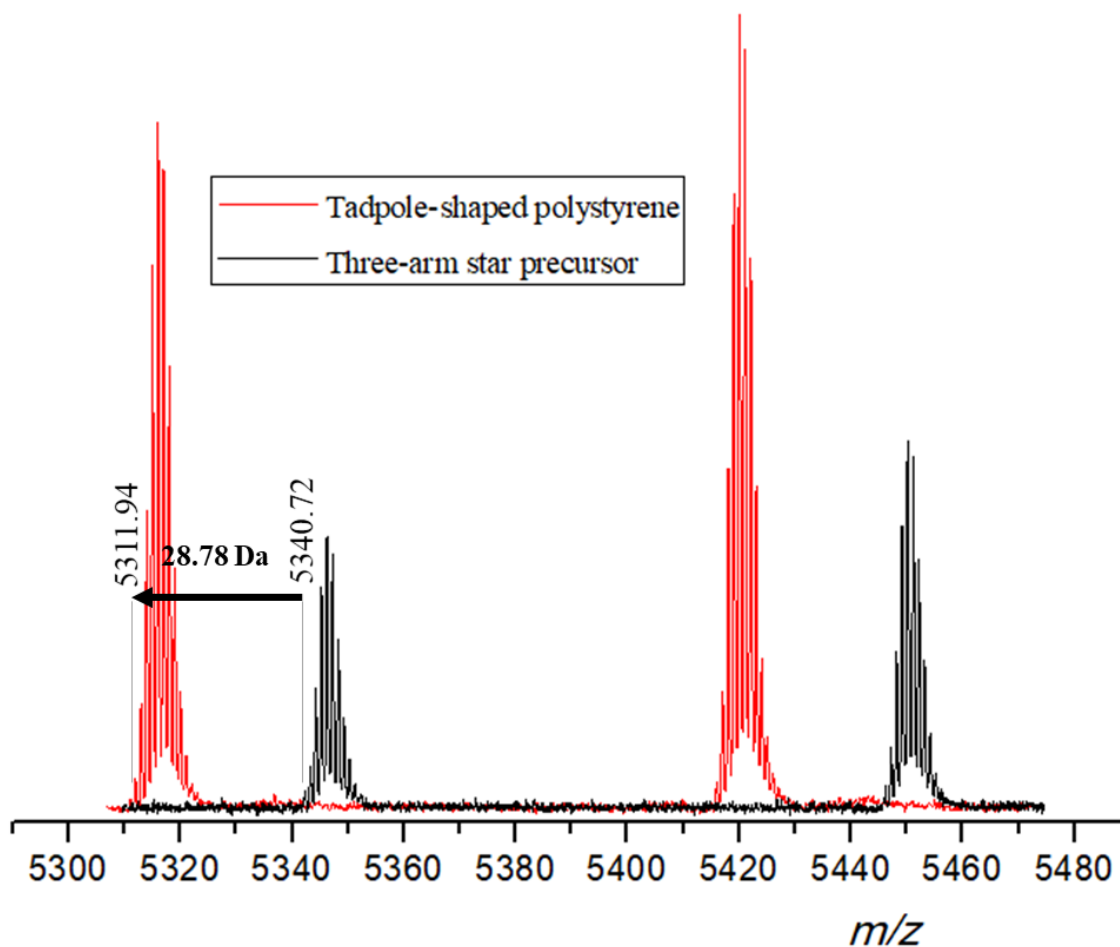


Figure 4.13. Overlaid mass spectra for the asymmetric, three-arm, star precursor and tadpole-shaped polystyrene.





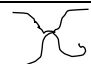
This synthetic methodology should work also for higher molecular weight tadpole molecules. Wang has explored the synthesis of macrocyclic polystyrenes with M of up to 36k¹³. That value is likely the attainable upper limit of molecular weight for the cyclic part of the molecule. As for the tail, which serves as a linking agent in our synthetic strategy, according to previous work by Fetters and Pennisi²⁸, the upper limit can be up to 100k. This is dictated by the requirement that the functionalized end of the linking agent be able to “find” and react with the two arms to form the asymmetric 3-arm star precursor. The overall attainable M for the tadpole PS, based on this synthetic method, is therefore around 130k.

4.5 Physical Properties of 6k Tadpole-Shaped Polystyrene

Table 4.1 compares the values of T_g determined by DSC for the three polymers in this study as well a 6k cyclic and 4-arm star analogs studied by He et al.³⁹ The T_g of the linear 6k PS (synthesized by anionic polymerization) was measured to be 85.3 ± 0.3 °C, and the T_g s of the 6k tadpole-shaped polystyrene and its three-arm star precursor synthesized here were determined to be 88.0 ± 0.4 and 76.3 ± 0.4 °C, respectively (Figure 4.13a). The effects of changes in the architecture of the chains on T_g are apparent. As the number of chain ends decrease, and with it the free volume, the T_g increases. The larger number of chain ends in the star PS than in the linear PS introduces additional free volume, which markedly lowers T_g by 9 °C. After cyclization of the three-arm star polystyrene, the number of chain ends drops by 66%, and the T_g increases by 12 °C due to a reduction of free volume and becomes larger than that of the linear chain. The cyclic analog to the 6k linear PS chain of He et al.³⁹ had a T_g of 98.9 °C. We had anticipated that the T_g of the

tadpole would be between the T_g s of the cyclic chain and linear chain of same overall molecular weight, and indeed that is what we see. In addition, the MD simulations show that at both 510 and 530 K the tadpole density is 1% higher than the star precursor density, consistent with the higher T_g for the tadpole. The ordering of the T_g s we see is also in line with the results of Monteiro and coworkers,⁴¹ who found that the T_g of their TPS was between the T_g s of their LPS analog and the interpolated value of T_g for a cyclic analog, all having overall molecular weights of 12k. However, in their case the T_g of the tadpole was closer to that for the cyclic than to that for the linear.

Table 4.1. T_g s for 6k polystyrenes with various architectures

Molecular weight (g/mol) ^a	Architecture	Schematic	T_g (°C)
6000	Cyclic		98.9 ^b
5500	Tadpole		88.0 ^c
6000	Linear		85.3 ^c
5500	3-arm star		76.3 ^c
6000	4-arm star		77 ^b

a. Measured using GPC with THF as eluent, uncertainty $\pm 10\%$

b. Measured using TA Q200 DSC, heating and cooling rate of 10K/min

c. Measured using Perkin-Elmer Pyris DSC, heating and cooling rate of 10K/min

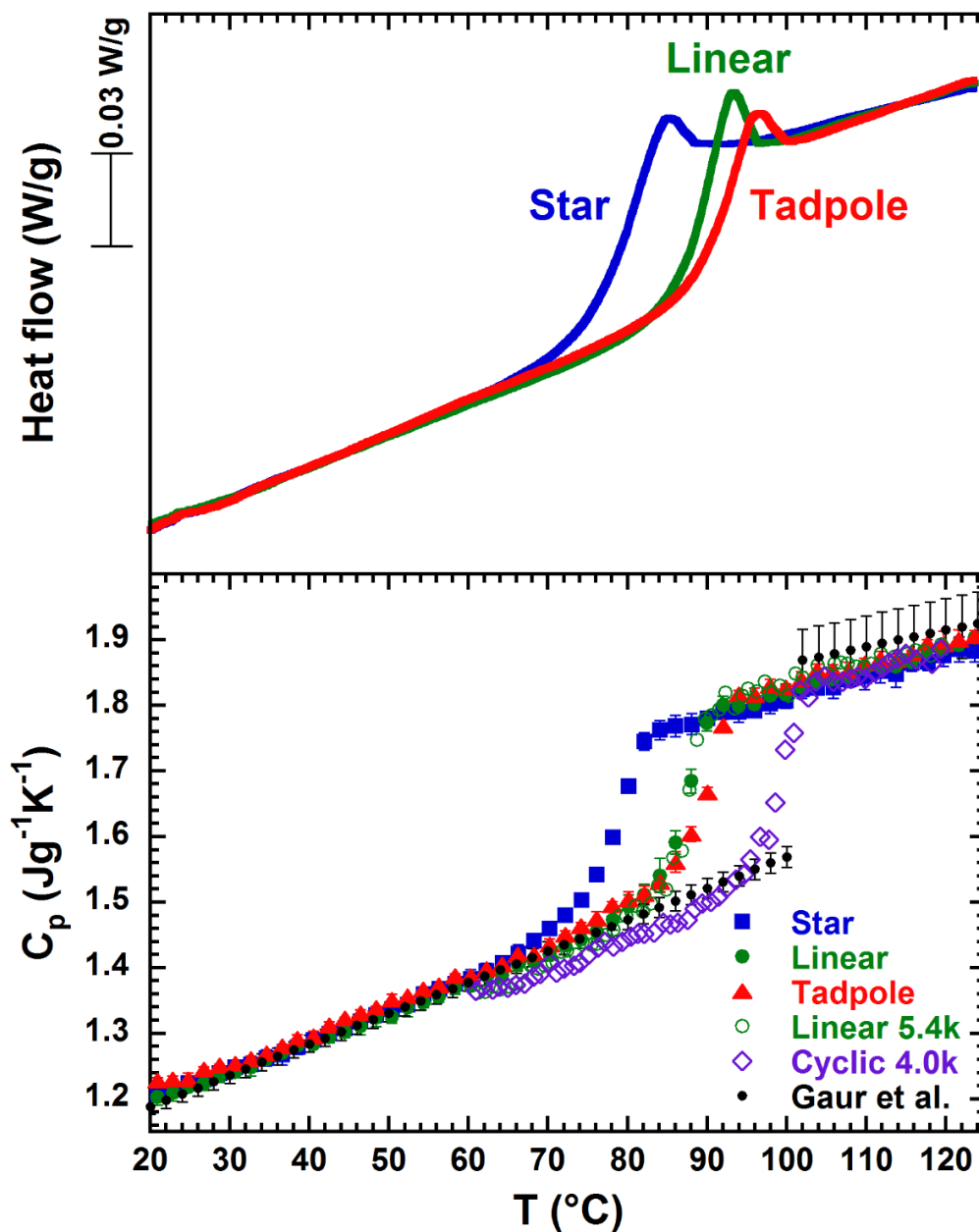


Figure 4. 14. a) Top panel: DSC scans for the three-arm star precursor, tadpole, and linear analogue, performed on heating at 10 K/min after cooling at 10 K/min. b) Bottom panel: Absolute heat capacity for the three samples, along with results for a linear and cyclic polystyrene from Huang et al.¹⁰³ and a compilation of results from the literature from Gaur and Wunderlich.¹⁰⁴

A quantitative comparison of the T_g s from our work and those for similar structures reported in the literature is shown in Figure 4.14, where T_g is plotted as a function of the concentration of chain ends. A linear relationship, as suggested by Fox and Flory,¹⁰⁵ is expected if the free volume arising from chain ends is the dominant factor determining T_g . We note that although Uberreitter and Kanig¹⁴ found a slightly better relationship with reciprocal T_g for small molecular weights, we plot the simpler relationship here for the purpose of clarity and because the difference in predictions from the two equations averages only 0.1 K in the regime we are interested in. The linear chains all follow the Fox and Flory linear relationship, with T_g decreasing with increasing free end concentration or decreasing molecular weight. In addition, our stars and tadpole also follow the same relationship, independent of structure, indicating that our junctions have no significant effect on T_g . Similarly, a cyclic material previously studied¹⁰³ follows the same trend, as does a short four-arm star investigated by Archer and coworkers¹⁰⁶ and the linear chain from the study of Monteiro et al.¹² that does not contain a triazole junction. On the other hand, Monteiro's tadpoles, bicycles, and tricycles that contain triazole junctions have higher T_g s due to the constraints imposed by the junctions; this has been elegantly pointed out in their most recent work, with T_g shown to increase linearly with the number of constrained segments for structures with no chain ends.¹⁵ Interestingly, two of the structures shown in Figure 4.14 (a linear chain and a three-arm star containing triazole junctions) also seem to follow the Fox and Flory relationship. Whether this is serendipitous or due to chain ends dominating in these materials is unclear. With the single atom junction used here, the explanation is more straightforward.

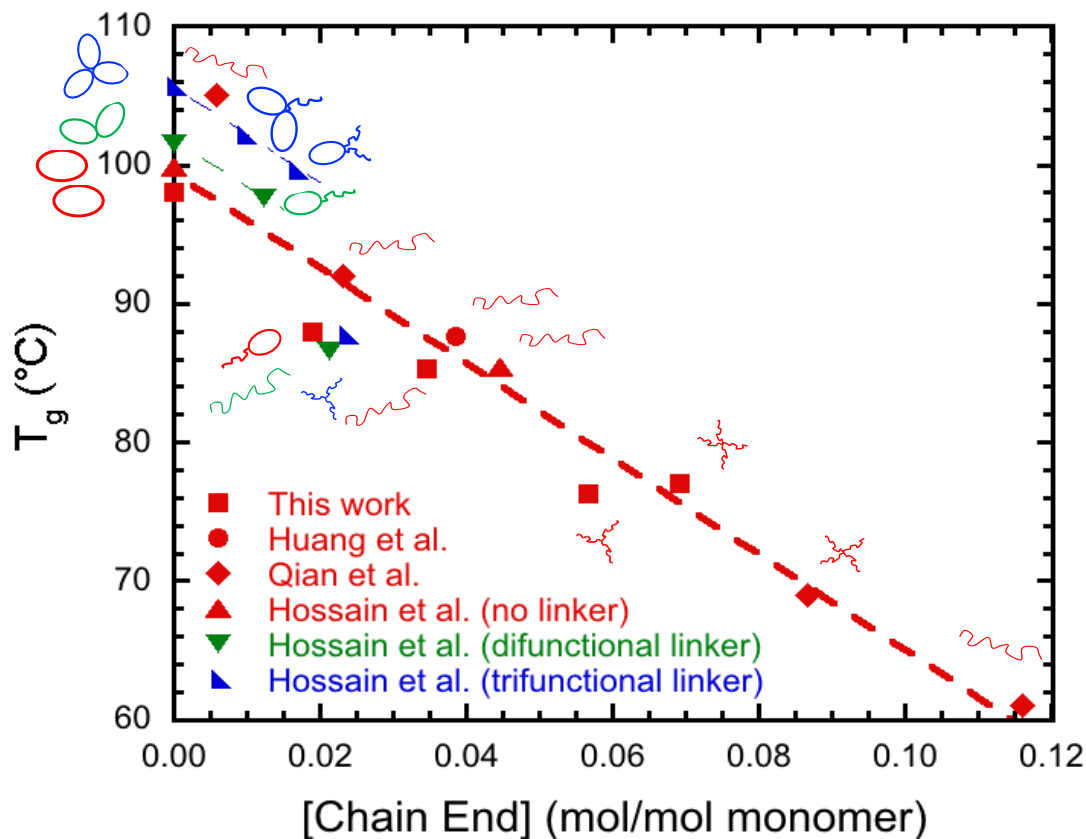


Figure 4.15. Summary of the variation of T_g with density of chain ends for the molecules considered in this work, set in the context of variations seen in other studies. To understand the T_g behavior for the star precursor and tadpole studied here, it is sufficient to consider the density of chain ends, whereas for some molecules from Monteiro et al.⁴¹ with bulkier and stiffer junction points it is necessary to consider the junction point types as well.

Additional insight from the thermal analysis is offered by consideration of the absolute heat capacity measurement, the results of which are shown in Figure 5b for the tadpole, its three-arm precursor, and the linear counterpart, along with results from a low-molecular weight cyclic and linear polystyrene previously studied, and a compilation of literature data from Gaur and Wunderlich.⁵⁵ In spite of the differences among the T_g s of the

various materials, the absolute heat capacities are identical within the error of the measurements ($\pm 1\%$) and the same as for high molecular weight PS. The result suggests the junctions in our molecules are not significantly impacting the pure material thermodynamics.

CHAPTER V

VISCOSITY ENHANCEMENT IN SUPPORTED MOLTEN STAR POLYSTYRENE FILMS

In this chapter, the effect of chain ends and branching point on the surface fluctuations of the polymer films will be presented. Surface fluctuations of a series of 15k SPS films with different thicknesses ($10 - 100R_g$) were systematically measured using XPCS. Viscosities derived from the XPCS data using the overdamped capillary wave theory were compared with values obtained from bulk rheology and a two-layer model with a highly viscous layer next to the substrate was generated to rationalize the data.

Star polystyrenes with narrow molecular weight distributions were synthesized using anionic polymerization and silicon linking reaction. Characterizations using SEC and MALDI-ToF MS verified the structure of the 15k four-arm star polystyrene. T_g of this 15k star polystyrene was measured with DSC to be 88 °C.

Surface tension and experimentally measured bulk viscosity for 15k SPS at different temperatures are listed in Table 5.1. Surface tension was calculated by extrapolation of data for 6.3, 12.6, and 18k SPS.¹⁰⁷

Table 5.2. Surface Tension and Bulk Viscosity of 15k Four-arm Star Polystyrene

temperature (°C)	γ_{linear}^a (mN/m)	η_{bulk} (Pa s) ^a
120	33.75	68000
130	32.8	8500
140	31.8	1400

^aUncertainty $\pm 5\%$.

With viscosity data in hand it was possible to estimate the amount of annealing that would have been expected to result in equilibrium behavior for a bulk samples. Based on the Rouse Model, the relaxation time, τ_R , is given by:

$$\tau_R \approx \frac{\eta_s b^3}{kT} N^2, \quad (5.1)$$

where η_s is the solvent viscosity at the annealing temperature (300 Pa S), b is the size of a Kuhn segment (7×10^{-10} m), k is the Boltzman constant ($k = 1.38 \times 10^{-23}$ J/K), T is the temperature (423K) and N is the number of Kuhn segments (145). The bulk Rouse relaxation time is estimated to be 0.4s and we annealed the films at 423K for 120 hours (432000s). Usually, the annealing time being two or three times larger than relaxation time is considered to be sufficient for the chains to reach equilibrium. Here, the annealing time is 6 orders of magnitude larger than the relaxation time. Therefore, we considered the films to be fully equilibrated. Non-equilibrium behavior shouldn't be a factor when we consider the XPCS results for this star film.

Plots of τ/h for the two thickest films (112 nm and 277 nm) collapse onto a universal curve for each temperature, as shown in Figure 5.1. The viscosities derived from fits to the curve for each temperature, η_{XPCS} , agree (within 20%) with those from bulk rheology, η_{bulk} (Figure 5.2). No viscosity enhancement is evident at these thicknesses.

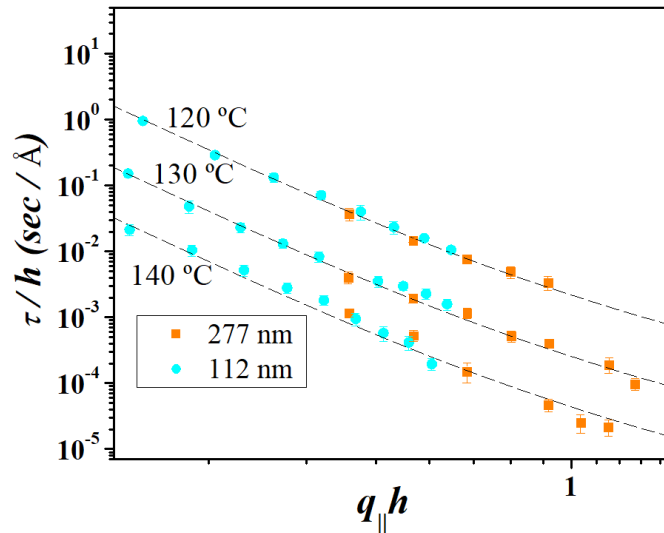


Figure 5.1. τ/h vs $q_{||}h$ at three temperatures for SPS films of two thickness. The dashed curves correspond to least-square fits using the HCT expression with η_{XPCS} as a fitting parameter.

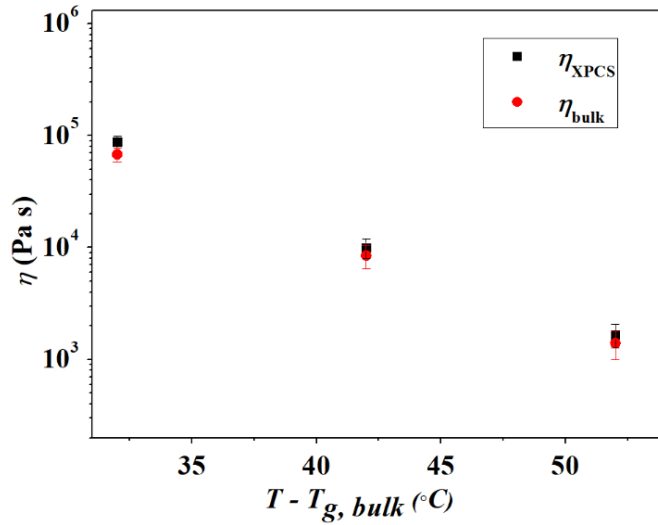


Figure 5.2. Comparison of viscosities from XPCS (black squares) and bulk rheology (red circles) as a function of temperature for SPS.

Plots of τ/h vs. $q_{||}h$ and fits to HCT for three thinner films are shown in Figure 5.3. The largest deviations are seen for the thinnest film (28.7 nm). The key observation is that the maximum thickness at which viscosity enhancement is observed is 72 nm ($26R_g$), which is much larger than the critical thicknesses for LPS ($4R_g$)⁵² and CPS thin films ($10R_g$ for $14k$ ⁴⁵ or $16R_g$ for $6k$ ³⁹). Although τ/h values for SPS films of thickness < 72 nm are all above the universal curve anticipated by the HCT, the data can still be fit with the HCT using either an effective viscosity higher than the bulk viscosity or a smaller value of h_{eff} , without inclusion of a shear modulus.⁵²

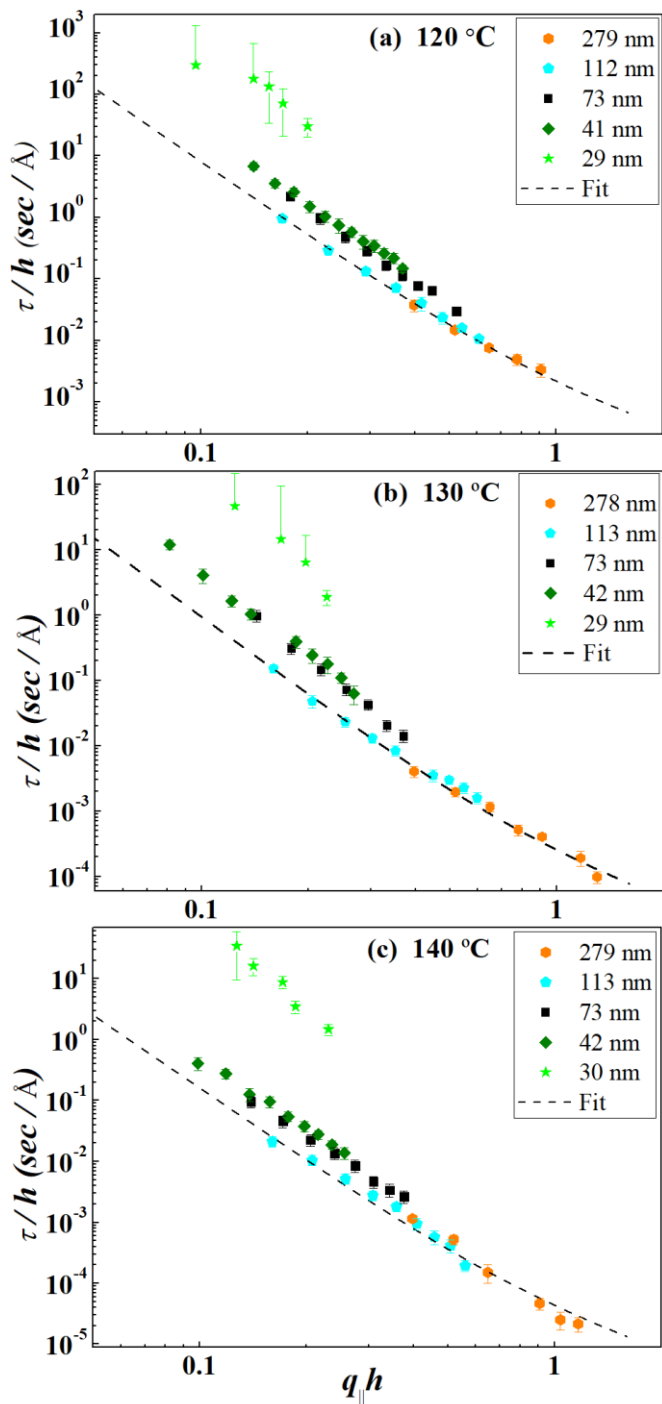


Figure 5.3. τ/h vs $q_{\parallel}h$ for SPS films with various thicknesses at (a) 120 °C (b) 130 °C and (c) 140°C. The dashed curves correspond to least-square fits to the HCT using the data for h of 112 and 277 nm.

If we assume that this behavior can be described using a two-layer model,^{39, 77} the bottom layer having extremely high viscosity and the layer next to air having bulk viscosity, then h_{vis} must be about 17 nm ($6R_g$) to collapse the data for various thicknesses onto the universal curve at three temperatures, as shown in Figure 5.4 (where h_{vis} varies by ± 1 nm). All the data except for that of the 28.7 nm sample collapse reasonably well onto a single curve consistent with the HCT for a single film of thickness h_{eff} .

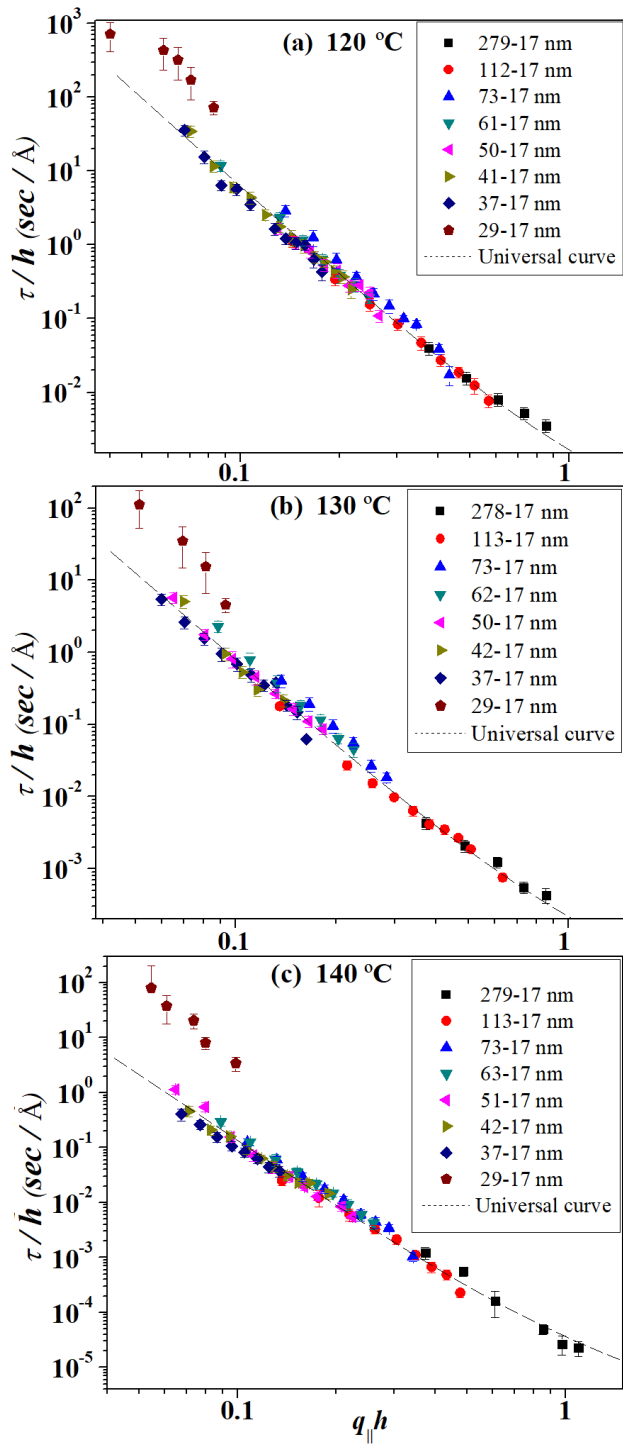


Figure 5.4. Collapse of the τ/h vs $q_{\parallel}h$ data at three temperatures achieved by assuming an effective thickness, h_{eff} , for the film equal to total thickness minus the highly viscous layer thickness ($h-h_{\text{vis}}$, as shown in legend).

How do we explain the tethering of the SPS at the substrate leading to such enormous increases in viscosity at distances many times R_g from the substrate? Koga *et al.*⁷⁰ argue that entanglements are key to propagating slow dynamics from a $1R_g$ thick irreversibly adsorbed layer up into a melt film of 123k LPS ($R_g = 10$ nm) to cause an order of magnitude enhancement in viscosity 30 nm ($3R_g$) from the substrate. Zhou *et al.*⁷⁷ find the surface fluctuations on a similar 123k LPS film on silicon can be rationalized by assuming a 27 nm ($2.7R_g$) thick layer of infinite viscosity at the substrate, but the result from Koga *et al.*⁷⁰ indicates there is a more gradual gradient in viscosity in such films that extends farther even than h_{vis} . Roth and coworkers¹⁰⁸ have suggested that increases in local T_g extending up to 100 nm (ca. $13R_g$ of the 110k tethered chains) into films of highly entangled chains as a result of covalently tethering ca. 10 vol% of chains next to the substrate result from interactions between chains. However, it has already been shown experimentally that chains do not have to be entangled to propagate slow dynamics from a sluggish interfacial layer. Earlier work by Foster and collaborators¹⁰⁹ shows that covalently tethering 28k LPS chains to the substrate in a blend with 2k LPS chains slows surface fluctuations by at least three orders of magnitude for a film thickness of 45 nm ($10R_{g,tethered}$), and by factors of four and two, respectively, for films of 70 and 90 nm thickness (15 and $20R_{g,tethered}$) even though the tethered chains extend only 22-26 nm ($\sim 5R_g$) into the film.

For our 15k SPS films in which the “tethered” interfacial layer is formed by irreversible physisorption, the penetration of tethered portions of chains up into the melt is even more subtle. The irreversibly adsorbed layer, when collapsed after rinsing, is also only $1R_g$ (2.7nm) in thickness, but a value of $h_{vis} = 17$ nm has to be assumed to fit the XPCS data.

MD simulations by Green *et al.*⁵⁹ show (their Fig. 1) that for a “weakly adsorbing interface” with stars having eight arms of length 10 beads, the extension of the arms of the physisorbed stars into the melt is only of order R_g , which is far less than the extension into the melt one can have with covalently end-tethered linear chains of the same overall M . The propagation of the slow dynamics with these 15k four-arm stars, which have arms even shorter than those of the 36k end-branched stars studied earlier⁹, must then depend significantly on the friction between arms of different molecules that are not tethered to the substrate, and are not entangled, but only interpenetrate¹⁰.

A final issue is how to explain the dramatic viscosity enhancement of the thinnest film. For that film, postulating a 17 nm viscous layer at the substrate is insufficient, with an order of magnitude discrepancy between the relaxation time predicted by the two-layer model and the observed value. Two additional features are probably important for explaining the largest effect in the thinnest film. First, changes in segmental mobility with depth near interfaces are not abrupt, but are better described as gradients^{72, 110}. Although what we are looking at here is viscosity, which is associated with chain movement instead of segmental mobility, we still expect the changes with depth to be gradual, not abrupt. Work done by Fakhraai¹¹¹ showed that the slowdown in translational chain dynamics is directly correlated to decreased polymer segmental motion under nanoconfinement. That would suggest the film should have a viscosity gradient in the film if there is a T_g gradient. Additionally, measurements of local T_g by Torkelson *et al.*^{25, 26} using fluorescence techniques suggest that the T_g gradients evolve as film thickness decreases. When the film is sufficiently thin, the gradients from the two interfaces overlap and influence the entire

film thickness roughly equivalently. As simulations of Green *et al.*⁷⁸ suggest a weaker localization of star placement exists at the air/polymer surface with a concomitant increase in viscosity, we conjecture that for the 4-arm SPS films viscosity is enhanced at both interfaces, leading to the dramatic increase in relaxation time. We note that the thickness relative to R_g at which this overlap occurs for the unentangled stars is much larger than the relative thicknesses at which Torkelson *et al.*^{72, 110} posit such gradient overlap in films of highly entangled (400k and 800k) linear chains.

CHAPTER VI

VISCOSITY ENHANCEMENT IN SUPPORTED MELT FILMS OF TADPOLE-SHAPED POLYSTYRENE

In this chapter, the effect of junction points and chain ends on surface fluctuations will be addressed further through study of tadpole-shaped polymer melt films. A group of films of 6k tadpole-shaped PS with thicknesses from 10 to $80R_g$ were prepared and measured using XPCS. The behavior observed strongly suggests that with the annealing protocol used the films were not at equilibrium and therefore the results must be considered in light of that possibility. Rationalizing the data using the same two-layer model with a highly viscous layer next to substrate as was used in the previous chapter is still possible. Also, the irreversibly adsorbed layer remaining after rinsing could be studied using XR to gain further insight into the character of the region of enhanced viscosity that is formed before the film is fully annealed.

Tadpole-shaped polystyrenes with narrow molecular weight distributions were synthesized by anionic polymerization, silicon linking chemistry and ring-closure metathesis. The architecture and structure of the 6k tadpole-shaped polystyrene were verified using SEC, ^1H NMR and MALDI-ToF MS as described in Chapter 4. The surface fluctuations of melts of these novel nonlinear polymers were then studied using XPCS. Before XPCS measurements the samples were annealed following a protocol used previously. The T_g was measured and the samples were annealed at a temperature of $T_g + 20$ °C for 12 hours. This conservative annealing protocol was intended to minimize the possibility of dewetting of the films due to the fact that there was very little material to

work with. Unfortunately, that initial T_g value proved to be low. The T_g was later determined (by S. Simon and Y. Koh) in a set of self-consistent measurements with chains of other architecture and the actual T_g was found to be 13 °C higher (88.0 °C). Thus, it appears the samples were actually annealed at $T_g + 7^\circ\text{C}$ for 12 hours. Data for a second set of samples annealed in the same way, but made using a first batch of TPS that was later found to contain trace contaminant are described in Appendix A.

In order to prepare for interpreting the XPCS data, the surface tension values for tadpole-shaped PS at various temperatures were calculated based on the surface tension of the 6k LPS using a group contribution method,¹¹² and the bulk viscosities for tadpole-shaped PS at the corresponding temperatures were measured by with rheometry. The values obtained are listed in Table 6.1.

Table 6.1. Surface Tensions of 6k Tadpole-shaped Polystyrene

Temperature (°C)	$\gamma^{\text{linear}}{}^a$ (mN/m)	$\eta^{\text{bulk}}{}^a$ (Pa s)
115	32.5	110000
125	31.9	10600
135	31.3	1800

^aThe uncertainty in the surface tension value and bulk viscosity value is estimated to be $\pm 5\%$

Using the same model and equation 5.1 described in Chapter 5, again the viscosity data allowed us to estimate the amount of annealing that would have been expected to result in equilibrium behavior for a bulk samples. Here, η_s is 1×10^8 Pa S, T is 368K and N is 145; b and k stay the same. The bulk Rouse relaxation time at the annealing temperature is

estimated to be 20400s and we annealed the films at 368k for 12h (43200s). In contrast to the annealing condition for the 15k star films in Chapter 5, the annealing time here is just enough for the film to reach equilibrium, assuming the chains throughout the film exhibit bulk viscosity. However, the viscosity is apparently not equal to the bulk value all the way through the film. Previous works^{70, 72} have proven that the T_g and viscosity of the polymer chains near a substrate can be much larger than those of bulk material. Additionally, for a non-equilibrium entangled polymer thin film, annealing allows the recovery of entanglement networks¹¹³⁻¹¹⁴, which certainly does not happen in the annealing process for our 6k TPS chains. Based on this information, the annealing here is sufficient for chains far away from the substrate to reach equilibrium, but insufficient for those chains near the substrate, including the adsorbed chains, and perhaps those chains constrained by interpenetrating with the adsorbed chains. Thus, the annealing essentially affects the evolution of the adsorbed layer associated with polymer-substrate interaction and chain rearrangement⁶⁹, which could further affect the thickness of the highly viscous layer. With these calculations of equilibration times in mind we proceed to consider the XPCS results.

Examples of g_2 functions at nine values of $q_{||}$ from the 6k Tadpole-shaped PS for 111 nm thickness at 115 °C are shown in Figure 6.1. Generally, for such melt films, the g_2 functions are best behaved for data from the thickest films and higher temperatures (farther from T_g). Here, the g_2 functions of all the films could be well fit using a single exponential form with no stretching, even at 115 °C, which is 27 °C above T_g . There are no clues in the shapes of the g_2 functions to suggest that the samples are out of equilibrium.

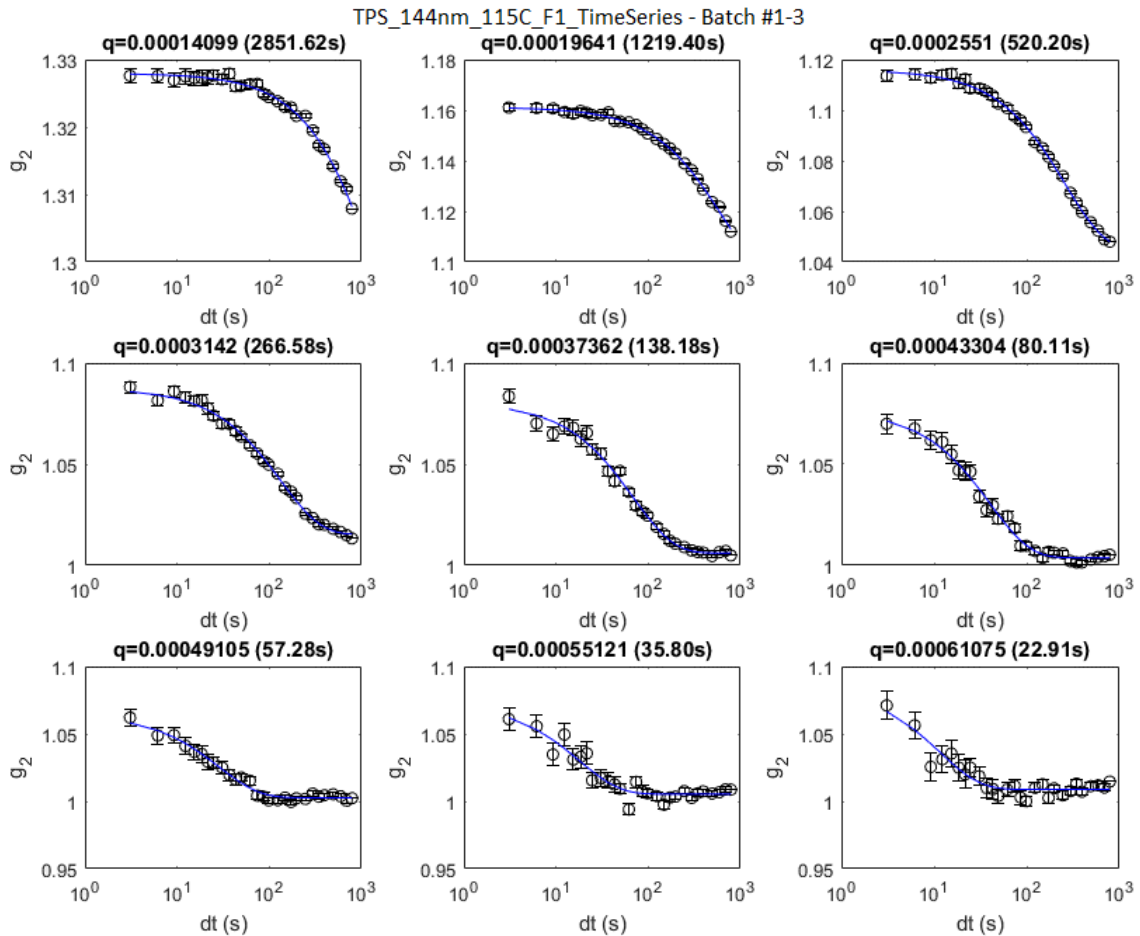


Figure 6.1. g_2 Functions at nine values of $q_{||}$ from TPS film of 144 nm thickness.

For the pure tadpole-shaped PS, the viscosity derived from fitting the data for films with thicknesses of 144, 122 and 111 nm using the HCT is a factor of three or four larger than the measured bulk viscosity at each measurement temperature, as shown in Figure 6.2. For films thicker than 112 nm, the plots of τ/h vs. $q_{||}h$ seem to overlap at each temperature, as would be expected if the HCT applied. For the film with thickness of 70 nm, the data overlap with those of thicker films at 115 °C and 125 °C. However, the 70 nm film data deviate from the overlapping behavior at 135 °C. It could be that the fact the deviation shows up at 135 °C is due to some change in behavior with increase in $T - T_g$. However,

one has to be careful in drawing conclusions about the effect of the temperature itself because the samples were measured with the protocol that involved measuring from lowest temperature to highest temperature. Thus, the samples at 135 °C have also been at elevated temperature longer than were the samples at 115 °C and 125 °C. It is instructive here to compare to the results of He et al.³⁹ for the 6k analog cyclic PS. They found that the XPCS data for films with evident viscosity enhancement deviated more from the universal behavior at the second highest temperature than at the lower temperature measured, but then the deviation became smaller at the highest temperature, though still larger than the deviation at the lowest temperature (i.e. 3.4nm “highly viscous layer at 140 °C , 9.0 nm at 150 °C and 6.2 nm at 160 °C). Already the results of He¹¹⁵ suggested that, even for PS without entanglement, the annealing conditions used may not have been sufficient for the chains to fully equilibrate in the thin films. Here the annealing is taking place at a temperature even closer to T_g . If the strongly adsorbed layer film was still developing at 125 °C, when the temperature was raised to 135 °C the adsorbed layer may have grown additionally in thickness enough so that deviation from the overlapped data manifested itself for the 70 nm thick film. So far there isn’t evidence from any other source that the effect of the strongly adsorbed layer should simply grow as $T-T_g$ grows. Thus, we consider this an unlikely explanation.

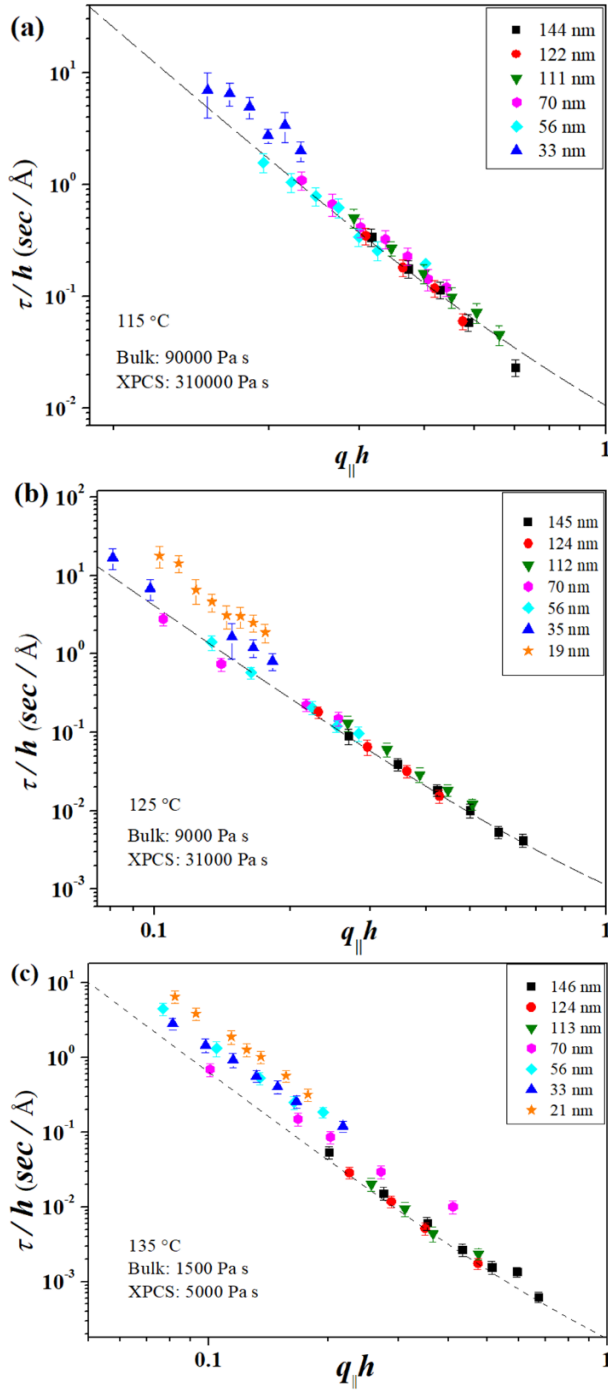


Figure 6.2. τ/h vs $q_{\parallel}h$ for TPS films with various thicknesses at (a) 115 °C, (b) 125 °C and (c) 135 °C. The dashed curves correspond to the HCT allowing the viscosity to float as a fitting parameter. The viscosity required to fit the data that overlap is substantially above bulk viscosity at each temperature.

Since data of thicker films overlap at each temperature, the plots of τ/h vs $q_{//}h$ for films of the thicknesses 144, 122, 111 nm can be well described by fitting with HCT using the film viscosity as a fitting parameter as shown in Figure 6.2. The comparison of viscosities of the melts in the films derived from fitting the XPCS data for the thickest TPS films and viscosities obtained from rheometry is shown in Figure 6.3. The viscosities obtained from XPCS are about three or four times larger than those from rheometry. This difference is larger than what has been seen in the literature in comparisons of XPCS derived bulk viscosities and rheometrically derived bulk viscosities from any previous works on surface fluctuations of PS.^{4, 38-39, 45, 47, 77} We suggest two possibilities for explaining this discrepancy. One is that there is some new mechanism at work here with the tadpole molecules that has not been seen before. The second is that the bulk viscosity measurement was inaccurate due to difficulties with eliminating air bubbles in the sample when measuring the rheometry. Steps are always taken when setting up the rheometry measurements to minimize bubbles, but they are difficult to completely eliminate and they can result in reported viscosity values substantially below the actual value. Since the synthesis of tadpole molecules is so new, we know of no data from others' work that would provide a ready comparison with ours. Viscosities of tadpole molecules of three molecular weights have been measured by Matsushita et al.,³⁷ but those data are all for tadpoles with total M and cycle M larger than the critical molecular weight for entanglement for linear PS (38k), so those results are not readily extrapolated into the M range studied here. However, for the present we assume that the bulk rheology value is too small due to measurement inaccuracy.

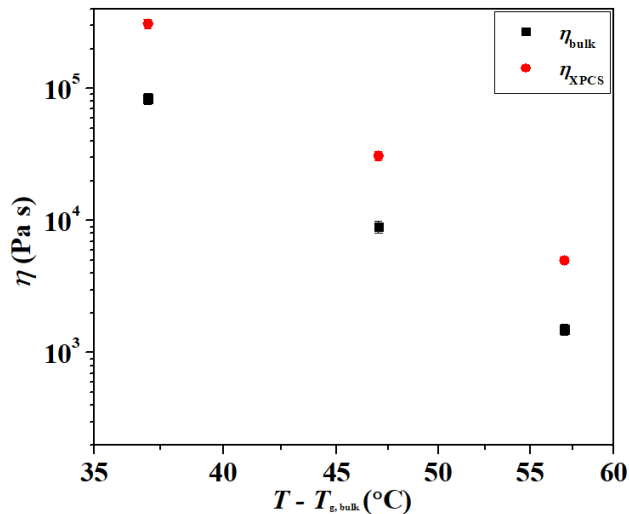


Figure 6.3. Comparison of viscosities obtained from fitting the XPCS data for thicker films (black square) and from bulk rheometry (red circle) as a function of temperature for the 6k TPS.

The same two-layer model with a highly viscous layer next to the substrate that was introduced in Chapter 5 was used here also to rationalize the data and to infer a thickness of a highly viscous layer at each temperature. It seems possible to collapse the data from all the available thicknesses at each of the three temperatures using a different viscous layer thickness at each temperature, as shown in Figure 6.4. The thickness of the highly viscous layer next to the substrate, inferred from this model, seems to grow from 6 to 7 to 10 nm as temperature goes up from 125 °C to 135 °C. The easiest explanation for the thickness change with temperature seems to be that the films were still annealing during the XPCS measurements.

We had hoped to be able to make close comparison with data from He et al.³⁹ for 6k CPS. However, the values of $T - T_g$ at which the two types of films were annealed and measured do not match well. He et al. annealed the samples for 12 h at 120 °C, which

corresponds to $T-T_g$ of 22 °C. Here, the annealing time was also 12 h, but, due to difficulties in determining the T_g accurately for tadpole molecules, the annealing was done at $T-T_g$ of 7 °C ($T_{\text{anneal}} = 95$ °C). The tadpole samples were annealed at a temperature much closer to T_g and thus are probably farther from thermal equilibrium than were the cyclic samples studied by He et al.³⁹ The time the TPS films spent at 115, 125, and 135 °C during the XPCS measurements was all “annealing time”. This is probably the reason that the highly viscous layer thickness needed to explain the data is higher for the higher measurement temperature. At each measurement temperature the adsorbed layer at the substrate was still developing. In one sense this is similar to what was seen by He¹¹⁵ who found it necessary to postulate a viscous layer thickness of 3.4 nm at 140 °C, 9 nm at 150 °C and 6.2 nm at 160 °C. Apparently at 140 °C and 150 °C the adsorbed layer was still growing during XPCS measurement, but upon going to 160 °C some chains in the adsorbed layer have sufficient mobility to reorganize, reducing the effective adsorbed layer thickness some.

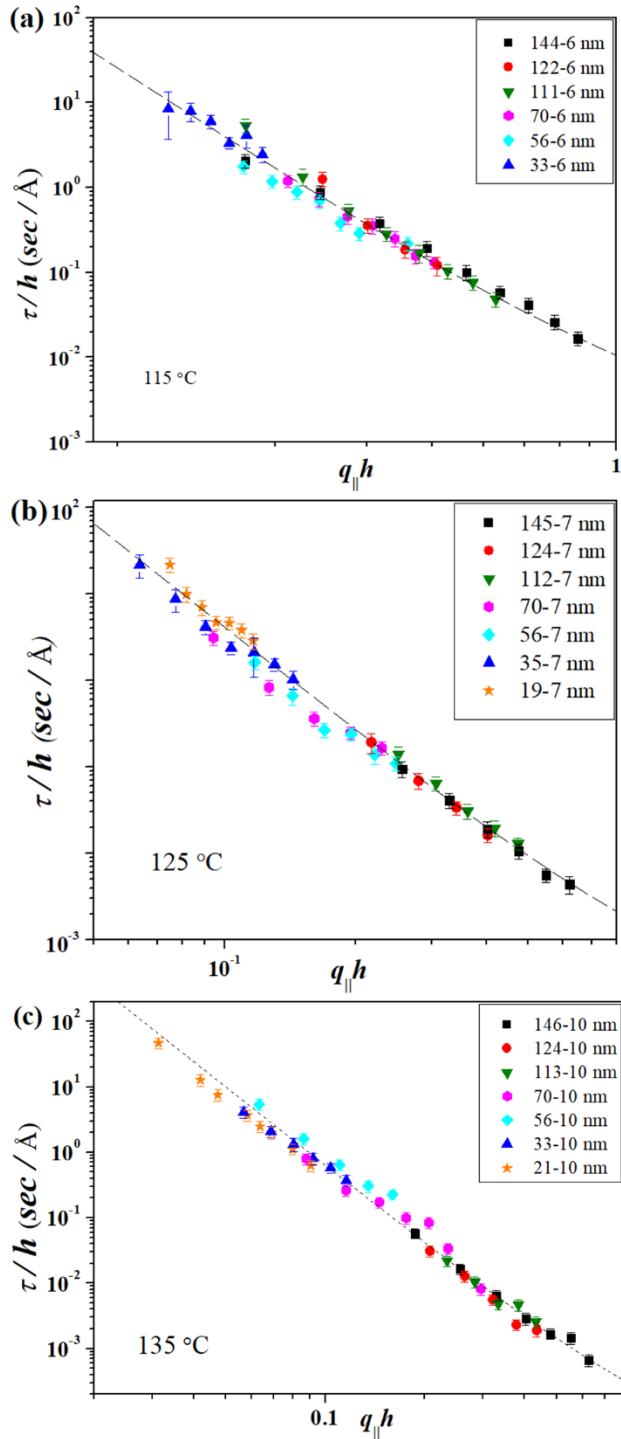


Figure 6.4. Collapse of the τ/h vs $q_{\parallel}h$ data at three temperatures achieved by assuming an effective thickness, h_{eff} , for the film, shown in the legend, which is equal to total thickness minus the highly viscous layer thickness.

Again, one of the TPS films was rinsed with toluene to reveal the irreversibly adsorbed layer and the actual thickness of that layer was probed indirectly using X-ray reflectivity as demonstrated in Chapter 5. The reflectivity curve for the TPS irreversibly adsorbed layer on silicon for a 40 nm thick sample after measurement at 115, 125, and 135 °C in the XPCS beam line is shown in Figure 6.5. By fitting the curve, the scattering length density (SLD) profile was obtained, as shown in the inset of Figure 6.5. The SLD profile shows a clear plateau for the PS between air and substrate. The model that emerges from the fitting can be thought of as consisting of two regions of PS material of different mass densities with a strongly smeared interface between air and PS; the layer next to air being 8.5 Å thick with SLD of $8.9 \times 10^{-6} \text{ \AA}^{-2}$, which is identical to the bulk PS SLD value and the other being 11.2 Å thick with SLD of $10.7 \times 10^{-6} \text{ \AA}^{-2}$, which is 20% larger than the bulk value. If we define the overall thickness of the irreversibly adsorbed layer as being the distance from the middle of the interface with air to the middle of the interface with the substrate (as sketched in the figure) the overall thickness is $19.6 \pm 0.5 \text{ \AA}$, or slightly larger than $1R_g$, which is between the relative thicknesses of such layers seen for the 6k linear and 6k cyclic analogs, which were $1R_g$ and $2.3R_g$, respectively.¹¹⁵ This is consistent with the expectation that introduction of the linear tails should disrupt the compact packing of cyclic chains.

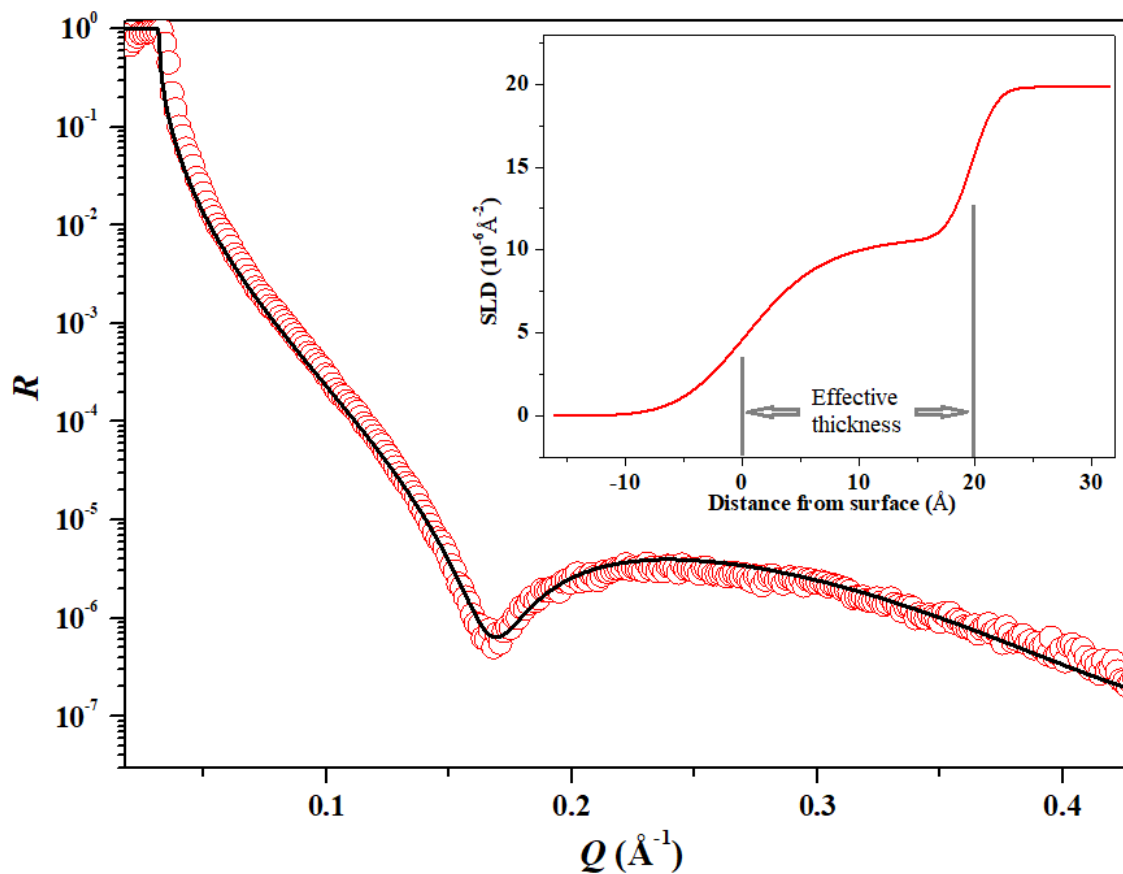


Figure 6.5. X-ray reflectivity of the irreversibly adsorbed layer remaining after rinsing a 40 nm thick, annealed TPS film and drying in a high vacuum oven. The solid line represents the best fit to the data with the SLD depth profile shown in the inset.

The highly viscous layer postulated to explain the surface fluctuation dynamics in these systems and films of other nonlinear architectures has consistently been found to be thicker than the irreversibly adsorbed layer measured after rinsing. That is, the slow dynamics that we readily associate with the irreversibly adsorbed layer must be propagating up into the melt above the adsorbed layer. Koga et al.⁷⁰ has argued that in films of linear chains of M much above the critical molecular weight for entanglement, M_c , the slowed dynamics of the adsorbed layer propagate into the melt by means of entanglements.

While this explanation is reasonable for conventionally entangled melts it does not work for explaining the difference between the irreversibly adsorbed layer thickness and the highly viscous layer thickness in the present case. This propagation of slow dynamics without conventional entanglements is seen both for the low M stars of the previous chapter and for the tadpoles and represents an important theme of this dissertation research. For the stars we attributed the propagation to “interpenetration” of arms of neighboring chains. Though the chains do not entangle conventionally, the interpenetration of arms that are tethered at the centers of adjacent molecules provides a means of generating dynamic interactions that go beyond what is seen with linear chains.

With the tadpoles the alternative to conventional entanglement must take some different form since there are not multiple arms for interpenetration. However, the tadpoles do contain cycles, and this invites the suggestion that threading might be a mechanism for propagating the slow dynamics. Threading is known to be an important mechanism in the dynamics of large macrocyclics, such as DNA.¹¹⁶⁻¹¹⁸ Key to threading, though, is the cycle being large enough for something else to fit in the center of the cycle. In this case, MD simulations by Tsige et al.¹¹⁹ have suggested that once a PS cycle is larger than 2k it is possible for a linear portion of a PS chain to fit inside the cycle. For our case the cycle has a molecular weight of 4k, and thus threading is possible. However, for such small cycles threading is thought to be highly improbable, considering that the cycles are not fully expanded in the melt. Nonetheless, at this time the threading of the tail of one tadpole through the cycle of another TPS molecule seems the only mechanism available to provide

a means for “interpenetration” to propagate the slow dynamics of the irreversibly adsorbed layer.

CHAPTER VI

CONCLUSIONS

Conclusions can be drawn in three different aspects of the research. The first part of the research addressed the efficient synthesis and characterization of well-defined tadpole-shaped polystyrene, since the synthesis of polymers with this architecture allows us to incisively investigate the effect of architecture in terms of chain end and branching point on physical properties, especially surface fluctuations. This synthetic approach is a combination of living anionic polymerization, silicon chloride linking chemistry and metathesis ring-closure methods. Characterization with GPC, NMR and MALDI-ToF MS proved that this is an efficient way of synthesizing tadpole-shaped polystyrene with predictable molecular weight and narrow molecular weight distribution. As compared to previous synthetic methods, this approach has the advantages of high stability of the precursor, high yield of cyclic formation without further purification steps (fractionation or HPLC), and small size of the junction point, i.e. that of a single atom. This approach can be utilized to synthesize tadpole-shaped polystyrene with molecular weight up to 130k, and can also be applied to make tadpole-shaped chains with other monomers once high yield of vinyl end functionalization is obtained with those monomers. The glass transition temperature of the tadpole-shaped PS is 2.7 °C higher than that of its linear analog and 11.7 °C higher than that of the three-arm star analog, due to lower free volume with fewer chain ends. For these molecules in which the junction is a single atom, the change in T_g with architecture is adequately explained by considering self-plasticization by chain ends,

which highlights the importance of the structure of the junction point in terms of explaining physical properties.

The second part of the research addressed the study of surface fluctuations for 15k four-arm star polystyrene. The thickness at which viscosity enhancement manifests itself for melt films of these four-arm star chains is much larger than that for melt films of linear and cyclic polystyrene chains in terms of thickness relative to chain size, R_g . The surface fluctuation behavior for most thicknesses can be described using a two-layer model postulating the existence of a highly viscous layer next to the substrate that is much thicker for the star chains than for linear or cyclic chains. The irreversibly adsorbed layer resisting rinsing was measured to be only $1R_g$ in thickness. We conjecture the modestly branched chains have optimal conformations for forming a first layer next to the substrate that is strongly adsorbed, but still able to interact significantly with chains much further from the substrate, resulting in a remarkable slowing down despite the absence of conventional entanglements. The gradients in mobility at the substrate and free surface come closer together as the film thickness is reduced, finally overlapping for a film of thickness $10R_g$ to cause an even more striking enhancement of viscosity.

The final part of the research further addressed the role of branching and chain end on surface fluctuations. For the surface fluctuations of films of pure TPS, the viscosities derived from XPCS data using the HCT for the thicker films are about a factor of three or four larger than the viscosities obtained from rheology measurements. This discrepancy might be due to inaccurate rheology measurements. Data for thinner films deviate from the overlapping behavior in the τ/h vs. $q_{||}h$ plot due to viscosity enhancement near the substrate.

Collapse of the data using a two-layer model requires a highly viscous layer with different thicknesses at different temperatures, which evidently shows that the films were not fully equilibrated and the highly viscous layer was still evolving during the measurement. The irreversibly adsorbed layer revealed by rinsing a film of pure TPS with good solvent was measured using X-ray reflectivity to be $1R_g$ thick, which is between the irreversibly adsorbed layer thicknesses for the LPS and CPS analogs. This is consistent with the expectation that introduction of the linear tails should disrupt the compact packing of cyclic chains. The highly viscous layer being thicker than the irreversibly adsorbed layer suggests that the slow dynamics near the substrate can propagate through molecular interpenetration so that a part of the film much thicker than the irreversibly adsorbed layer is ultimately affected.

REFERENCES:

- (1) Hiller, J. A.; Mendelsohn, J. D.; Rubner, M. F., Reversibly Erasable Nanoporous Anti-Reflection Coatings from Polyelectrolyte Multilayers. *Nat. Mater.* **2002**, *1*, 59.
- (2) Martin, C. R., Nanomaterials: A Membrane-Based Synthetic Approach. *Science* **1994**, *266*, 1961.
- (3) Hawker, C. J.; Russell, T. P., Block Copolymer Lithography: Merging “Bottom-Up” with “Top-Down” Processes. *MRS Bulletin* **2011**, *30*, 952-966.
- (4) Wang, S.-F.; Yang, S.; Lee, J.; Akgun, B.; Wu, D. T.; Foster, M. D., Anomalous Surface Relaxations of Branched-Polymer Melts. *Phys. Rev. Lett.* **2013**, *111*, 068303.
- (5) Beinat, S.; Schappacher, M.; Deffieux, A., Linear and Semicyclic Amphiphilic Diblock Copolymers. 1. Synthesis and Structural Characterization of Cyclic Diblock Copolymers of Poly(hydroxyethyl vinyl ether) and Linear Polystyrene and Their Linear Homologues. *Macromolecules* **1996**, *29*, 6737-6743.
- (6) Oike, H.; Uchibori, A.; Tsuchitani, A.; Kim, H.-K.; Tezuka, Y., Designing Loop and Branch Polymer Topology with Cationic Star Telechelics through Effective Selection of Mono- and Difunctional Counteranions. *Macromolecules* **2004**, *37*, 7595-7601.
- (7) Li, H.; Debuigne, A.; Jérôme, R.; Lecomte, P., Synthesis of Macrocyclic Poly(ϵ -caprolactone) by Intramolecular Cross-Linking of Unsaturated End Groups of Chains Precyclic by the Initiation. *Angew. Chem. Int. Ed.* **2006**, *45*, 2264-2267.
- (8) Shi, G.-Y.; Tang, X.-Z.; Pan, C.-Y., Tadpole-shaped Amphiphilic Copolymers Prepared via RAFT Polymerization and Click Reaction. *J. Polym. Sci. A* **2008**, *46*, 2390-2401.
- (9) Zhang, B.; Zhang, H.; Grayson, S. M. Tadpole-shaped Amphiphilic Poly(ethylene glycol)-*b*-polycaprolactone Copolymer Polymer Prepared by Ring-opening Polymerization and Click Chemistry, *Abstracts of Papers of the American Chemical Society*, 245th National Spring Meeting of the American Chemical Society, New Orleans, LA, April 7-11, 2013; American Chemical Society: Washington, DC, 2013 PSME 305.
- (10) Doi, Y.; Ohta, Y.; Nakamura, M.; Takano, A.; Takahashi, Y.; Matsushita, Y., Precise Synthesis and Characterization of Tadpole-Shaped Polystyrenes with High Purity. *Macromolecules* **2013**, *46*, 1075-1081.
- (11) Wang, S. F. Synthesis and Characterization of Surface Relaxations of Macrocyclic Polystyrenes and Interfacial Segregation in Blends with Linear Polystyrenes. Ph.D. Dissertation, University of Akron, Akron, OH, 2011.

- (12) He, Q.; Yol, A. M.; Wang, S.-F.; Ma, H.; Guo, K.; Zhang, F.; Wesdemiotis, C.; Quirk, R. P.; Foster, M. D., Efficient Synthesis of Well-defined Cyclic Polystyrenes using Anionic Polymerization, Silicon Chloride Linking Chemistry and Metathesis Ring Closure. *Polym. Chem.* **2016**, *7*, 5840-5848.
- (13) Quirk, R. P.; Wang, S.-F.; Foster, M. D.; Wesdemiotis, C.; Yol, A. M., Synthesis of Cyclic Polystyrenes Using Living Anionic Polymerization and Metathesis Ring-Closure. *Macromolecules* **2011**, *44*, 7538-7545.
- (14) He, Q. M.; Mao, J.; Wesdemiotis, C.; Quirk, R. P.; Foster, M. D., Synthesis and Isomeric Characterization of Well-Defined 8-Shaped Polystyrene Using Anionic Polymerization, Silicon Chloride Linking Chemistry, and Metathesis Ring Closure. *Macromolecules* **2017**, *50*, 5779-5789.
- (15) Hsieh, H. L.; Quirk, R. P., *Anionic Polymerization: Principles and Practical Applications*. Marcel Dekker: New York, 1996.
- (16) Quirk, R. P.; Pickel, D. L., Controlled End-Group Functionalization (including Telechelics). In *Polymer Science: A Comprehensive Reference*, Matyjaszewski, K.; Moller, M., Eds. Elsevier BV: Amsterdam, 2012; Vol. 6, pp 351-412.
- (17) Ziegler, K., Die Bedeutung Der Alkalimetallorganischen Verbindungen für Die Synthese. *Angew. Chem.* **1936**, *49*, 499-502.
- (18) Szwarc, M., 'Living' Polymers. *Nature* **1956**, *178*, 1168.
- (19) Szwarc, M.; Levy, M.; Milkovich, R., Polymerization Initiated by Electron Transfer to Monomer. A New Method of Formation of Block Polymers. *J. Am. Chem. Soc.* **1956**, *78*, 2656-2657.
- (20) Morton, M.; Fetters, L. J., Anionic Polymerization of Vinyl Monomers. *Rubber Chem. Technol.* **1975**, *48*, 359-409.
- (21) Webster, O. W., Living Polymerization Methods. *Science* **1991**, *251*, 887.
- (22) Waack, R.; Doran, M. A., Reactivities of Organolithium Compounds in Tetrahydrofuran. I. As Vinyl Polymerization Initiators. *J. Org. Chem.* **1967**, *32*, 3395-3399.
- (23) Takano, A.; Furutani, T.; Isono, Y., Preparation of a Polystyrene Macromonomer with a Novel Anionic Initiator Containing an Olefinic Vinyl Group. *Macromolecules* **1994**, *27*, 7914-7916.
- (24) Morton, M., *Anionic Polymerization: Principles and Practice*. Academic Press: New York, 1983.
- (25) Bauer, B. J.; Fetters, L. J., Synthesis and Dilute-Solution Behavior of Model Star-Branched Polymers. *Rubber Chem. Technol.* **1978**, *51*, 406-436.

- (26) Hadjichristidis, N.; Pitsikalis, M.; Pispas, S.; Iatrou, H., Polymers with Complex Architecture by Living Anionic Polymerization. *Chem. Rev.* **2001**, *101*, 3747-3792.
- (27) Hunt, M. O.; Belu, A. M.; Linton, R. W.; DeSimone, J. M., End-functionalized Polymers. 1. Synthesis and Characterization of Perfluoroalkyl-terminated Polymers via Chlorosilane Derivatives. *Macromolecules* **1993**, *26*, 4854-4859.
- (28) Pennisi, R. W.; Fetters, L. J., Preparation of Asymmetric 3-arm Polybutadiene and polystyrene Stars. *Macromolecules* **1988**, *21*, 1094-1099.
- (29) Mays, J. W., Synthesis of "Simple graft" poly(isoprene-g-styrene) by Anionic Polymerization. *Polym. Bull.* **1990**, *23*, 247-250.
- (30) Uhrig, D.; Hong, K.; Mays, J. W.; Kilbey, S. M.; Britt, P. F., Synthesis and Characterization of an ABC Miktoarm Star Terpolymer of Cyclohexadiene, Styrene, and 2-Vinylpyridine. *Macromolecules* **2008**, *41*, 9480-9482.
- (31) Bielawski, C. W.; Benitez, D.; Grubbs, R. H., An "Endless" Route to Cyclic Polymers. *Science* **2002**, *297*, 2041.
- (32) Tezuka, Y.; Komiya, R., Metathesis Polymer Cyclization with Telechelic Poly(THF) Having Allyl Groups. *Macromolecules* **2002**, *35*, 8667-8669.
- (33) Endo, K., Synthesis and Properties of Cyclic Polymers. In *New Frontiers in Polymer Synthesis*, Kobayashi, S., Ed. Springer Berlin Heidelberg: Berlin, Heidelberg, 2008; pp 121-183.
- (34) Roovers, J.; Toporowski, P. M., Relaxation by Constraint Release in Combs and Star-combs. *Macromolecules* **1987**, *20*, 2300-2306.
- (35) Milner, S. T.; McLeish, T. C. B., Arm-Length Dependence of Stress Relaxation in Star Polymer Melts. *Macromolecules* **1998**, *31*, 7479-7482.
- (36) Larson, R. G., Combinatorial Rheology of Branched Polymer Melts. *Macromolecules* **2001**, *34*, 4556-4571.
- (37) Doi, Y.; Takano, A.; Takahashi, Y.; Matsushita, Y., Melt Rheology of Tadpole-Shaped Polystyrenes. *Macromolecules* **2015**, *48*, 8667-8674.
- (38) Liu, B.; Narayanan, S.; Wu, D. T.; Foster, M. D., Polymer Film Surface Fluctuation Dynamics in the Limit of Very Dense Branching. *Macromolecules* **2013**, *46*, 3190-3197.
- (39) He, Q.; Narayanan, S.; Wu, D. T.; Foster, M. D., Confinement Effects with Molten Thin Cyclic Polystyrene Films. *ACS Macro Lett.* **2016**, *5*, 999-1003.
- (40) Zhang, L.; Elupula, R.; Grayson, S. M.; Torkelson, J. M., Major Impact of Cyclic Chain Topology on the T_g -Confinement Effect of Supported Thin Films of Polystyrene. *Macromolecules* **2016**, *49*, 257-268.

- (41) Hossain, M. D.; Lu, D.; Jia, Z.; Monteiro, M. J., Glass Transition Temperature of Cyclic Stars. *ACS Macro Lett.* **2014**, *3*, 1254-1257.
- (42) Gan, Y.; Dong, D.; Hogen-Esch, T. E., Effects of Lithium Bromide on the Glass Transition Temperatures of Linear and Macrocyclic Poly(2-vinylpyridine) and Polystyrene. *Macromolecules* **1995**, *28*, 383-385.
- (43) Ueberreiter, K.; Kanig, G., Self-plasticization of Polymers. *J. Colloid Interface Sci.* **1952**, *7*, 569-583.
- (44) Pipertzis, A.; Hossain, M. D.; Monteiro, M. J.; Floudas, G., Segmental Dynamics in Multicyclic Polystyrenes. *Macromolecules* **2018**, *51*, 1488-1497.
- (45) Wang, S.-F.; Jiang, Z.; Narayanan, S.; Foster, M. D., Dynamics of Surface Fluctuations on Macrocyclic Melts. *Macromolecules* **2012**, *45*, 6210-6219.
- (46) Ghatak, A.; Chaudhury, M. K., Adhesion-Induced Instability Patterns in Thin Confined Elastic Film. *Langmuir* **2003**, *19*, 2621-2631.
- (47) Kim, H.; Rühm, A.; Lurio, L. B.; Basu, J. K.; Lal, J.; Lumma, D.; Mochrie, S. G. J.; Sinha, S. K., Surface Dynamics of Polymer Films. *Phys. Rev. Lett.* **2003**, *90*, 068302.
- (48) Josef, J., The spectrum of Surface Waves on Viscoelastic Liquids of Arbitrary Depth. *J. Phys. Condens. Matter* **1998**, *10*, 7121-7131.
- (49) Gutt, C.; Sprung, M.; Fendt, R.; Madsen, A.; Sinha, S. K.; Tolan, M., Partially Wetting Thin Liquid Films: Structure and Dynamics Studied with Coherent X Rays. *Phys. Rev. Lett.* **2007**, *99*, 096104.
- (50) Demirel, A. L.; Granick, S., Origins of Solidification When a Simple Molecular Fluid is Confined Between Two Plates. *J. Chem. Phys.* **2001**, *115*, 1498-1512.
- (51) Wang, J.; Tolan, M.; Seeck, O. H.; Sinha, S. K.; Bahr, O.; Rafailovich, M. H.; Sokolov, J., Surfaces of Strongly Confined Polymer Thin Films Studied by X-Ray Scattering. *Phys. Rev. Lett.* **1999**, *83*, 564-567.
- (52) Jiang, Z.; Kim, H.; Jiao, X.; Lee, H.; Lee, Y. J.; Byun, Y.; Song, S.; Eom, D.; Li, C.; Rafailovich, M. H.; Lurio, L. B.; Sinha, S. K., Evidence for Viscoelastic Effects in Surface Capillary Waves of Molten Polymer Films. *Phys. Rev. Lett.* **2007**, *98*, 227801.
- (53) Fujii, Y.; Yang, Z.; Leach, J.; Atarashi, H.; Tanaka, K.; Tsui, O. K. C., Affinity of Polystyrene Films to Hydrogen-Passivated Silicon and Its Relevance to the T_g of the Films. *Macromolecules* **2009**, *42*, 7418-7422.
- (54) Gennes, P. G. d., Some Conformation Problems for Long Macromolecules. *Rep. Prog. Phys.* **1969**, *32*, 187.

- (55) O'Shaughnessy, B.; Vavylonis, D., Irreversibility and Polymer Adsorption. *Phys. Rev. Lett.* **2003**, *90*, 056103.
- (56) Srebnik, S.; Chakraborty, A. K.; Shakhnovich, E. I. Adsorption-Freezing Transition for Random Heteropolymers near Disordered 2D Manifolds due to "Pattern Matching". *Phys. Rev. Lett.* **1996**, *77*, 3157-3160.
- (57) Möddel, M.; Bachmann, M.; Janke, W. Conformational Mechanics of Polymer Adsorption Transitions at Attractive Substrates. *J. Phys. Chem. B* **2009**, *113*, 3314-3323.
- (58) Möddel, M.; Janke, W.; Bachmann, M. Adsorption and Pattern Recognition of Polymers at Complex Surfaces with Attractive Stripelike Motifs. *Phys. Rev. Lett.* **2014**, *112*, 148303.
- (59) Glynos, E.; Frieberg, B.; Chremos, A.; Sakellariou, G.; Gidley, D. W.; Green, P. F. Vitrification of Thin Polymer Films: From Linear Chain to Soft Colloid-like Behavior. *Macromolecules* **2015**, *48*, 2305-2312.
- (60) Karalus, S.; Janke, W.; Bachmann, M. Thermodynamics of Polymer Adsorption to A Flexible Membrane. *Phys. Rev. E* **2011**, *84*, 031803.
- (61) Blavatska, V.; Janke, W. Polymer Adsorption on A Fractal Substrate: Numerical Study. *J. Chem. Phys.* **2012**, *136*, 104907.
- (62) Guiselin, O., Irreversible Adsorption of a Concentrated Polymer Solution. *EPL* **1992**, *17*, 225.
- (63) Durning, C. J.; O'Shaughnessy, B.; Sawhney, U.; Nguyen, D.; Majewski, J.; Smith, G. S., Adsorption of Poly(methyl methacrylate) Melts on Quartz. *Macromolecules* **1999**, *32*, 6772-6781.
- (64) Napolitano, S.; Lupaşcu, V.; Wübberhorst, M., Temperature Dependence of the Deviations from Bulk Behavior in Ultrathin Polymer Films. *Macromolecules* **2008**, *41*, 1061-1063.
- (65) Rotella, C.; Napolitano, S.; De Cremer, L.; Koeckelberghs, G.; Wübberhorst, M., Distribution of Segmental Mobility in Ultrathin Polymer Films. *Macromolecules* **2010**, *43*, 8686-8691.
- (66) Napolitano, S.; Pilleri, A.; Rolla, P.; Wübberhorst, M., Unusual Deviations from Bulk Behavior in Ultrathin Films of Poly(*tert*-butylstyrene): Can Dead Layers Induce a Reduction of T_g ? *ACS Nano* **2010**, *4*, 841-848.
- (67) Housmans, C.; Sferrazza, M.; Napolitano, S., Kinetics of Irreversible Chain Adsorption. *Macromolecules* **2014**, *47*, 3390-3393.
- (68) Gin, P.; Jiang, N.; Liang, C.; Taniguchi, T.; Akgun, B.; Satija, S. K.; Endoh, M. K.; Koga, T., Revealed Architectures of Adsorbed Polymer Chains at Solid-Polymer Melt Interfaces. *Phys. Rev. Lett.* **2012**, *109*, 265501.

- (69) Simavilla, D. N.; Huang, W.; Vandestruck, P.; Ryckaert, J.-P.; Sferrazza, M.; Napolitano, S., Mechanisms of Polymer Adsorption onto Solid Substrates. *ACS Macro Lett.* **2017**, *6*, 975-979.
- (70) Koga, T.; Jiang, N.; Gin, P.; Endoh, M. K.; Narayanan, S.; Lurio, L. B.; Sinha, S. K., Impact of an Irreversibly Adsorbed Layer on Local Viscosity of Nanoconfined Polymer Melts. *Phys. Rev. Lett.* **2011**, *107*, 225901.
- (71) Ellison, C. J.; Torkelson, J. M., The Distribution of Glass-transition Temperatures in Nanoscopically Confined Glass Formers. *Nat. Mater.* **2003**, *2*, 695.
- (72) Askar, S.; Torkelson, J. M., Stiffness of Thin, supported Polystyrene Films: Free-surface, Substrate, and Confinement Effects Characterized via Self-referencing Fluorescence. *Polymer* **2016**, *99*, 417-426.
- (73) Napolitano, S.; Wübbenhorst, M., The lifetime of the Deviations from Bulk Behaviour in Polymers Confined at the Nanoscale. *Nat. Commun.* **2011**, *2*, 260.
- (74) Jiang, N.; Shang, J.; Di, X.; Endoh, M. K.; Koga, T., Formation Mechanism of High-Density, Flattened Polymer Nanolayers Adsorbed on Planar Solids. *Macromolecules* **2014**, *47*, 2682-2689.
- (75) Bal, J. K.; Beuvier, T.; Unni, A. B.; Chavez Panduro, E. A.; Vignaud, G.; Delorme, N.; Chebil, M. S.; Grohens, Y.; Gibaud, A., Stability of Polymer Ultrathin Films (<7 nm) Made by a Top-Down Approach. *ACS Nano* **2015**, *9*, 8184-8193.
- (76) Burroughs, M. J.; Napolitano, S.; Cangialosi, D.; Priestley, R. D., Direct Measurement of Glass Transition Temperature in Exposed and Buried Adsorbed Polymer Nanolayers. *Macromolecules* **2016**, *49*, 4647-4655.
- (77) Zhou, Y.; He, Q.; Zhang, F.; Yang, F.; Narayanan, S.; Yuan, G.; Dhinojwala, A.; Foster, M. D., Modifying Surface Fluctuations of Polymer Melt Films with Substrate Modification. *ACS Macro Lett.* **2017**, *6*, 915-919.
- (78) Glynos, E.; Johnson, K. J.; Frieberg, B.; Chremos, A.; Narayanan, S.; Sakellariou, G.; Green, P. F., Free Surface Relaxations of Star-Shaped Polymer Films. *Phys. Rev. Lett.* **2017**, *119*, 227801.
- (79) Harden, J. L.; Pleiner, H.; Pincus, P. A., Hydrodynamic Surface Modes on Concentrated Polymer Solutions and Gels. *J. Chem. Phys.* **1991**, *94*, 5208-5221.
- (80) Sinha Sunil, K.; Jiang, Z.; Lurio Laurence, B., X-ray Photon Correlation Spectroscopy Studies of Surfaces and Thin Films. *Adv. Mater.* **2014**, *26*, 7764-7785.
- (81) Hadjichristidis, N.; Iatrou, H.; Pispas, S.; Pitsikalis, M., Anionic Polymerization: High Vacuum Techniques. *J. Polym. Sci. A* **2000**, *38*, 3211-3234.

- (82) Uhrig, D.; Mays, J. W., Experimental Techniques in High-vacuum Anionic Polymerization. *J. Polym. Sci. A* **2005**, *43*, 6179-6222.
- (83) Quirk, R. P.; Ocampo, M., Anionic Polymerization. *Material Matters* **2006**, *1*, 10-13.
- (84) Ashby, E. C., The Manipulation of Air-sensitive Compounds (Shriver, D. F.). *J. Chem. Educ.* **1970**, *47*, A721.
- (85) Sekutowski, D. G.; Stucky, G. D., A Simple Oxygen Test to Use in Dry Boxes Containing a Solvent Vapor Atmosphere. *J. Chem. Educ.* **1976**, *53*, 110.
- (86) Kim, J.; Jeong Seo, Y.; Kim Kwang, U.; Ahn Young, H.; Quirk Roderic, P., Anionic Dispersion Polymerization. I. Control of Particle Size. *J. Polym. Sci. A* **1996**, *34*, 3277-3288.
- (87) Quirk Roderic, P.; Ma, J. J., Characterization of the Functionalization Reaction Product of Poly(styryl)lithium with Ethylene Oxide. *J. Polym. Sci. A* **1988**, *26*, 2031-2037.
- (88) Gilman, H.; Cartledge, F. K., The Analysis of Organolithium Compounds. *J. Organomet. Chem.* **1964**, *2*, 447-454.
- (89) Watkins, E. K.; Jorgensen, W. L., Perfluoroalkanes: Conformational Analysis and Liquid-State Properties from ab Initio and Monte Carlo Calculations. *J. Phys. Chem. A* **2001**, *105*, 4118-4125.
- (90) Tatek, Y. B.; Tsige, M., Structural Properties of Atactic Polystyrene Adsorbed onto Solid Surfaces. *J. Chem. Phys.* **2011**, *135*, 174708.
- (91) Plimpton, S., Fast Parallel Algorithms for Short-Range Molecular Dynamics. *J. Comput. Phys.* **1995**, *117*, 1-19.
- (92) Piranha solution is corrosive, so acid-resistant gloves, protective goggles, and lab coats are required when handling the piranha solution.
- (93) Quirk, R. P.; Jang, S. H.; Kim, J. Recent Advances in Anionic Synthesis of Functionalized Elastomers Using Functionalized Alkylolithium Initiators. *Rubber Chem. Technol.* **1996**, *69*, 444-461.
- (94) Hsieh, H. L.; Glaze, W. H. Kinetics of Alkylolithium Initiated Polymerizations. *Rubber Chem. Technol.* **1970**, *43*, 22-73.
- (95) Bywater, S.; Worsfold, D. J. Anionic Polymerization of Styrene Effect of Tetrahydrofuran. *Can. J. Chem.* **1962**, *40*, 1564-1570.
- (96) Quirk, R. P.; Yin, J. Carbonation of Polymeric Organolithium Compounds: Effects of Chain End Structure. *J. Polym. Sci. A* **1992**, *30*, 2349-2355.

- (97) Lee, C.; Gido, S. P.; Pitsikalis, M.; Mays, J. W.; Tan, N. B.; Trevino, S. F.; Hadjichristidis, N. Asymmetric Single Graft Block Copolymers: Effect of Molecular Architecture on Morphology. *Macromolecules* **1997**, *30*, 3732-3738.
- (98) Roovers, J.; Toporowski, P. M. Synthesis of High Molecular Weight Ring Polystyrenes. *Macromolecules* **1983**, *16*, 843-849.
- (99) Laurent, B. A.; Grayson, S. M. Synthetic Approaches for the Preparation of Cyclic Polymers. *Chem. Soc. Rev.* **2009**, *38*, 2202-2213.
- (100) Roovers, J., Organic Cyclic Polymers. In *Cyclic Polymers*, Semlyen, J. A., Ed. Springer Netherlands: Dordrecht, 2002; pp 347-384.
- (101) Kok, C. M.; Rudin, A. Relationship between the Hydrodynamic Radius and the Radius of Gyration of a Polymer in Solution. *Macromol. Rapid Commun.* **1981**, *2*, 655-659.
- (102) Hayashi, S.; Adachi, K.; Tezuka, Y. An Efficient Route to Cyclic Polymers by ATRP-RCM Process. *Chem. Lett.* **2007**, *36*, 982-983.
- (103) Huang, D.; Simon, S. L.; McKenna, G. B. Chain Length dependence of the Thermodynamic Properties of Linear and Cyclic Alkanes and Polymers. *J. Chem. Phys.* **2005**, *122*, 084907.
- (104) Gaur, U.; Wunderlich, B. Heat Capacity and Other Thermodynamic Properties of Linear Macromolecules. V. Polystyrene. *J. Phys. Chem. Ref. Data* **1982**, *11*, 313-325.
- (105) Fox, T. G.; Flory, P. J. Second-Order Transition Temperatures and Related Properties of Polystyrene. I. Influence of Molecular Weight. *J. Appl. Phys.* **1950**, *21*, 581-591.
- (106) Qian, Z.; Minnikanti, V. S.; Sauer, B. B.; Dee, G. T.; Kampert, W. G.; Archer, L. A. Surface Tension of Polystyrene Blends: Theory and Experiment. *J. Polym. Sci. B* **2009**, *47*, 1666-1685.
- (107) Qian, Z.; Minnikanti, V. S.; Sauer, B. B.; Dee, G. T.; Archer, L. A. Surface Tension of Symmetric Star Polymer Melts. *Macromolecules* **2008**, *41*, 5007-5013.
- (108) Huang, X.; Roth, C. B. Optimizing the Grafting Density of Tethered Chains to Alter the Local Glass Transition Temperature of Polystyrene near Silica Substrates: The Advantage of Mushrooms over Brushes. *ACS Macro Lett.* **2018**, *7*, 269-274.
- (109) Lee, J. K.; Akgun, B.; Jiang, Z.; Narayanan, S.; Foster, M. D. Altering Surface Fluctuations by Blending Tethered and Untethered chains. *Soft Matter* **2017**, *13*, 8264-8270.

- (110) Kim, S.; Torkelson, J. M. Distribution of Glass Transition Temperatures in Free-Standing, Nanoconfined Polystyrene Films: A Test of de Gennes' Sliding Motion Mechanism. *Macromolecules* **2011**, *44*, 4546-4553.
- (111) Hor, J. L.; Wang, H.; Fakhraai, Z.; Lee, D. Effect of Physical Nanoconfinement on the Viscosity of Unentangled Polymers during Capillary Rise Infiltration. *Macromolecules* **2018**, *51*, 5069-5078.
- (112) Koberstein, J. T., Molecular Design of Functional Polymer Surfaces. *J. Polym. Sci. B* **2004**, *42*, 2942-2956.
- (113) McGraw, J. D.; Fowler, P. D.; Ferrari, M. L.; Dalnoki-Veress, K. Relaxation of Non-equilibrium Entanglement Networks in Thin Polymer Films. *Eur. Phys. J. E* **2013**, *36*, 7.
- (114) Barbero, D. R.; Steiner, U. Nonequilibrium Polymer Rheology in Spin-Cast Films. *Phys. Rev. Lett.* **2009**, *102*, 248303.
- (115) He, Q. Synthesis of Cyclic and Multicyclic Polystyrenes and Their Surface Fluctuations in Melt Polymer Films. Ph.D. Dissertation, University of Akron, Akron, OH, 2017.
- (116) Önfelt, B.; Lincoln, P.; Nordén, B. Enantioselective DNA Threading Dynamics by Phenazine-Linked [Ru(phen)2dppz]2+ Dimers. *J. Am. Chem. Soc* **2001**, *123*, 3630-3637.
- (117) Searcey, M.; Noel Martin, P.; Howarth, N. M.; Madden, B.; Wakelin, L. P. G. DNA Threading Agents: Effect of Sidechain Bulk on DNA Binding and Cytotoxicity of 9-Anilinoacridine-4-carboxamides. *Bioorganic Med. Chem. Lett.* **1996**, *6*, 1831-1836.
- (118) Tanious, F. A.; Jenkins, T. C.; Neidle, S.; Wilson, W. D. Substituent Position Dictates the Intercalative DNA-binding Mode for Anthracene-9,10-dione Antitumor Drugs. *Biochemistry* **1992**, *31*, 11632-11640.
- (119) Tsige, M. University of Akron, Akron, OH. Unpublished work, 2018.

APPENDIX A

SURFACE FLUCTUATIONS OF TADPOLE-SHAPED POLYSTYRENE WITH 0.5% HIGH MOLECULAR WEIGHT DIMER IMPURITY

The first attempt to synthesis the 6k TPS resulted in a material that apparently contained a high molecular weight impurity (TPS_2). The GPC traces comparison shown in Figure A.1 exhibits a very small high molecular weight shoulder for this TPS_2. Characterization of this high molecular weight impurity proved difficult. It appears to constitute less than 0.5 wt% of the sample. A possible dimeric structure for the contaminant is shown in Figure A.2. If this structure is correct, then the molar mass should be twice that of the 6k desired product and might be visible in MALDI-ToF MS measurements. The MALDI MS result for this material is shown in Figure A.3. We know from other measurements that it is possible to analyze 13k linear PS with this MALDI instrument, but no signal appears here in the neighborhood of $m/z = 12k$. When XPCS measurements were carried out with this material, it was thought to be pure and the detailed analysis of the TPS structure was not achieved until after the XPCS data were collected.

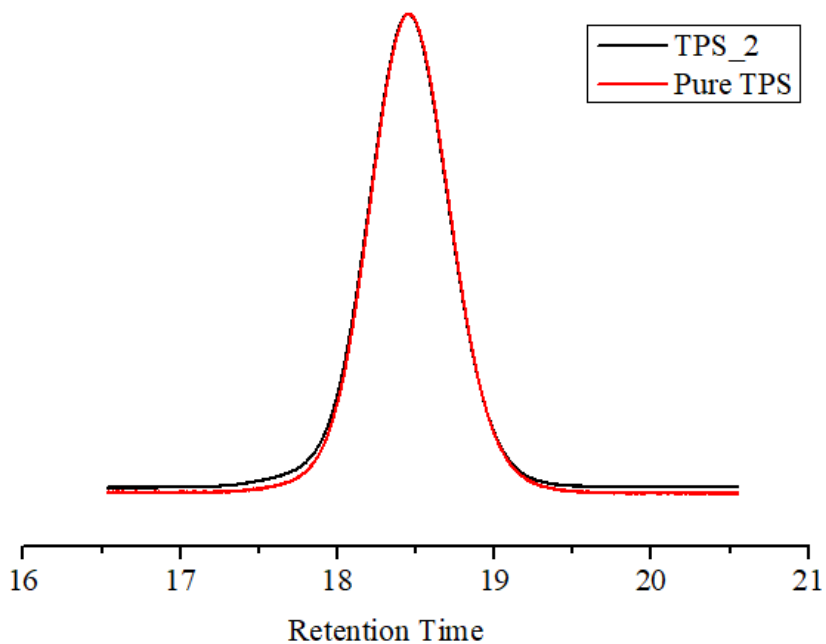


Figure A.1. GPC traces comparison between pure TPS and TPS with high molecular weight impurity.

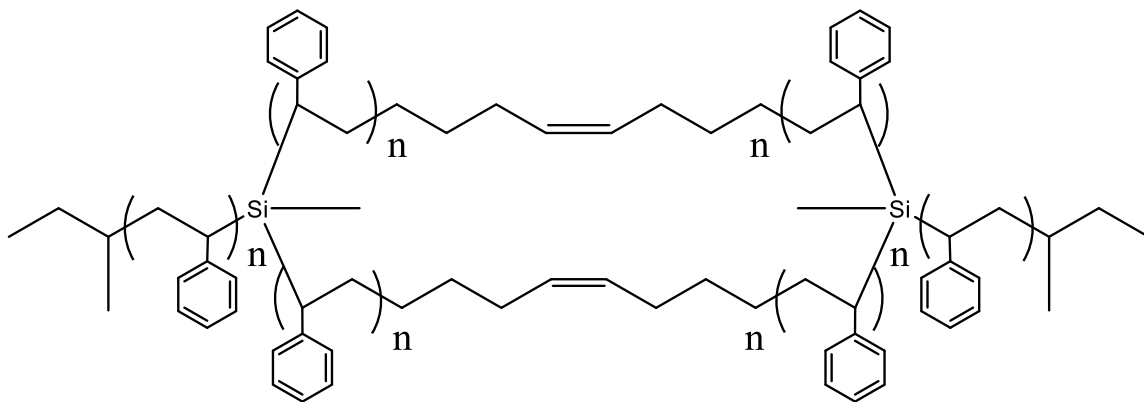


Figure A.2. Possible chemical structure for the high molecular weight species.

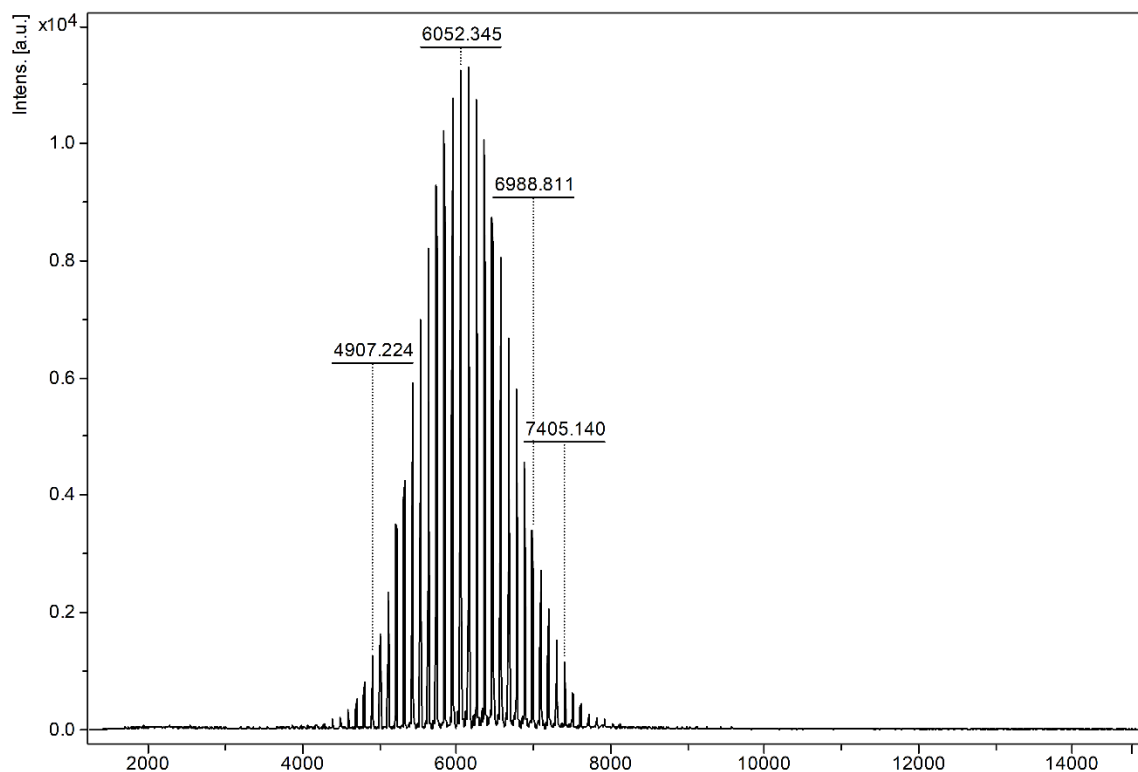


Figure A.3. MALDI MS result for TPS_2, no signal is present at $m/z = 12000$.

The effects of the trace high molecular weight contaminant in the TPS on surface fluctuations are striking. A group of films of TPS_2 with thicknesses from 10 to $100R_g$ (assuming that $\langle R_g \rangle$ is negligibly affected by the presence of the contaminant) were prepared and measured using XPCS. The viscosities inferred by analyzing the XPCS data for thick films using HCT were compared with values obtained from bulk rheology on the pure material (as presented in Chapter 6). A two-layer model was used to rationalize the data to infer a thickness of the highly viscous layer. The irreversibly adsorbed layer was revealed using the procedure described in Chapter 5 and studied using XR to provide further insight into the mechanism behind the viscosity enhancement.

The data for films of thickness larger than 51 nm collapse onto a universal curve and are well described by the HCT using the measured bulk viscosity at each temperature, as shown in Figure A.4. The viscosities of the melts in the films derived from XPCS data for TPS_2 are compared with viscosities obtained from bulk rheometry in Figure A.5. The differences between the viscosity value inferred from XPCS and the bulk value from rheometry are of order 25%, which is consistent with the degree of agreement found between XPCS derived viscosities and bulk viscosities reported by other authors for other PS chain architectures.^{4, 38-39, 45, 47} For these film thicknesses there is no need to invoke the presence of any strongly adsorbed layer to explain the surface fluctuations. However, it is essential to note that the relaxation times observed with these films of TPS contaminated with trace high molecular weight species are roughly 100x smaller than those measured for films made from the pure TPS, as is evident from the comparison in Figure A.6 of data for the thicker films from the two types of materials.

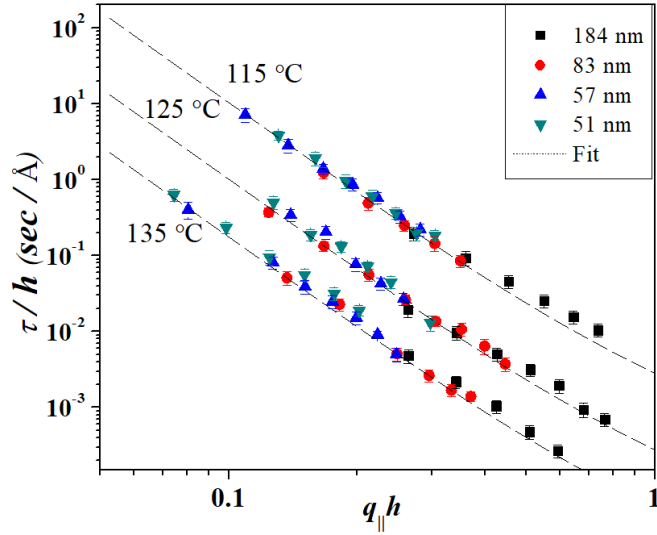


Figure A.4. τ/h vs. $q_{||}h$ for tadpole-shaped PS with high molecular weight impurity (TPS_2) films at various temperatures. The dashed curves represent least squares fits to the HCT with η_{XPCS} as a fitting parameter.

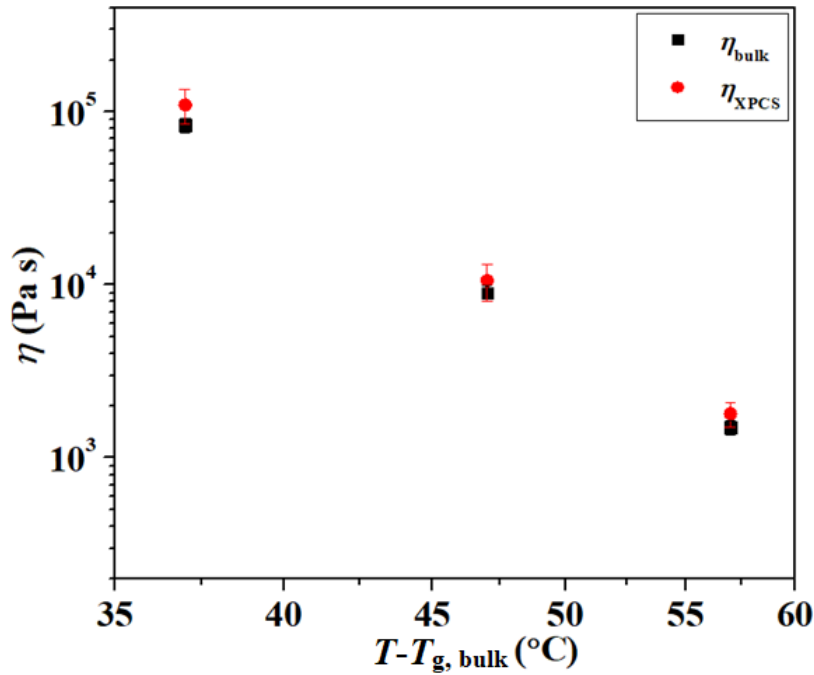


Figure A.5. Comparison of zero shear viscosities obtained from XPCS data (black squares) and from bulk rheology (red circles) as a function of temperature for the TPS_2.

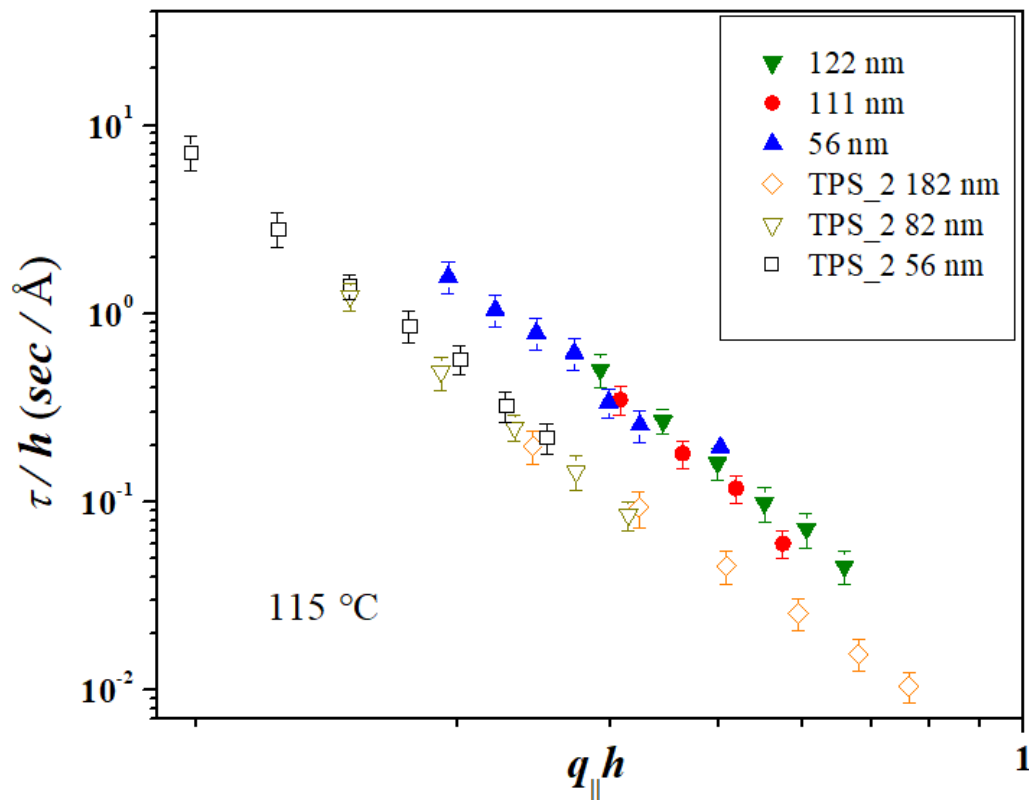


Figure A.6. Comparison of data for thicker films from pure TPS and TPS with high molecular weight impurity.

Viscosity enhancement manifests itself at a thickness of 26 nm ($\sim 14R_g$) at all measured temperatures, as shown in Figure A.7. At the lowest temperature, 115 °C, the surface fluctuations for the thinner films (< 26 nm) are so slow that they cannot be resolved in our experimental window. The g_2 functions are flat for runs lasting up to 1528 seconds. Therefore, viscosity enhancement becomes evident at some thickness between 51 and 26 nm. We note that viscosity enhancement for TPS_2 films becomes evident at a relative thickness similar to the relative thickness ($14R_g$) at which viscosity enhancement manifests itself in 6k cyclic film.³⁹

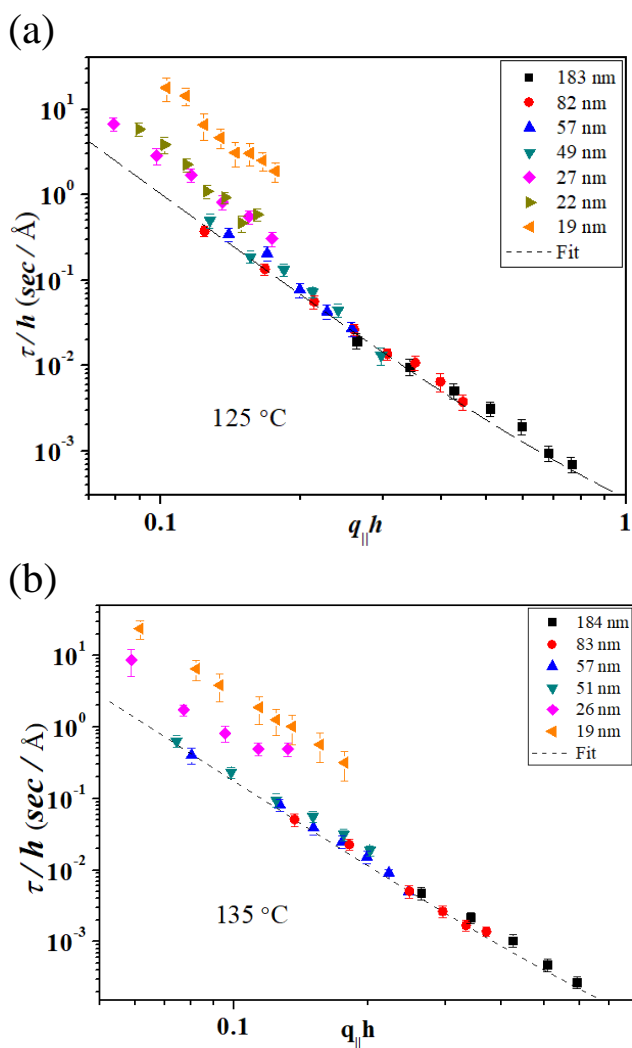


Figure A.7. τ/h vs $q_{\parallel}h$ for TPS_2 films with various thicknesses at (a) $125\text{ }^{\circ}\text{C}$ and (b) $135\text{ }^{\circ}\text{C}$. The dashed curves correspond to least-square fits to the HCT using the data for h of 184 nm, 83 nm, 57 nm and 51 nm.

An attempt has been made to collapse the data from films of all thicknesses using the same two-layer model mentioned above in order, once again, to infer a thickness of a highly viscous layer at each temperature. Similar to what was observed for the surface fluctuations of 15k four-arm star PS melt films, Figure A.7 shows that the data from the

films of thickness 27 nm and lower do not collapse onto the HCT curve that describes well the data for thicker film. However, once again, collapsing the data can be achieved for some thinner films by introducing the two-layer model and an “effective thickness” that has bulk viscosity. With this model, the highly viscous layer next to the substrate has to be 6 nm or 10 nm in thickness to rationalize the surface fluctuation behavior for the films of thickness 22 and 26 nm thickness at 125 °C and 135 °C, respectively, as shown in Figure A.8. We note, however, that even this model is not sufficient to collapse the data from the 19 nm thick film to the HCT curve. In order to get the data for the 19 nm thick film to collapse more or less onto one curve with the other thicknesses the highly viscosity has to be assumed to have a thickness of 12.5 nm at 125 °C and 13.5 nm at 135 °C.

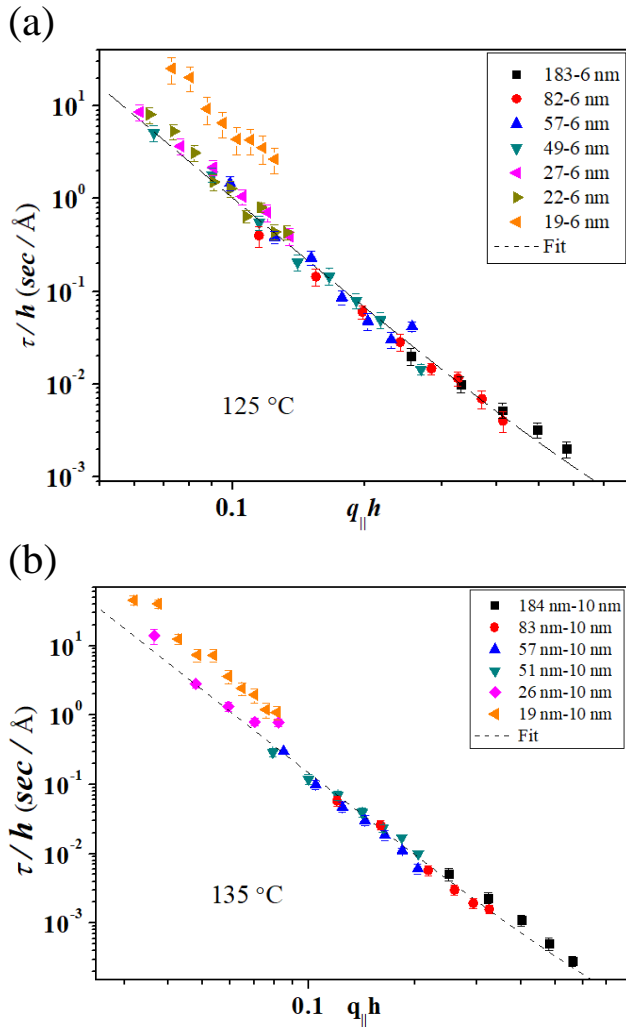


Figure A.8. Collapse of the τ/h vs $q_{||}h$ data at three temperatures achieved by assuming an effective thickness, h_{eff} , for the film equal to total thickness minus the highly viscous layer thickness.

Again, one of the TPS_2 films was rinsed with toluene to reveal the layer of irreversibly adsorbed chains that collapsed against the substrate after removal from solvent and was studied using XR to gain insight into the behavior of chains next to the substrate.

The reflectivity curve for the TPS_2 irreversibly adsorbed layer on silicon for a 25 nm thick sample after measurement at 135 °C in the XPCS beam line is shown in Figure A.9.

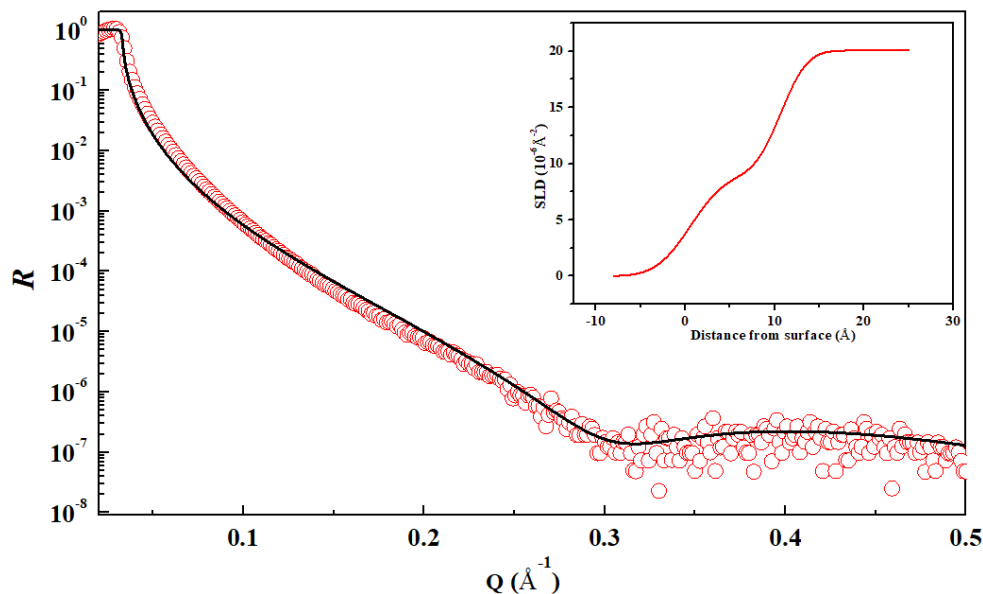


Figure A.9. X-ray reflectivity of the irreversibly adsorbed layer remaining after rinsing a 25 nm thick, annealed TPS_2 film and drying in a high vacuum oven. The solid line represents the best fit to the data with the SLD depth profile shown in the inset.

Even without fitting the XR data it is evident that the irreversibly adsorbed layer obtained in this case is less well defined than the layer obtained from the films of pure TPS. By fitting the XR curve, the scattering length density (SLD) profile shown in the inset of Figure A.9 was obtained. Unlike the typical SLD profile for a spun-cast PS film, here we can barely see a plateau in SLD for the PS between air and substrate. The model that emerges from the fitting can be thought of as consisting of two layers of PS material of different mass densities with a strongly smeared interface in between, the layer next to air being 1.1 Å thick with SLD of $3.6 \times 10^{-6} \text{ \AA}^{-2}$ and roughness of 1.2 Å rms and the other being 9.6 Å thick with SLD of $7.9 \times 10^{-6} \text{ \AA}^{-2}$, which is still 10% smaller than the bulk value,

which for 6k LPS of bulk density is known to be $8.9 \times 10^{-6} \text{ \AA}^{-2}$. Apparently the presence of the contaminant affects enormously the way in which the chains organize at the interface in the 12 hours provided for annealing. The effect of this second layer next to the air in the model is to lead to a SLD profile that is slightly asymmetric in shape there. Clearly the strongly adsorbed layer as a whole is not very well defined. It is rough and has a density below bulk density, through somewhat higher than the density seen by He¹¹⁵ for the irreversibly adsorbed layer of a linear analog (80% ρ_{bulk}) and less than the relative density seen for the cyclic adsorbed layer, which was 98% of its bulk density. The overall nominal thickness of the irreversibly adsorbed layer is 10.7 \AA , or only $0.6R_g$, which is substantially thinner than the relative thicknesses seen for both the linear and cyclic analogs, which were $1R_g$ and $2.3R_g$, respectively.¹¹⁵ There are at least two possible explanations for this. The first could be that the contaminant in this material disrupts the packing at the interface somewhat, as compared to the pure tadpole material. The other is that the strongly adsorbed layer is simply not as well developed as for either the linear or cyclic analogs because the TPS_2 films were annealed for the same time, but at a temperature much closer to the glass transition temperature and therefore did not have the opportunity to build such a well-optimized strongly adsorbed layer. The difference in structures of the strongly adsorbed layer for the TPS without contaminant and with contaminant are more challenging to explain, however.

Comparison with the behavior of a pure tadpole material, discussed in the Chapter 6, clearly shows that although the annealing conditions were exactly the same for pure TPS and TPS_2, the irreversibly adsorbed layer in the pure TPS film is 83% thicker than that in

the TPS₂ film, and the overall density is also higher. These results are two further evidences that when the contaminant is absent the packing of the chains is more efficient. Furthermore, from this comparison of the irreversibly adsorbed layers for pure TPS and TPS₂ it seems probable that when the higher molecular weight contaminant is present in TPS₂ the film requires a longer time to establish a well-optimized irreversibly adsorbed layer.

What is most important to note is that the thickness of the irreversibly adsorbed layer measured after rinsing is much less than the thickness of the highly viscous layer postulated to explain the surface fluctuation dynamics. That is, whatever was going on in the melt at 125 °C or 135 °C it involved the propagation of slowing of the melt movement much farther into the melt than the thickness of the layer remaining after rinsing. Thus, we see evidence of a phenomenon similar to that important for the star melt films. The adsorbed layer that can be evidenced by rinsing is only 1 nm thick, but the hydrodynamic flow of the melt is perturbed somehow even 10 nm or more away from the substrate. Again, the question that arises is how this could be. An attractive possibility to consider for tadpole chains (as discussed in Chapter 6 for the pure material) is that there is threading. Perhaps the linear tails of the tadpole chains adsorbed on the substrate can thread through the ring part of the tadpole chains on top of the irreversibly adsorbed layer, and thus slow down the dynamics of those chains. Whatever the mechanism, this slowing down at the substrate can propagate into the film up to $5R_g$ away from substrate. Furthermore, the addition of a very small amount of this high molecular weight contaminant apparently slows the rate at which

the highly dense irreversibly adsorbed layer forms, so after 12 hours of annealing the film from contaminated TPS is less well developed than that in the film of pure chains.